AD NUMBER

ADB062870

NEW LIMITATION CHANGE

TO

Approved for public release, distribution unlimited

FROM

Distribution authorized to U.S. Gov't. agencies only; Test and Evaluation; Apr 1981. Other requests shall be referred to the Air Force Wright Aeronautical Laboratories [FIBR], Wright-Patterson Air Force Base, Ohio 45433.

AUTHORITY

AfWAL ltr, 9 Mar 1984

UNCLASSIFIED

AD B062 870

AUTHORITY: AFWAL LTR,
9 mar 84

UNCLASSIFIED

BEST AVAILABLE COPY

THIS REPORT HAS BEEN DELIMITED AND CLEARED FOR PUBLIC RELEASE UNDER DOD DIRECTIVE 5200.20 AND NO RESTRICTIONS ARE IMPOSED UPON ITS USE AND DISCLOSURE.

DISTRIBUTION STATEMENT A

APPROVED FOR PUBLIC RELEASE; DISTRIBUTION UNLIMITED.

AFWAL-TR-81-3066

A DEMONSTRATION OF THE PRINCIPLE OF AEROELASTIC TAILORING APPLIED TO FORWARD SWEPT WINGS

Van C. Sherrer, Capt., USAF
Terrence J. Hertz
Michael H. Shirk

Aeroelastic Group
Analysis and Optimization Branch
Structures and Dynamics Division

January 1982

Final Report for Period February 1978 - April 1981

FLIGHT DYNAMICS LABORATORY
AIR FORCE WRIGHT AERONAUTICAL LABORATORIES
AIR FORCE SYSTEMS COMMAND
WRIGHT-PATTERSON AIR FORCE BASE, OHIO 45433

NOTICE

When Government drawings, specifications, or other data are used for any purpose other than in connection with a definitely related Government procurement operation, the United States Government thereby incurs no responsibility nor any obligation whatsoever; and the fact that the government may have formulated, furnished, or in any way supplied the said drawings, specifications, or other data, is not to be regarded by implication or otherwise as in any manner licensing the holder or any other person or corporation, or conveying any rights or permission to manufacture, use, or sell any patented invention that may in any way be related thereto.

This technical report has been reviewed and is approved for publication.

Michael H Shirk

MICHAEL H. SHIRK
Principal Scientist
Analysis & Optimization Branch

Fred A Picchioni

FREDERICK A. PICCHIONI, Lt Col, USAF
Chief, Analysis & Optimization Branch
Structures & Dynamics Division

FOR THE COMMANDER:

Ralph L Kuster Jr

RALPH L. KUSTER, Jr., Col, USAF
Chief, Structures & Dynamics Division

"If your address has changed, if you wish to be removed from our mailing list, or if the addressee is no longer employed by your organization please notify AFWAL/FIBRC, W-P AFB, OH 45433 to help maintain a current mailing list".

Copies of this report should not be returned unless return is required by security considerations, contractual obligations, or notice on a specific document.

AIR FORCE/56780/5 February 1982 — 170

UNCLASSIFIED

SECURITY CLASSIFICATION OF THIS PAGE (When Data Entered)

REPORT DOCUMENTATION PAGE		READ INSTRUCTIONS BEFORE COMPLETING FORM
1. REPORT NUMBER AFWAL-TR-81-3066	2. GOVT ACCESSION NO.	3. RECIPIENT'S CATALOG NUMBER
4. TITLE (and Subtitle) A DEMONSTRATION OF THE PRINCIPLE OF AEROELASTIC TAILORING APPLIED TO FORWARD SWEPT WINGS		5. TYPE OF REPORT & PERIOD COVERED Final Report February 1978-April 1981
		6. PERFORMING ORG. REPORT NUMBER
7. AUTHOR(s) Van C. Sherrer Terrence J. Hertz Michael H. Shirk		8. CONTRACT OR GRANT NUMBER(s) FE 61102F
9. PERFORMING ORGANIZATION NAME AND ADDRESS Analysis and Optimization Branch 62662 Flight Dynamics Laboratory (AFWAL/FIBR) Air Force Wright Aeronautical Laboratories Wright-Patterson AFB, Ohio 45433		10. PROGRAM ELEMENT, PROJECT, TASK AREA & WORK UNIT NUMBERS Project 2401 Task 240102 Work Unit 24010226
11. CONTROLLING OFFICE NAME AND ADDRESS Air Force Wright Aeronautical Laboratories Air Force Systems Command Wright-Patterson AFB, Ohio 45433		12. REPORT DATE January 1982
		13. NUMBER OF PAGES 126
14. MONITORING AGENCY NAME & ADDRESS (if different from Controlling Office)		15. SECURITY CLASS. (of this report) Unclassified
		15a. DECLASSIFICATION/DOWNGRADING SCHEDULE

16. DISTRIBUTION STATEMENT (of this Report)

Distribution limited to U.S. Government agencies only; test and evaluation April 1981. Other requests for this document must be referred to Air Force Wright Aeronautical Laboratories (FIBR), Wright-Patterson AFB, Ohio 45433.

17. DISTRIBUTION STATEMENT (of the abstract entered in Block 20, if different from Report)

18. SUPPLEMENTARY NOTES

19. KEY WORDS (Continue on reverse side if necessary and identify by block number)

Aeroelastic Tailoring
Composites
Forward Swept Wing
Wind Tunnel Test

20. ABSTRACT (Continue on reverse side if necessary and identify by block number)

The principle of aeroelastic tailoring with advanced composite materials to increase the divergence speed of a forward swept wing has been demonstrated through low speed wind tunnel tests. The approach was to perform a low cost, fairly simple wind tunnel test on a variable sweep cantilever wing model. Available analytical methods were used and were shown to accurately predict the divergence speed of both aluminum and composite plate structures in the subsonic speed range. Methods were evaluated for predicting the onset of divergence using subcritical wind tunnel data. Results of the analyses and tests are presented.

DD FORM 1 JAN 73 1473 EDITION OF 1 NOV 65 IS OBSOLETE

UNCLASSIFIED

SECURITY CLASSIFICATION OF THIS PAGE (When Data Entered)

FOREWORD

The analysis and tests described in this report were performed by the Aeroelastic Group, Analysis and Optimization Branch, Structures and Dynamics Division, Flight Dynamics Laboratory, Air Force Wright Aeronautical Laboratories, under work unit 24010226, "Forward Swept Wing Aeroelastic Studies".

The work was performed between February 1978 and April 1981. Capt V. C. Sherrer, USAF, Mr. T. J. Hertz, and Mr. M. H. Shirk were the principal investigators.

The assistance of the Air Force Institute of Technology in the fabrication of parts of the divergence model and wind tunnel testing of the model is sincerely appreciated. Special thanks to: Messrs J. Tiffany, R. Ruley, and R. Murry of the AFIT model shop, and S. Whitt and N. Yardich at the AFIT five foot wind tunnel. Thanks also goes to Mr. R. Achard and his people in the FDL Composites Facility Group for their help in constructing the composite plates, to Mr. B. Foist of Purdue University for his assistance in the testing phases of this effort, and Mr. E. Pendleton of the Aeroelastic Group for his work on the load deflection testing. And, appreciation is extended to Mrs. Lisa Wilson and Ms. Mary Lipik for their diligent work in preparation of the manuscript and visual aids.

TABLE OF CONTENTS

LIST OF ILLUSTRATIONS

LIST OF ILLUSTRATIONS (CONT'D)

LIST OF TABLES

LIST OF SYMBOLS

A	plate area
AR	aspect ratio
a_o	two-dimensional lift curve slope
B	strain gage calibration constant; bending mode
c	chord
C_{L_α}	wing lift curve slope
E	modulus of elasticity
EI	bending stiffness
F_r	wing restoring force
G	modulus of elasticity in shear
GJ	torsional stiffness
g	damping coefficient
h	length on gridboard (load deflection test)
k	wing structural stiffness
L	lift
ℓ	wingspan; distance from gridboard to plane of wing (load deflection test)
M	average moment (load deflection test)
q	dynamic pressure
q_D	divergence dynamic pressure
S	wing planform area
T	applied torque (load deflection test); torsion mode
V	velocity
W	plate weight
x	streamwise distance on wing from leading edge root
y	spanwise distance from wing root
α	angle of attack
Δ	difference; divergence index
ϵ	strain
θ	twist or bending slope (load deflection test); angle of attack due to wing flexibility
Λ	wing leading edge sweep
λ	taper ratio; slope of angle of attack versus strain

LIST OF SYMBOLS (CONT'D)

ν	Poisson's ratio
ω	frequency

Superscripts

t	tension

Subscripts

n	dynamic pressure index
S	symmetric
1	longitudinal
2	transverse
12	shear

LIST OF ABBREVIATIONS

deg	degree
CG	center of gravity
GVT	ground vibration test
Hz	Hertz; cycles per second
in	inches
lb	pounds
mv	millivolts
psf	pounds per square foot
psi	pounds per square inch
μin/in	micro inch per inch

SECTION I

INTRODUCTION

Until recently, consideration of aeroelastic divergence has essentially eliminated the forward swept wing as an aircraft design option. The static aeroelastic instability of divergence of lifting surfaces is well known. Bisplinghoff [1] presents the classical trend of divergence speed as a function of wing sweep. In the figure taken from his text (Figure 1), he shows the divergence speed for a conventional wing reduces dramatically with moderate forward sweep, but the divergence speed becomes very high with moderate aft sweep.

Bending deformation affects the aeroelastic behavior of swept wings. For a slender wing with aft sweep, bending produces a reduction in the local angle of attack known as wash-out. Wash-out unloads the wing and virtually eliminates the problem of divergence in aft swept wings. However, for a slender wing with forward sweep, bending produces an increase in the local angle of attack, or wash-in. Wash-in increases the aerodynamic loading and total flexible lift curve slope of the wing, and consequently reduces the aeroelastic divergence speed. An approach to the problem of increasing the divergence speed is to reduce the bending deformation, and the wing wash-in. For the conventional metallic wing under a given aerodynamic loading, the bending deformation is reduced by increasing the wing bending stiffness which normally requires an increase in structural material with an associated increase in weight. For a conventional metallic wing structure with a forward sweep greater than 15°, the weight required to provide adequate stiffness for sufficiently high divergence speeds is prohibitive.

A different approach to increasing divergence speed is possible when advanced composite materials are used in the wing structure. If one looks carefully at the problem of divergence, only a reduction in wash-in is required, not necessarily an accompanying reduction in bending. Advanced composites such as graphite-epoxy and boron-epoxy have significantly higher specific stiffness and specific strength characteristics than conventional aircraft metals. Additionally, these properties are directional. The directional properties of composites can be oriented to alter the deformation under loading. By orienting the composites in

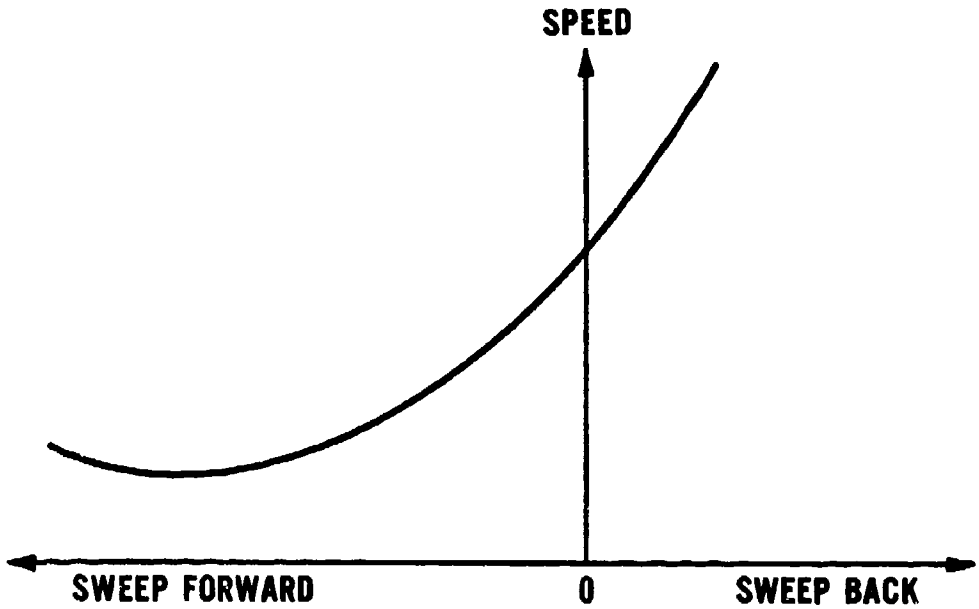

Figure 1. Divergence Speed Variation with Wing Sweep.

advantageous directions, wash-in of a forward swept wing can be reduced, and hence, the divergence speed can be increased. Therefore, to increase divergence speed, significantly less weight would be required for a composite structure than for a conventional metal structure.

The technology to design for a desired aeroelastic response of a lifting surface using advanced filamentary composite materials has been named aeroelastic tailoring. References 2 through 11 describe the aeroelastic tailoring technology and its applications. Krone [2] applied the aeroelastic tailoring procedure described in Reference 3 to design for elimination of aeroelastic divergence. He showed that the weight of executive transport and lightweight fighter wings with sweeps from 35° aft to 35° forward could be significantly reduced using tailored composites. A weight comparison of a metallic wing and a tailored composite wing for a lightweight fighter is presented in Figure 2 taken from Reference 2. The figure shows that for increasing forward sweep the weight required in aluminum to provide adequate stiffness increases much faster than the weight required in tailored composites. Weisshaar [5,6] used laminated beam theory and aerodynamic strip theory to predict the static aeroelastic divergence characteristic of

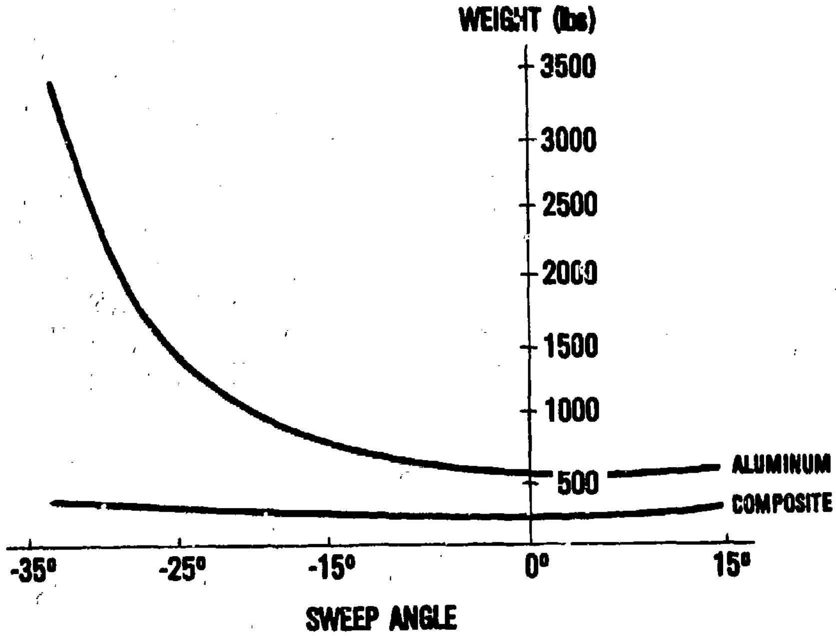

Figure 2. Lightweight Fighter Wing Skin Weight Variation with Sweep.

swept wings. He showed that, because of elastic coupling between the bending and torsional deformation of the wing box, laminated composites may be used to preclude divergence for a large range of forward sweep angles.

Since the forward swept wing has not been considered a serious design option, there is a scarcity of data on its structural and aeroelastic characteristics. The Flight Dynamics Laboratory recognized the need for experimental data that would illustrate the principle of aeroelastic tailoring with composites and its application to divergence of forward swept wings. This report describes the design, analysis and testing of an aeroelastic model which incorporates variable forward wing sweep. Four plates of the same planform, one aluminum and three graphite-epoxy composite plates with different laminate orientations, were individually incorporated in the model as the structural element. The test and analysis results illustrate a simple, yet effective, form of aeroelastic tailoring.

SECTION II

MODEL DESIGN AND FABRICATION

1. DESIGN CONSIDERATIONS

The objective of the model design was not to replicate a full-scale wing, but rather to create a versatile research tool from which a maximum amount of data could be obtained. The relatively simple wing design facilitated fabrication and computer modeling, yet it was of sufficient complexity to provide experience in analyzing and wind tunnel testing a forward swept wing model.

The half-span model was designed to diverge at approximately the middle of the velocity range of the Air Force Institute of Technology (AFIT) five foot wind tunnel. The maximum velocity of this tunnel is approximately 300 feet per second. The boundary layer at the maximum velocity is approximately three inches thick.

The model design evolved from the basic concept of using a cantilevered plate as the load carrying member with an airfoil shaped (NACA 0010) polyurethane foam sleeve surrounding the plate. The model with three of the sleeve sections removed from the plate is shown in Figure 3. The plate concept was required in order to demonstrate the effect of tailoring of composite materials while allowing divergence of the wing within the available tunnel velocity range. A conventional two-skin wing box design could not be used because it would have presented an excessive stiffness problem. The half-span model was designed so the plate could be removed permitting testing of both aluminum and graphite-epoxy materials while using the same aerodynamic sleeve.

The initial sizing of the plate was accomplished by using the closed form solution for divergence dynamic pressure given in Bisplinghoff (Reference 1) for a uniform slender swept wing:

$$q_D = \frac{6.33EI}{a_o c \ell^3 \cos^2\Lambda |\sin\Lambda|} \quad (1)$$

The lift curve slope a_o was assumed to be less than the two-dimensional value (2π) for conservatism.

The span at 30° forward sweep was 24 inches with a full-span aspect ratio of 4 and a taper ratio of 0.4. The aspect ratio was selected as representative of current fighter aircraft designs. For a wing of

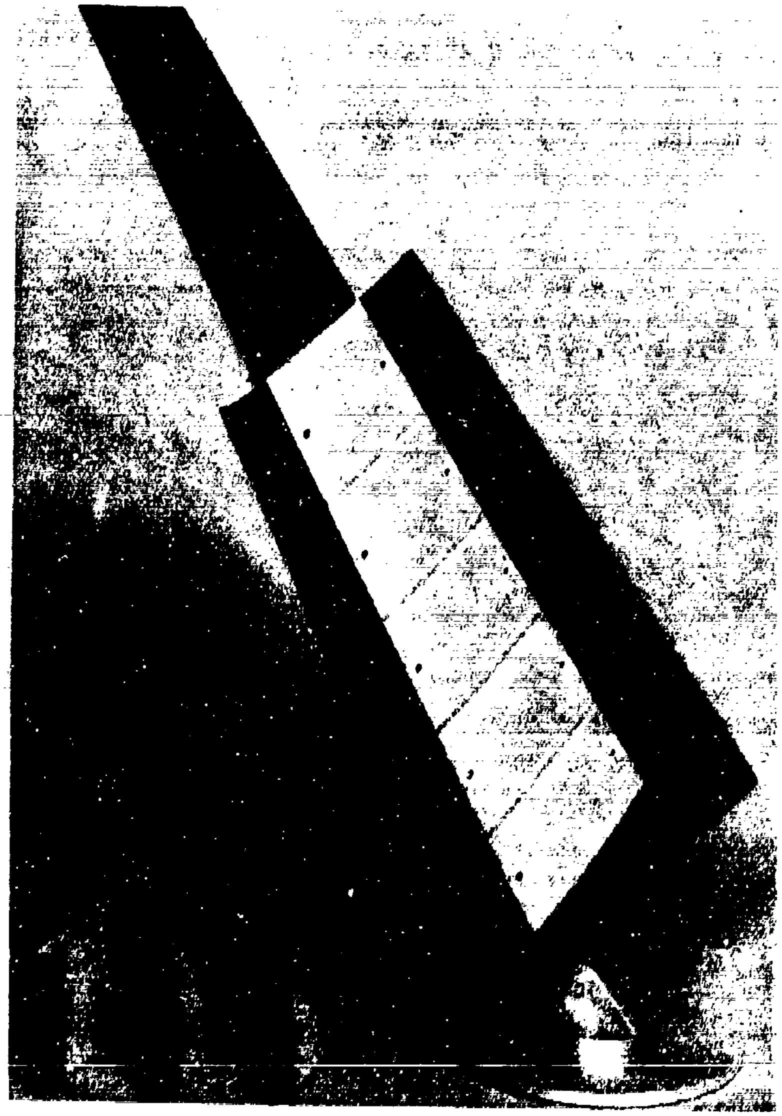

Figure 3. Flight Dynamics Laboratory Forward Swept Wing Model.

this geometry, the thickness of an aluminum plate and of a 0°±45° laminated graphite-epoxy plate was established for a dynamic pressure at the midrange of the wing tunnel.

To increase the capability of the model, two features were incorporated in the model design. The leading edge sweep could be varied from

0° to 60° forward in increments of 15°, as shown in Figure 4. At zero leading edge sweep, the maximum span is 33.0 inches. In addition, the ability to vary the model angle of attack was included. Variable model angle of attack was required for the subcritical divergence projection methods used during the wind tunnel testing.

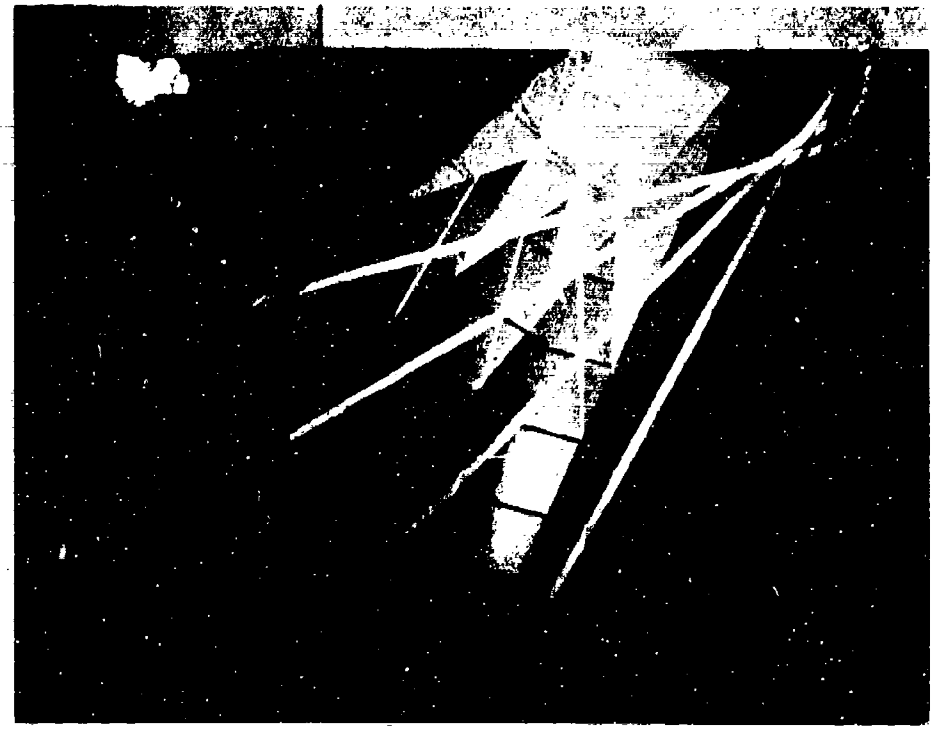

Figure 4. The Five Forward Sweep Positions of the Model.

2. COMPONENT DESCRIPTIONS

The structural load carrying member of the wing model was one of four plates of identical planform. The plate position and wing dimensions in the 30° forward sweep position are shown in Figure 5. The leading and trailing edges of the plate were on the 15 and 65% chord lines, respectively, and the wing reference line was on the 40% chord line. At -30° sweep, the plate tips were cut parallel to

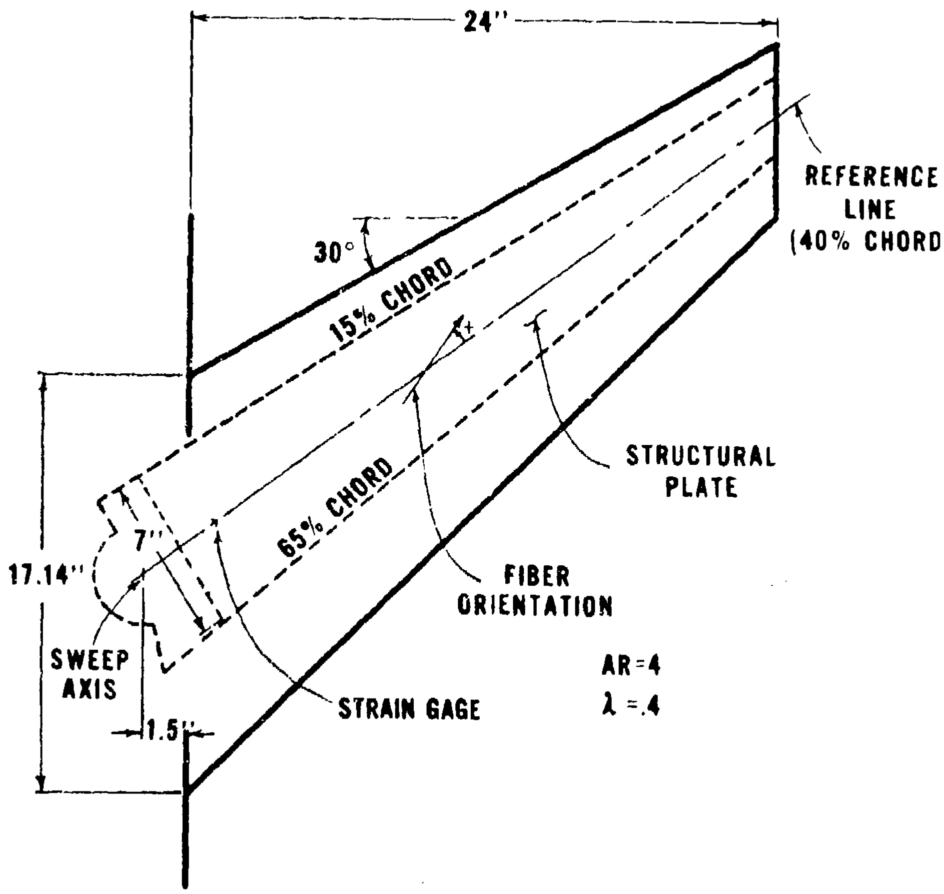

Figure 5. Wing Dimensions.

the airstream. The pivot axis was located on the reference line 1.5 inches inboard of the wing root chord.

The 4 plates, 1 aluminum and 3 composite, were tested at each of the 5 sweep positions, allowing for information to be collected on 20 wing configurations. The 0.10 inch, 2024-T6 aluminum plate was used as the baseline structure.

The 3 composite plates consisted of 16 plies of NARMCO T300/5208 graphite-epoxy with a nominal thickness of 5.25 mil. Each of these plates were cut from a larger plate with a symmetric layup of four 0° plies on the outside of the laminate and two pairs of ±45° plies on the inside, or $[0_4,(-45,+45)_2]_S$, (Table 1). As shown in Figure 6, one plate was cut so the 0° plies were parallel to the reference line. The second

TABLE 1

GRAPHITE-EPOXY LAMINATE
STACKING SEQUENCE

Ply Number	Orientation (about reference line)
1	0°
2	0°
3	0°
4	0°
5	-45°
6	45°
7	-45°
8	45°
Symmetric Laminate	

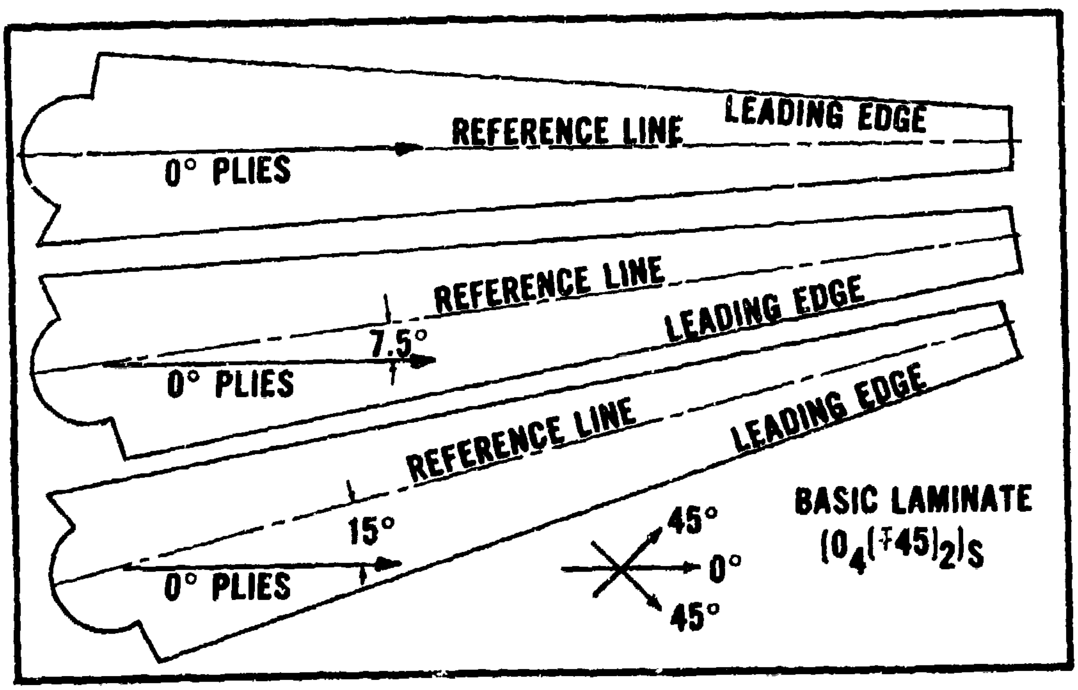

Figure 6. Graphite-epoxy Plate Orientation Prior to Cutting.

and third plates were cut so the 0° plies, and consequently the laminates, were rotated 7.5° and 15° forward of the reference line, respectively. A positive fiber orientation is forward of the reference axis. After curing, the 16 ply laminate had an average total thickness of 0.080 inches.

After fabrication, each plate was instrumented with strain gage rosettes located on either side of the plate on the reference line four inches outboard of the root. The two opposing center gages on each plate were connected in a Wheatstone bridge to record the average bending strain. The torsional strain was obtained from an opposing set of gages oriented 45° from the reference line. The remaining set of 45° gages were used as spares. Since only differential voltage readings were required for the subcritical divergence projection methods, the gages were not calibrated.

To achieve the minimum sleeve stiffness and promote durability, the sleeve was sectioned and each section employed a bridging concept. Bridges are commonly used in beam type flutter models to transfer loads from the airfoil to the load carrying member over a minimum of beam area. In the midspan of each section, an aluminum U-shaped channel was encased in the foam on both sides of the plates. The aluminum plate with the bridges installed, prior to foaming of the sleeve, is shown in Figure 7. After foaming, the sleeve was sectioned to reduce the bending and torsional stiffness attributed to the sleeve. The crosswise dowels added lateral stability to each section and transmitted the airloads on the section onto the bridge. Only the bridges contacted the plates. Two aluminum bolts one-half inch from the leading and trailing edges of the plate held each section to the plate.

The variable sweep mechanism (Figure 8) cantilevered the wing and provided the variable sweep and variable angle of attack features of the model. The structural plate root was clamped between two 0.25 inch steel plates. The wing pivoted about a 9/16 inch bolt located near the center of this mechanism. The nine holes located on an arc centered at the pivot were used to align the wing at the desired sweep angles.

A fairing that had been used for a previous test in the AFIT tunnel was adapted for mounting the wing models. The sweep mechanism was housed inside the fairing which was mounted to the wind tunnel ceiling.

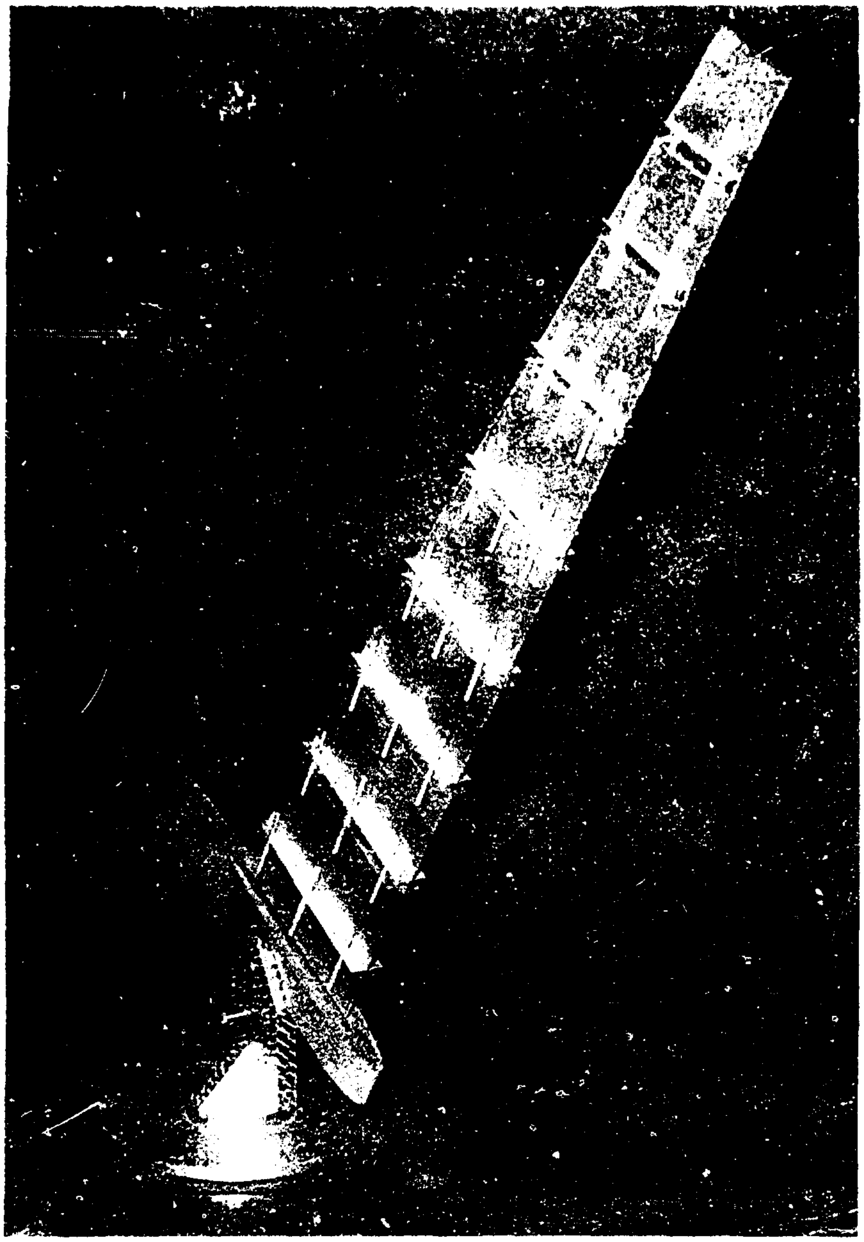

Figure 7. Aluminum Plate with Bridges.

Figure 9 shows a sketch of the wing installed in the fairing at the 30° forward sweep position. The stainless steel tube on the sweep mechanism projected through the fairing and tunnel ceiling, and was used to control the wing angle of attack from outside the tunnel. The opening in the fairing at the wing root was minimized depending on the wing sweep by various cover plates. One side of the fairing was hinged to provide access to the sweep mechanism.

BEST AVAILABLE COPY

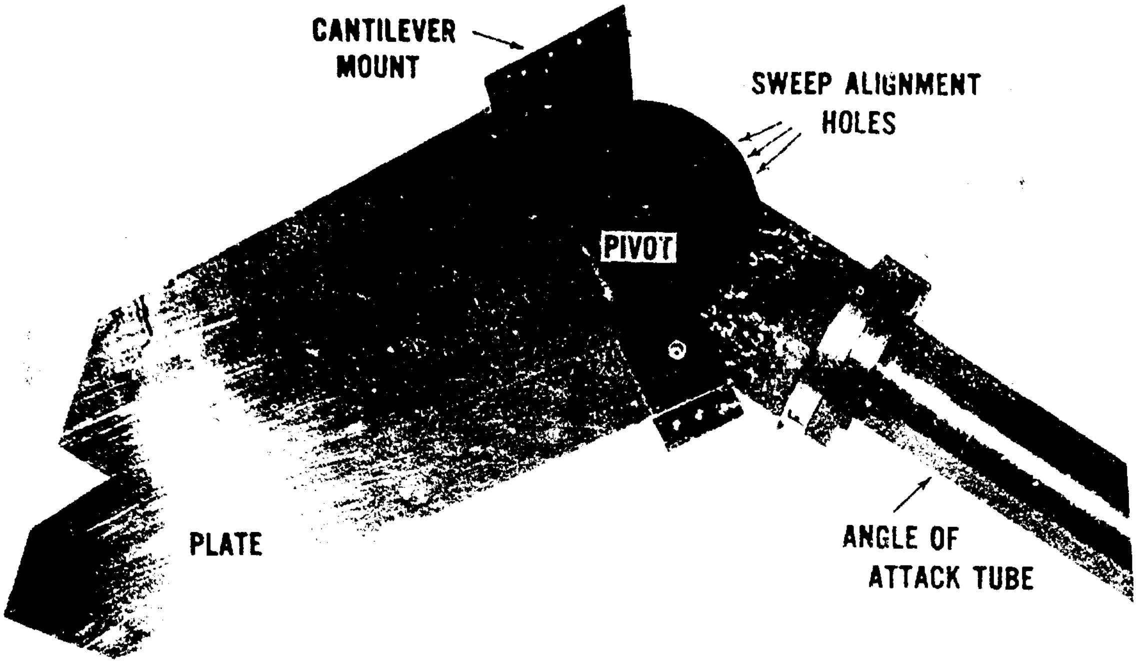

Figure 8. Variable Sweep Mechanism and Cantilever Mount.

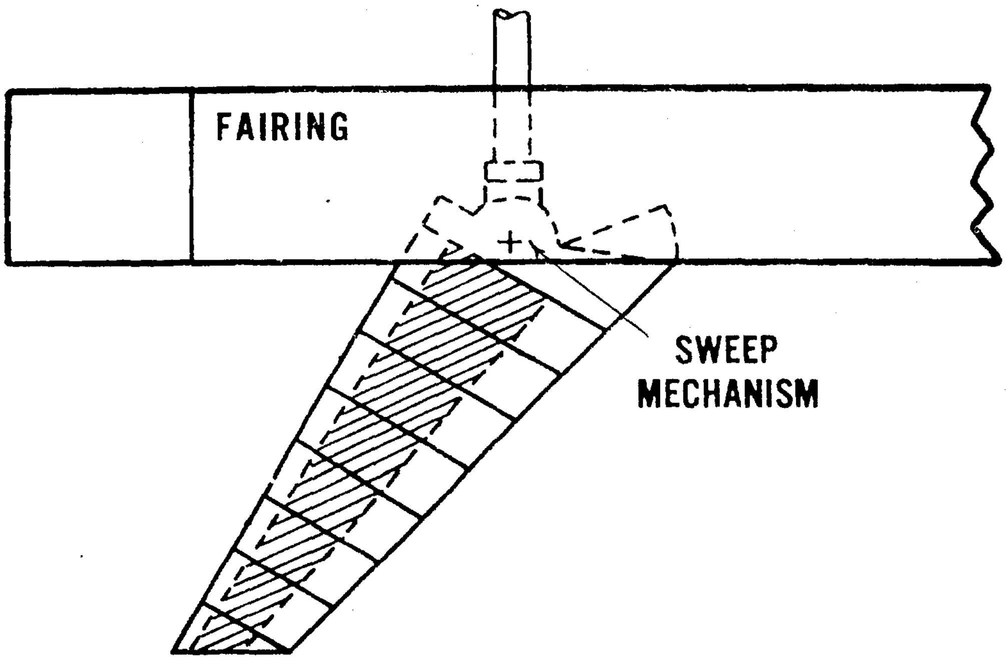

Figure 9. Wing Model in Fairing.

BEST AVAILABLE COPY

In order to avoid confusion in the following sections of this report, the following terms will be used to describe the wing configurations. The term plate refers to one of the four plates without the sleeve. The term rotated refers to one of the three graphite-epoxy plates: the nonrotated, 7.5° rotated and 15° rotated plates. The term model refers to a plate and sleeve configuration such as aluminum model or 7.5° rotated model. The term wing is a generic reference applying to both plates and models.

SECTION III

PRE-WIND TUNNEL TESTS

1. MATERIAL PROPERTIES

As properties of composite materials can vary significantly from batch to batch, specimens of the NARMCO T300/5208 graphite-epoxy were tested in tension to failure to experimentally determined the elastic moduli and ultimate tensile strains. Each specimen consisted of 16 plies of the graphite-epoxy. For the longitudinal modulus, four specimens with all fibers oriented in the load direction were tested. For the transverse modulus, four specimens with all fibers oriented perpendicular to the load direction were tested. For the shear modulus, four specimens with ±45° plies were loaded in tension. The average measured values for these moduli are given in Table 2 with the aluminum material properties.

TABLE 2

ELASTIC CONSTANTS

Constant	Aluminum	Graphite-epoxy
Density (psi)	.1	.059
Longitudinal Modulus E_1^t (psi)	10.5×10^6	20.8×10^6
Transverse Modulus E_2^t (psi)	10.5×10^6	1.54×10^6
Poisson's Ratio ν_{12}	.3	.327
Shear Modulus G_{12} (psi)	4.04×10^6	0.80×10^6
Ultimate Strains:		
Longitudinal ε_1^t (μin/in)		11.2×10^3
Transverse ε_2^t (μin/in)		4.7×10^3
Shear ε_{12}^t (μin/in)		19.0×10^3

2. SLEEVE MASS AND INERTIA DATA

Each sleeve section was first weighed to the nearest 0.1 gram on a balance. The center of gravity of each section was located by balancing the section on a knife edge at three angular orientations. Lines were etched in the surface of the section along the knife edge. The intersection of the lines was the center of gravity of the section.

The bifilar pendulum method was used to determine the rotational inertia of each section about an axis parallel to the wing leading edge and through the center of gravity of each section. The measured mass inertia and center of gravity location of each section are given in Table 3.

TABLE 3

SLEEVE MASS DATA

Section	Center of Gravity from leading edge root $\Lambda = 0°$ (in) x	y	Mass (lb)	Moment of Inertia About CG ($lb\text{-}in^2$)
1	5.91	1.94	.2710	2.993
2	5.44	5.96	.2403	2.338
3	4.95	9.94	.2077	1.714
4	4.51	13.96	.1821	1.258
5	4.02	18.03	.1557	.8874
6	3.53	22.00	.1299	.5838
7	3.04	25.85	.0931	.3335
8	2.28	29.30	.0788	.1937

3. LOAD DEFLECTION TESTS

All of the plates and models were loaded in bending and in torsion, to determine the relative spanwise bending and torsional stiffness distributions. Front surfaced mirrors were imbedded in modeling clay and attached to balsa wood bridges. Each bridge was supported on the surface of a sleeve section by two straight pins at the trailing edge and one pin at the leading edge. The mirrors were positioned on the reference line at the midpoint of each section. The bridges reduced inaccuracies that could be caused by local surface distortion. A light source was used to reflect crosshairs off the mirrors and onto a gridboard.

By recording the position of the crosshairs on the gridboard before and after loading the model, the difference in twist or bending slope between secccions could be calculated. The difference in slope, $\Delta\theta$, is given by

$$\Delta\theta = \Delta h/2\ell \tag{2}$$

where Δh is the distance the crosshairs move on the gridboard, parallel to the reference axis for bending and perpendicular to the reference axis for twist. The length, ℓ, is the distance between the gridboard and the plane of the wing.

The average bending stiffness, EI, between mirrors is given by

$$EI = M\Delta y/\Delta\theta \tag{3}$$

where M is the average applied moment and Δy is the distance between adjacent mirrors. The average value for torsional stiffness, GJ, is

$$GJ = T\Delta y/\Delta\theta \tag{4}$$

where T is the applied torque. Stiffness distributions for the aluminum plate and model are compared to the theoretical distributions for bending, Figure 10, and for torsion, Figure 11. Except for the low value of bending stiffness at the tip due to the stress concentration caused by the load, the measured plate stiffnesses compare favorably with the theoretical values.

As described earlier, the plates are constant thickness, therefore the stiffnesses vary linearly with span. Dividing the measured stiffnesses by the respective chord results in a constant value along the span and provides a means of comparison of theory and experiment for the overall plate. Neglecting extreme deviations from the linear relationship, the results were averaged and are given with the symbol key in Figure 10 and 11.

The average plate bending and torsional stiffnesses are both less than the theoretical values, but the difference is less than 1%. The contribution of the model stiffness due to the sleeve is less than 6% in bending but greater than 20% in torsion.

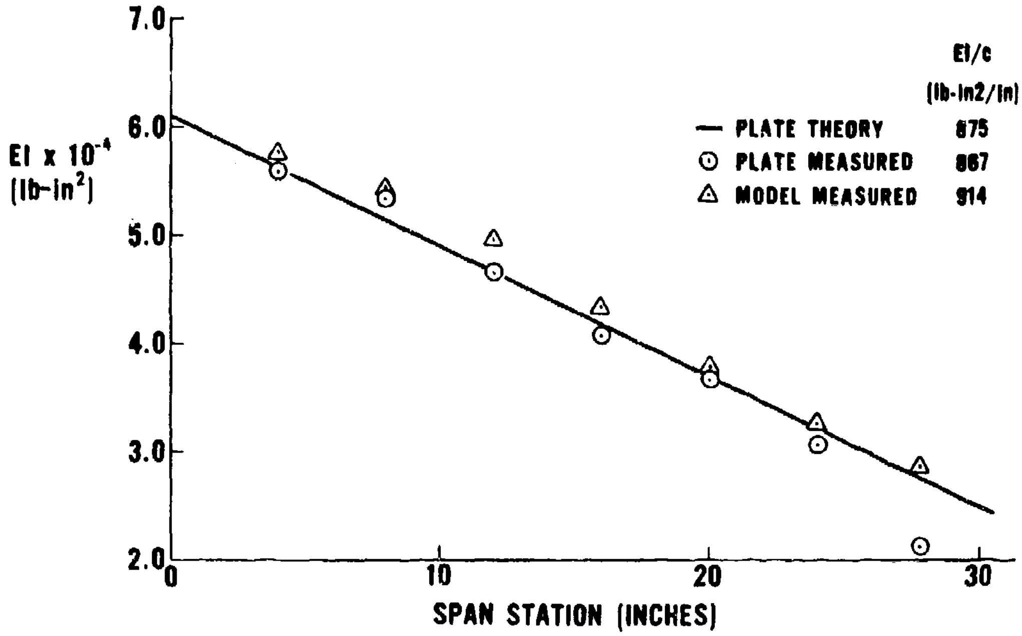

Figure 10. Aluminum Plate Bending Stiffness Distribution.

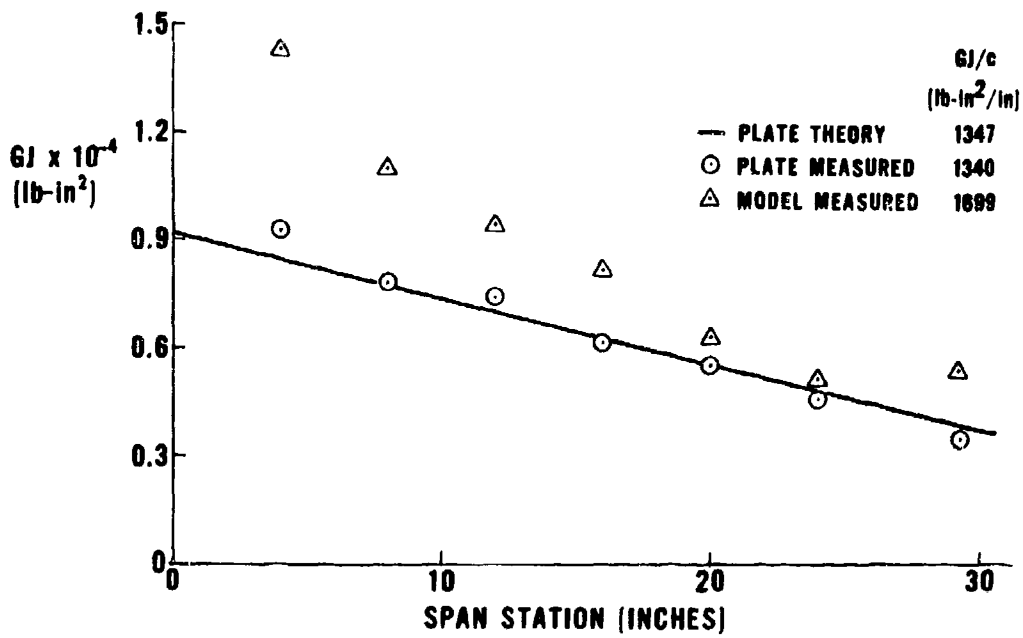

Figure 11. Aluminum Plate Torsional Stiffness Distribution.

Another loading test was conducted to locate the approximate zero twist axis of each plate. A perpendicular point load was applied directly to the plate at successive locations between two adjacent sleeve sections and the motion of the reflection of the mirror on the inboard section was observed. The point where the reflection remained stationary is on the zero twist axis. Figure 12 shows the zero twist axis for each of the four models. The aluminum model has a zero twist axis nearly perpendicular to the cantilevered root line. The zero twist axis is approximately oriented with the 0° fibers on each of the composite models.

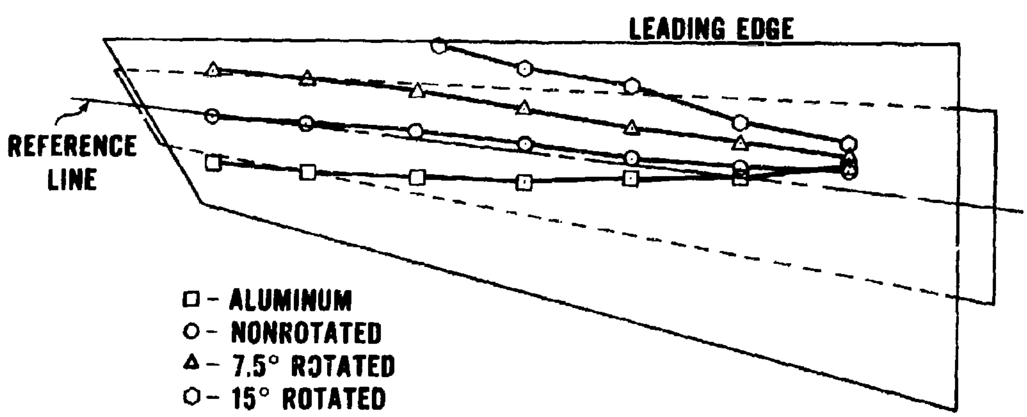

Figure 12. Zero Twist Axes.

4. GROUND VIBRATION TESTS

Ground vibration tests were the last tests conducted before entry into the wind tunnel. The frequencies and mode shapes for each plate and for each model were measured. A roving accelerometer was used to record the relative displacement amplitudes at 17 points on the wing: two chordwise locations on the mid-span of each section at the leading and trailing edge of the plate and one location on the root pivot. The measured mode shapes for the models are presented in Appendix A. The measured natural frequencies are presented in Table 4.

TABLE 4

WIND TUNNEL MODEL EXPERIMENTAL FREQUENCIES

Mode	Aluminum		Graphite-epoxy Nonrotated		Graphite-epoxy 7.5° Rotated		Graphite-epoxy 15° Rotated	
	Plate	Model	Plate	Model	Plate	Model	Plate	Model
1B	4.40	3.32	6.13	3.57	5.60	3.40	5.18	3.19
2B	21.81	16.97	31.29	17.04	29.21	16.96	23.35	15.36
1T	59.10	36.09	41.53	31.57	42.48	32.04	47.25	31.42
3B	60.72	43.48	82.05	46.53	76.63	44.36	67.52	40.70
2T	141.64	81.85	98.60	64.88	110.01	65.88	113.76	68.74
4B	115.34	87.07	152.93	86.22	145.77	83.08	---	75.99

Units: Hz

SECTION IV

MODEL ANALYSIS

1. METHODS OF ANALYSIS

Slender beam theory [1] and the method developed by Weisshaar [5], were used to perform preliminary analyses of the four models to insure that divergence could be obtained within the speed range of the wind tunnel. The analyses were refined using two procedures, TSO and NASTRAN. The analysis methods are described in this section.

a. Slender Beam Theory

The slender beam theory as presented by Bisplinghoff [1] assumes a high aspect ratio wing structure can be modeled by uncoupled bending and torsion flexibility coefficients at given span stations along an elastic axis. The wing model had a sufficiently high span to chord ratio and could be analyzed by this method, but the graphite-epoxy models exhibit coupled bending and torsion flexibility, so only the baseline aluminum wing could be analyzed. Modified strip theory aerodynamics provided the aerodynamic influence coefficients required to perform the divergence analyses.

b. CWING

The computer procedure CWING is an inexpensive analytical tool developed by Dr. T. A. Weisshaar of Virginia Tech for the Flight Dynamics Laboratory. Initially, the program provided a closed form solution of the divergence problem for specific wing configurations [5]. In subsequent studies [6], Dr. Weisshaar expanded CWING to provide analysis of divergence, lift redistribution, and aileron effectiveness of more general wing configurations. CWING uses a Weissenger-L aerodynamic theory and a structural model that has its properties defined at a finite number of span stations.

c. TSO

The aeroelastic tailoring computer procedure TSO [3,4] is an interdisciplinary preliminary design program combining aerodynamic, static aeroelastic, flutter, and structural analyses. Low to moderate aspect ratio wings can be modeled as plates, therefore the direct Rayleigh-Ritz energy formulation for a plate is used to perform structural analyses.

In TSO, a symmetric wing structural box is simulated by a trapezoidal plate with depth and skin thickness given by biquadratic polynomials. Three skin orientations may be modeled. In most wing structures, the structural box has a depth much greater than the skin thickness, and hence, the TSO stiffness polynomial was formulated assuming the plies of each orientation are distributed evenly over the skin thickness. Because the wind tunnel model structural box was a plate with no core between upper and lower skins, the stacking sequence plays an important role in the overall stiffness of the plate. To account for the error induced by the stacking sequence distribution assumed in TSO, equivalent thicknesses were calculated for a distributed stacking sequence that would yield the same flexibility as a specifically distributed laminate. The equivalent thicknesses for each orientation were calculated by equating the definition of the flexibility matrix for a distributed stacking sequence given in Reference 3 with the flexibility matrix for a specifically distributed laminate.

Two aerodynamic matrices used in TSO are calculated in other computer procedures. The steady aerodynamic matrix is provided by a Woodward aerodynamic routine, ROT [4,12]. This matrix is used with the structural influence matrix generated in TSO to calculate the divergence velocity.

The unsteady aerodynamic matrices are provided by a doublet lattice aerodynamic routine, N5KA [4,13]. An aerodynamic matrix is calculated for each of 20 reduced frequencies and a K-method modal flutter solution is used to solve for the velocities, frequencies, and dampings. For a reduced frequency near zero the corresponding aerodynamic matrix approximates the steady aerodynamic matrix, and hence, the divergence velocities can be calculated by the dynamic analysis in TSO.

d. NASTRAN

The NASTRAN finite element structural analysis computer program [14] was used for stress analysis, free vibration analysis, and flutter and divergence analyses. Levels 16 and 17 were used in all the NASTRAN analyses.

For the aluminum plate, the homogeneous elements CQUAD2 and CTRIA2 were used with the material properties input on a MAT1 card. For the graphite epoxy plates, CQUAD1 and CTRIA1 elements were used to simulate the anisotropic properties of composite laminates. For each of the three composite laminates, representative 3X3 in-plane and bending stiffness matrices were computed and input on MAT2 cards. These stiffness matrices were obtained from program SQ5 [15], which gives the in-plane and bending stiffness of a laminate accounting for ply material properties, ply thickness, stacking sequence and orientation.

A stress analysis of the three composite laminates was accomplished using rigid Format 1 of NASTRAN. The highest expected steady airload was first obtained from computer Procedure TSO using Woodward aerodynamics. These airloads were then resolved into lift forces and moments at the NASTRAN grid points by a program known as BEAMING [16]. The static loads were then applied to the finite element NASTRAN model to calculate stresses, element forces and displacements at the grid points. The area of the model near the root of the wing, where the highest stresses were expected, was divided into a finer mesh for better stress definition. Using the calculated element forces, point stress analysis program SQ5 was used to compute strain margins for each ply of graphite epoxy in the unrotated laminate near the cantilevered root area.

Rigid Format 3 of NASTRAN was used to extract the first six normal mode shapes and corresponding frequencies using the inverse power eigenvalue extraction method.

Rigid Format 10 of NASTRAN was used for flutter analysis. This rigid format incorporated doublet lattice aerodynamic theory to compute the aerodynamic influence coefficient matrix used in the flutter equation. The K-method of modal flutter solution was used to solve the flutter equation for both flutter and divergence speeds. A range of reduced frequencies down to zero was used to obtain corresponding values of damping and frequency at each value of velocity for each mode in the analysis. The first three normal modes were used in the modal solution. Flutter of the wing was indicated when the damping of the mode was equal to zero. Divergence of the wing was indicated when the damping and frequency of a mode simultaneously went to zero.

2. ANALYTICAL MODELS

a. Slender Beam Theory Analysis

The beam theory divergence analysis was performed at the five sweep positions for the wing assuming aerodynamics for the wing planform and stiffness due to only the aluminum plate. The wing planform was divided into seven strips of equal width. Theoretical values of bending and torsional stiffness were calculated at the midpoint of each of the seven strips. The aerodynamic strip theory was modified by calculating the aerodynamic center and local lift coefficient for each of the seven strips using doublet lattice aerodynamic theory. The calculated divergence dynamic pressures confirmed that the model would diverge well within the range of the tunnel.

The effect of the increase in stiffness due to the sleeve is evident in Table 5. The divergence dynamic pressures presented in this table were recalculated using the measured bending and torsional stiffnesses of the aluminum plate alone and of the aluminum model. Theoretical aerodynamics for the wing planform were used in the calculation of these dynamic pressures.

TABLE 5

BEAM THEORY DIVERGENCE DYNAMIC PRESSURE PREDICTIONS
FOR THE ALUMINUM MODEL

Sweep	Plate	Model
0	28.96	34.75
-15°	14.02	15.53
-30°	11.46	12.39
-45°	12.27	13.10
-60°	17.52	18.57

Model aerodynamic planform used.

Units: psf

b. CWING Analysis

The early version of CWING was modified for use as a subprogram of an analytical procedure developed for this effort. The main program varied ply orientation, stacking sequence, and sweep, and called CWING to calculate the divergence dynamic pressures. This analysis was qualitative since CWING analyzed wing structures with similar cross section along the span, but the plates had constant thicknesses. For this analysis, wing stiffness was due to the plate alone and aerodynamics were calculated for the entire planform. The divergence dynamic pressures for all of the stacking sequences analyzed are found in Appendix B.

The CWING analysis showed that placing the 0° plies farthest from the wing centerplane resulted in the greatest divergence dynamic pressures. Thus, the $[0_4,(-45,+45)_2]_S$ stacking sequence was chosen as a baseline laminate. Table 6 presents the divergence dynamic pressure results of the CWING analysis for variations of this laminate. The top half of Table 6 illustrates the increase in divergence dynamic pressures due to rotating only the 0° plies.

TABLE 6

CWING DIVERGENCE DYNAMIC PRESSURES FOR VARIATIONS OF THE $[0_4,(-45,+45)_2]_S$ GRAPHITE-EPOXY LAMINATE

Ply Angles (degs)	Sweep 0°	-15°	-30°	-45°	-60°
-5,+45,-45	4.39	4.03	4.54	6.44	13.66
0,+45,-45	8.27	6.64	6.82	9.06	18.36
5,+45,-45	45.43	14.67	11.17	12.59	23.49
10,+45,-45	******	314.94	19.67	15.93	26.61
15,+45,-45	******	******	32.80	16.69	25.56
20,+45,-45	******	******	36.17	14.35	21.49
25,+45,-45	******	******	24.46	11.03	16.94
-5,+40,-50	4.53	4.14	4.64	6.57	13.90
0,+45,-45	8.27	6.64	6.82	9.06	18.36
5,+50,-40	35.03	13.66	10.79	12.36	23.22
10,+55,-35	******	91.40	18.24	15.64	26.51
15,+60,-30	******	******	30.59	16.97	26.27
20,+65,-25	******	******	39.04	15.39	22.95
25,+70,-20	******	******	30.86	12.37	18.64

Units: psf

******: $q_D \geq 10^3$ psf

The lower half of Table 6 demonstrates an increase in divergence dynamic pressures if the whole laminate is rotated. The 7.5° and 15° rotated laminates were chosen since cutting all the composite plates out of one large plate was more economical than constructing plates of three different laminates. In addition, the variation of material properties was minimized. The stacking sequence and rotations were described in Table 1 and Figure 8.

c. TSO Analysis

A sketch of the TSO analytical model is shown in Figure 13. The trapezoidal structural plate in TSO requires parallel root and tip chords so the tip was modified as shown. The dashed lines in the sketch represent the airfoil planform.

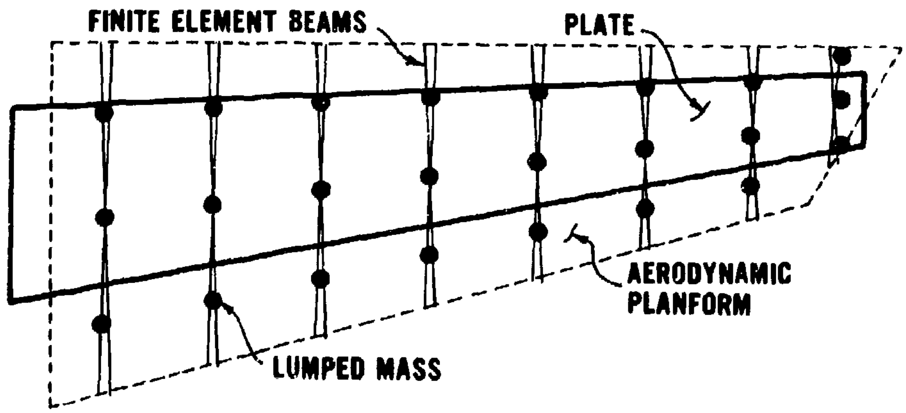

Figure 13. Analytical Model for TSO.

Results from the material properties test and a dimensional check of the finished plate provided the required input data of the plates. The load deflection tests performed on the plates were repeated in the TSO analysis demonstrating a fairly accurate representation of the structural plates.

A comparison of the first six modal frequencies measured experimentally with those calculated analytically showed the analytical values were higher. Since the analytical model was cantilevered at the root, the lower experimental frequencies were attributed to root flexibility. To model the root flexibility, the analytical model was altered slightly by moving the root of the plate inboard (one inch for the aluminum plate and one and one half inches for the graphite epoxy plates). The analytical frequencies for the plates are shown in Table 7.

In order to account for the mass of the airfoil sections in the TSO analytical model, each airfoil section mass was divided into three lumped masses. The section masses and locations for the TSO analysis are given in Table 8. The locations of the masses are shown relative to the plate in Figure 13.

TABLE 7

TSO ANALYSIS PLATE NATURAL FREQUENCIES

Mode	Aluminum	Graphite-epoxy Nonrotated	Graphite-epoxy 7.5° Rotated	Graphite-epoxy 15° Rotated
1B	4.44	5.98	4.91	5.64
2B	23.06	31.13	25.27	29.13
1T	59.11	38.95	46.66	41.94
3B	62.70	84.37	68.99	78.99
2T	143.90	98.93	116.04	106.17
4B	126.26	168.23	142.20	158.90

Units: Hz

TABLE 8

TSO ANALYSIS SLEEVE MASSES AND LOCATIONS

x (in)	y (in)	Weight (lb)	x (in)	y (in)	Weight (lb)
2.60	1.94	.1221	2.39	5.96	.1115
2.17	9.94	.0983	1.95	13.96	.0863
1.73	18.03	.0760	1.52	22.00	.0647
1.31	25.85	.0493	.28	29.30	.0281
6.51	1.94	.0685	5.97	5.96	.0527
5.43	9.94	.0416	4.88	13.96	.0326
4.33	18.03	.0221	3.79	22.00	.0155
3.27	25.85	.0053	1.96	29.30	.0075
10.42	1.94	.0804	9.55	5.96	.0762
8.68	9.94	.0678	7.81	13.95	.0632
6.93	18.03	.0576	6.07	22.00	.0497
5.23	25.85	.0385	3.65	29.30	.0432

The beam element feature of TSO was used to account for the stiffness added to the model by the sleeve. This feature allows bending and torsional rigidity constants to be input to model linear spars and ribs. To simplify assigning values of rigidity, it was assumed that the sleeve sections could be modeled by a pair of crossed beam elements with bending stiffness and no torsional stiffness. The locations are shown in Figure 13. Through iterations of values of bending stiffness, the first three natural frequencies of the analytical model were matched to the frequencies of the wind tunnel model. The locations and stiffness values of the beam are given in Table 9. The final analytical natural frequencies are given in Table 10. The first three natural mode shapes of each model are shown in Appendix A.

TABLE 9

TSO ANALYSIS SLEEVE BEAM ELEMENTS AND LOCATIONS

Leading-edge Endpoint x (in)	Leading-edge Endpoint y (in)	Trailing-edge Endpoint x (in)	Trailing-edge Endpoint y (in)	Bending Stiffness EI x 10^{-3} (lb-in^2) Aluminum	Bending Stiffness EI x 10^{-3} (lb-in^2) Graphite
0.	1.75	12.46	2.25	131.75	240.00
0.	2.25	12.46	1.75	131.75	240.00
0.	5.75	11.38	6.25	105.40	192.00
0.	6.25	11.38	5.75	105.40	192.00
0.	9.75	10.30	10.25	79.05	144.00
0.	10.25	10.30	9.75	79.05	144.00
0.	13.75	9.21	14.25	52.75	96.00
0.	14.25	9.21	13.75	52.75	96.00
0.	17.75	8.13	18.25	26.35	48.00
0.	18.25	8.13	17.75	26.35	48.00
0.	21.75	7.04	22.25	10.54	19.20
0.	22.25	7.04	21.75	10.54	19.20
0.	23.75	5.96	26.25	5.27	9.60
0.	26.25	5.96	25.75	5.27	9.60
0.	29.75	5.43	30.25	1.054	1.92
0.	30.25	5.43	29.75	1.054	1.92

TABLE 10

TSO ANALYSIS WIND TUNNEL MODEL NATURAL FREQUENCIES

Mode	Aluminum	Graphite-epoxy Nonrotated	Graphite-epoxy 7.5° Rotated	Graphite-epoxy 15° Rotated
1B	3.30	3.52	3.38	3.11
2B	16.82	17.78	16.97	15.44
1T	36.15	31.36	31.65	32.81
3B	45.06	46.75	42.47	40.32
2T	83.70	67.14	49.11	61.51
4B	90.18	83.91	79.85	78.63

Units: Hz

After the pretunnel test data was incorporated in the analytical model, divergence and flutter calculations were performed. The aerodynamic paneling for the Woodward and doublet lattice 30° forward sweep analyses are shown in Figure 14 and 15. Similar paneling was developed for the four other sweeps. The divergence dynamic pressure predictions are presented in Table 11 for both the static and dynamic aeroelastic calculations. The flutter dynamic pressures and frequencies calculated in the dynamic analysis are given in Table 12. The flutter mode is a coupling of second bending and first torsion. Frequency and damping versus velocity curves are presented in Appendix C.

TABLE 11

TSO ANALYSIS DIVERGENCE DYNAMIC PRESSURES

					Graphite-epoxy			
	Aluminum		Nonrotated		7.5° Rotated		15° Rotated	
Sweep	Static	Dynamic	Static	Dynamic	Static	Dynamic	Static	Dynamic
0°	42.9	37.6	49.7	40.6	---	192.6	---	486.3*
-15°	16.8	15.9	15.2	14.2	19.2	17.6	21.7	20.1
-30°	13.0	12.6	11.3	11.0	12.2	11.9	11.7	11.3
-45°	13.1	12.1	11.2	10.4	11.5	10.5	10.2	9.5
-60°	16.6	13.9	14.1	11.8	13.8	11.6	11.9	9.9

Units: psf

A comparison of the divergence speeds from the static aeroelastic analysis with those from the dynamic aeroelastic analysis (Table 11) indicates some significant differences in the divergence predictions. Both analyses use identical structural models, therefore the difference must lie in either the aeroelastic eigenvalue equations or in the aerodynamic analyses.

A steady aerodynamic influence coefficient matrix can be calculated in a doublet lattice analysis by choosing a reduced frequency near zero. This steady aerodynamic matrix was substituted for the Woodward aerodynamic matrix in the TSO analysis in order to determine how much difference exists between the static and dynamic calculations of divergence dynamic pressures. Five wing configurations were reanalyzed. The

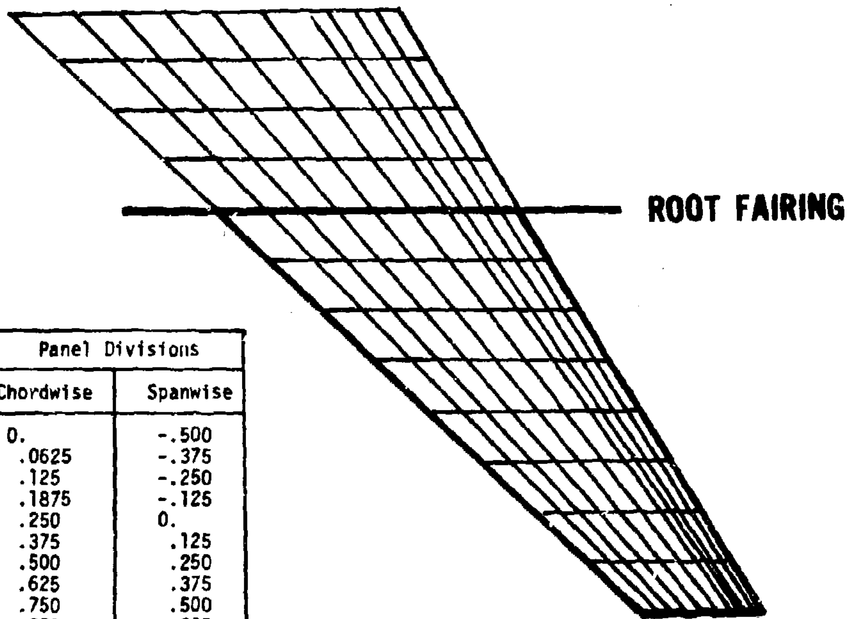

Panel Divisions	
Chordwise	Spanwise
0.	-.500
.0625	-.375
.125	-.250
.1875	-.125
.250	0.
.375	.125
.500	.250
.625	.375
.750	.500
.875	.625
1.000	.750
	.875
	1.0

Figure 14. Woodward Paneling.

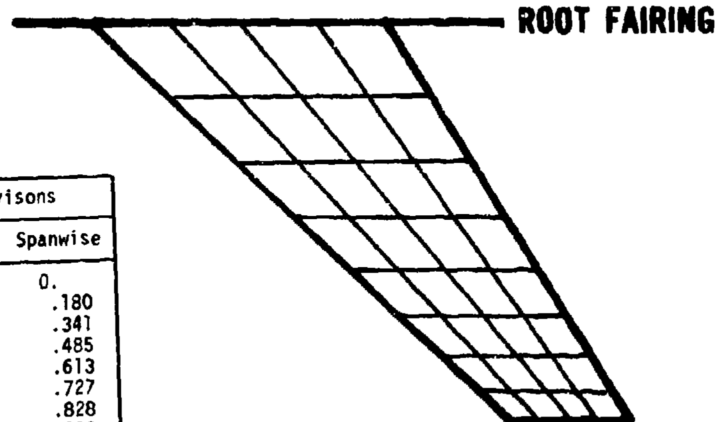

Panel Divisons	
Chordwise	Spanwise
0.	0.
.25	.180
.5	.341
.75	.485
1.00	.613
	.727
	.828
	.919
	1.000

Figure 15. Doublet Lattice Paneling.

TABLE 12

TSO ANALYSIS FLUTTER DYNAMIC PRESSURES AND FREQUENCIES

			Graphite-epoxy					
	Aluminum		Nonrotated		7.5° Rotated		15° Rotated	
Sweep	Dynamic Pressure (psf)	Frequency (Hz)	Dynamic Pressure (psf)	Frequency (Hz)	Dynamic Pressure (psf)	Frequency (Hz)	Dynamic Pressure (psf)	Frequency (Hz)
0°	57.1	23.0	32.7	21.4	39.6	15.9	39.9	14.6
-15°	68.6	22.6	39.1	21.3	42.7	20.5	47.7	20.8
-30°	109.8	20.5	63.0	19.6	61.3	19.7	67.1	19.9
-45°	145.5	8.5	118.4	9.2	145.3	9.1	140.4	6.4
-60°	47.5	14.4	48.1	14.7	37.6	15.0	38.3	13.3

comparisons between the static and dynamic divergence analyses, given in Table 13, show very little difference in the two eigenvalue solutions. Therefore, the difference in divergence results is due to the aerodynamic methods used.

TABLE 13

COMPARISON OF TSO STATIC AND DYNAMIC DIVERGENCE CALCULATIONS

Wing		Divergence Dynamic Pressure (psf)	
Plate	Sweep	Static	Dynamic
Aluminum	0°	37.7	37.6
Graphite-epoxy 7.5° Rotated	-15°	17.8	17.6
Graphite-epoxy 15° Rotated	-30°	11.4	11.3
Graphite-epoxy Nonrotated	-45°	10.4	10.4
Graphite-epoxy 7.5° Rotated	-60°	11.8	11.6

Two attempts were made to resolve the differences in the aerodynamics. The first was in the location of the panel center of pressure. The Woodward analysis assumes a center of pressure located at the panel midchord, and the doublet lattice analysis assumes a quarter chord center of pressure location. For a fine paneling grid, the location of the center of pressure should have no effect. However, the grids used in these analyses are fairly coarse. The aerodynamic analyses were performed at a Mach number of 0.13. For speeds in this range, the flow is such that the center of pressure should be near the quarter chord, therefore the Woodward routine was altered to perform calculations with the center of pressure at the quarter chord.

By moving the center of pressure forward the twisting moment due to the same load will be greater and, hence, the divergence speeds will be lower. The TSO analysis was performed once again with the recalculated steady aerodynamic matrix on the same wing configurations used to compare the eigenvalue problems. Table 14 has a comparison of the divergence speeds for each of the five cases. As expected, the divergence speeds calculated by the static aeroelastic method did decrease.

The second attempt at resolving the difference in the aerodynamics was to increase the fineness of the Woodward paneling without altering the center of pressure location. The number of panels shown in Figure 14 was doubled, the aerodynamics recalculated, and divergence analyses performed. The results, Table 14, show a decrease in the divergence speeds comparable to the results obtained by changing the center of pressure location.

TABLE 14

CHANGE IN TSO DIVERGENCE CALCULATIONS DUE TO WOODWARD CENTER OF PRESSURE LOCATION AND AERODYNAMIC PANELING

Wing		Divergence Dynamic Pressure (psf)			
Plate	Sweep	C_p at .5c	C_p at .25c	160 Panels	Dynamic
Aluminum	0°	42.9	40.7	40.5	37.6
Graphite-epoxy 7.5° Rotated	-15°	19.2	18.6	18.6	17.6
Graphite-epoxy 15° Rotated	-30°	11.7	11.5	11.4	11.3
Graphite-epoxy Nonrotated	-45°	11.2	10.8	11.0	10.4
Graphite-epoxy 7.5° Rotated	-60°	13.8	13.1	13.5	11.6

d. NASTRAN Analysis

The NASTRAN model used for stress analysis is presented in Figure 16. The highest steady airload expected during testing was applied to the model. This airload condition occurs at 0° sweep, 3° angle of attack, and 80% of the predicted divergence velocity for the unrotated composite laminate. A maximum strain of one seventh of the ultimate strain was predicted in the plies located near the root of the model

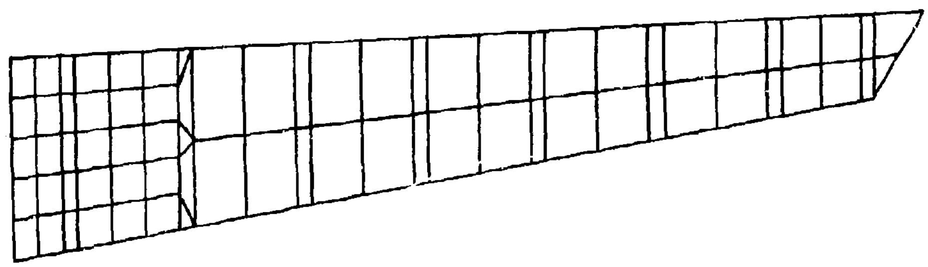

Figure 16. NASTRAN Model for Stress Analysis.

which indicated a sufficient margin of safety for wind tunnel testing at this load condition.

The NASTRAN vibration analysis was accomplished with the model shown in Figure 17. The model included the internally calculated plate mass, inertia and stiffness, the measured mass and inertia characteristic of the sleeve, and the additional stiffness of the sleeve. The mass and inertial characteristics of each sleeve section, given in Table 3, were simulated by pairs of equal masses, balanced about the section center of gravity. The additional torsional stiffness of the sleeve was simulated by rigidly connecting the six bridge end points local rotational degrees of freedom about the spanwise axis running parallel to the wing leading edge. These two modifications to the basic plate analytical model effectively accounted for the sleeve's influence on the model.

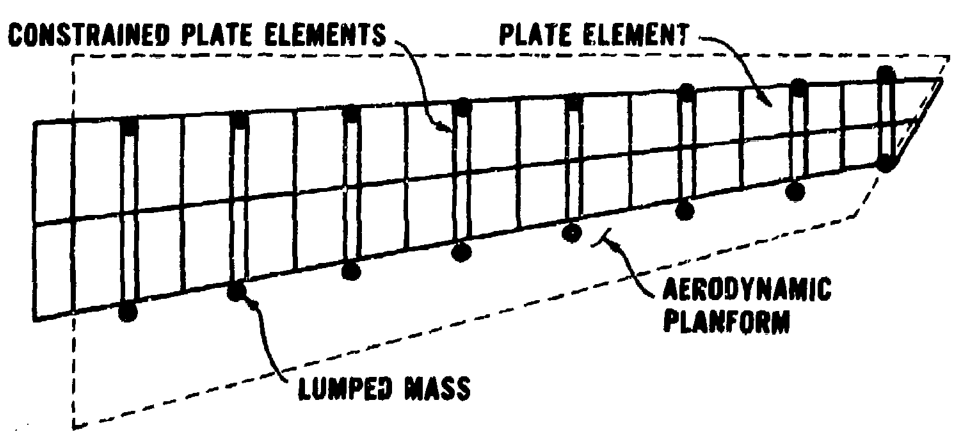

Figure 17. NASTRAN Model for Dynamic Analysis.

The ground vibration test revealed the analytical frequencies and mode shapes were not accurate. This problem was solved by locating the cantilevered root of the analytical model 1.5 inches inboard to compensate for the mount flexibility. The NASTRAN calculated natural frequencies are presented in Table 15. Good correlation in frequency and mode shapes was obtained for the four plate models. The largest discrepancy occurred with the aluminum plate model data where the analytical fifth and sixth modes occurred in reverse order. This was not considered a problem as only the first three modes were used in the flutter and divergence calculations. The NASTRAN mode shapes for each plate model are presented in Appendix A.

TABLE 15

NASTRAN ANALYSIS WIND TUNNEL MODEL NATURAL FREQUENCIES

Mode	Aluminum	Graphite-epoxy		
		Nonrotated	7.5° Rotated	15° Rotated
1B	3.20	3.51	3.37	3.11
2B	16.30	17.75	17.10	15.66
1T	36.12	32.31	31.73	31.36
3B	42.94	46.51	44.91	41.01
2T	85.23	70.28	69.23	69.19
4B	82.83	88.93	86.09	78.55

Units: Hz

Once the vibration models gave satisfactory results, the flutter and divergence calculations were accomplished. The frequency versus velocity and damping versus velocity plots obtained from NASTRAN for each of the twenty plate/sweep angle combinations are contained in Appendix C. In every case, the first bending mode was the mode that diverged. However, flutter occurred before divergence in some models at the zero sweep angle. The flutter and divergence predictions from NASTRAN are presented in Tables 16 and 17.

TABLE 16

NASTRAN ANALYSIS FLUTTER DYNAMIC PRESSURES

Sweep	Aluminum	Graphite-epoxy Nonrotated	Graphite-epoxy 7.5° Rotated	Graphite-epoxy 15° Rotated
0°	56.9	34.4	36.2	37.4
-15°	66.3	39.5	39.8	42.0
-30°	91.2	53.2	50.9	52.5
-45°	139.3	113.6	125.8	126.9
-60°	94.2	88.9	87.2	76.7

Units: psf

TABLE 17

NASTRAN ANALYSIS DIVERGENCE DYNAMIC PRESSURES

Sweep	Aluminum	Graphite-epoxy Nonrotated	Graphite-epoxy 7.5° Rotated	Graphite-epoxy 15° Rotated
0°	36.6	39.6	93.2	185.4
-15°	15.3	14.4	17.8	21.2
-30°	11.7	10.6	11.3	11.2
-45°	11.3	10.0	10.1	9.3
-60°	12.4	10.9	10.6	9.4

Units: psf

SECTION V

WIND TUNNEL TESTING AND CORRELATION OF RESULTS

1. WIND TUNNEL TESTING AND PROJECTION METHODS

The nature of divergence does not allow testing near the divergence velocity because there is usually little chance of recovery. Since 20 wing configurations were to be tested, each with the same foam sleeve, it was necessary to use a testing technique that limited the possibility of damage to the sleeve, as well as the plates and wind tunnel.

The subcritical divergence testing began at 50% of the analytically predicted divergence velocity. At this velocity, the model was positioned at the angle of attack where no bending strain was observed. The model angle of attack was increased in increments of one degree, and bending and torsional strain readings were recorded at the nominal angles of attack of 1, 2 and 3°. The model was returned to the initial angle of attack, the tunnel dynamic pressure was increased, and strain readings were again taken at the three angles of attack.

A minimum of six dynamic pressures and therefore six sets of strain readings were recorded up to 80% of the projected divergence velocity. The divergence velocity was projected by two techniques, the divergence index method and a Southwell-type method, which were programmed in a hand-held calculator. As each set of data was read, it was stored in the calculator and the divergence velocity projections were updated.

The divergence index method was developed at the NASA Langley Research Center. The discussion given here was obtained by the authors from Mr. W. H. Reed, Chief of the Aeroelasticity Branch at the NASA Langley Research Center. For the wing shown in Figure 18, the lift of the wing is the sum of the rigid lift due to angle of attack, α, and the incremental lift due to the angle of attack induced by the flexibility, θ, of the wing

$$L = qSC_{L_\alpha}(\alpha + \theta) \tag{5}$$

The restoring force of the wing

$$F_r = k\theta \tag{6}$$

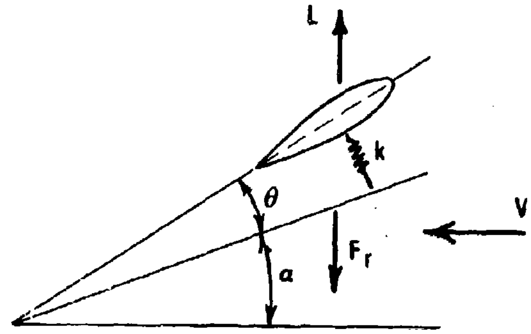

Figure 18. Wing Angle of Attack Components.

(where k represents the stiffness of the wing structure) is equal to the wing lift.

Equating Equations 5 and 6, and rearranging terms

$$\theta = \frac{qSC_{L_\alpha}\alpha}{k-qSC_{L_\alpha}} \tag{7}$$

At divergence the denominator of Equation 7 is equal to zero. Thus the restoring force is just able to counter the flexible lift, giving

$$q_D SC_{L_\alpha} = k \tag{8}$$

and the divergence dynamic pressure is

$$q_D = \frac{k}{SC_{L_\alpha}} \tag{9}$$

Substituting Equation 8 into Equation 7 and solving for the angle of attack as a function of the angle of attack induced by the wing flexibility results in

$$\alpha = \left(\frac{q_D}{q} - 1\right)\theta \tag{10}$$

Measuring strain in the wind tunnel model with a strain gage located on the plate near the root provides an indication of the wing deflection due to the flexible lift. The relation of strain to deflection is

$$\theta = B\varepsilon \tag{11}$$

where B is a constant. Substituting Equation 11 into Equation 10 results in

$$\alpha = \left(\frac{q_D}{q} - 1\right)B\varepsilon \tag{12}$$

which illustrates that the strain varies linearly with angle of attack for a constant dynamic pressure.

The slope of the angle of attack versus strain curve for the nth dynamic pressure is

$$\lambda_n = \frac{d\alpha}{d\varepsilon} = B(\frac{q_D}{q_n} - 1) \tag{13}$$

Dividing the slope of the first dynamic pressure line by the slope of the nth dynamic pressure line results in the equation

$$\frac{\lambda_1}{\lambda_n} = \frac{B(q_D/q_1 - 1)}{B(q_D/q_n - 1)} = \frac{q_n/q_1 - q_n/q_D}{1 - q_n/q_D} \tag{14}$$

The divergence index is defined as

$$\Delta_n = \frac{1 - q_n/q_1}{1 - \lambda_1/\lambda_n} \tag{15}$$

and when substituted into Equation 14, results in

$$\Delta_n = 1 - \frac{q_n}{q_D} \tag{16}$$

Thus, the divergence index varies linearly with the dynamic pressure. As the dynamic pressure approaches the divergence dynamic pressure, the divergence index approaches zero. An example of the use of the divergence index is outlined in the following paragraphs.

The angle of attack versus strain data for the nonrotated model at -15° sweep is presented in Table 18 and shown plotted in Figure 19. The slope for the first set of data is calculated and used as the reference. The slope for each subsequent set of data is calculated and substituted into Equation 15 to calculate the divergence indices which are tabulated in Table 19.

The divergence indices are plotted versus dynamic pressure in Figure 20. For a dynamic pressure of zero the divergence index is one, therefore, the linear relation between the divergence index and the dynamic pressure is fitted by a least squares method and forced through $\Delta_n = 1$. The divergence dynamic pressure is the intersection of this line and the dynamic pressure axis. For this example, the divergence dynamic pressure is projected to be 11.9 psf.

TABLE 18

DYNAMIC PRESSURE AND STRAIN DATA FOR THE NONROTATED MODEL, $\Lambda = -15°$

Dynamic Pressure (psf)	Strain (mv)		
	$\alpha = 1°$	$\alpha = 2°$	$\alpha = 3°$
4.03	.325	.655	.980
4.73	.409	.830	1.230
5.48	.540	1.068	1.650
5.88	.600	1.200	1.870
6.29	.713	1.500	2.230
6.72	.830	1.667	2.500

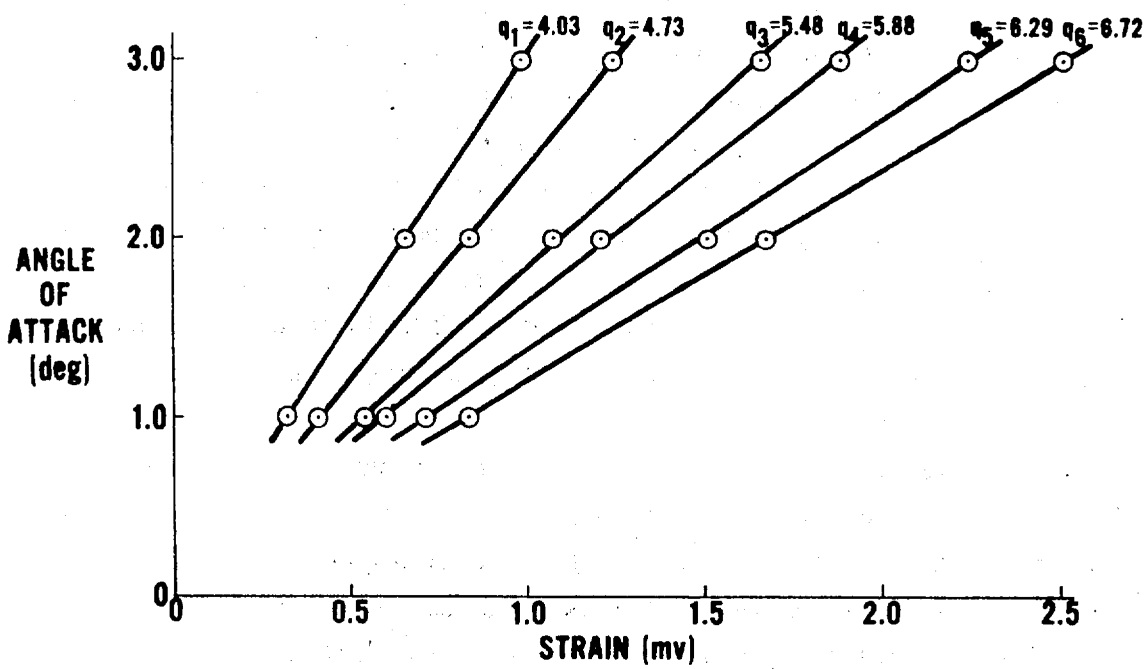

Figure 19. Angle of Attack versus Strain Data for the Nonrotated Model, $\Lambda = -15°$.

TABLE 19

DIVERGENCE INDEX PROJECTIONS
FOR THE NONROTATED MODEL, Λ = -15°

Dynamic Pressure (psf)	Divergence Index Δ	Divergence Projection (psf)
4.03	-	-
4.73	.688	15.1
5.48	.520	12.9
5.88	.490	12.4
6.29	.428	11.9
6.72	.432	11.9

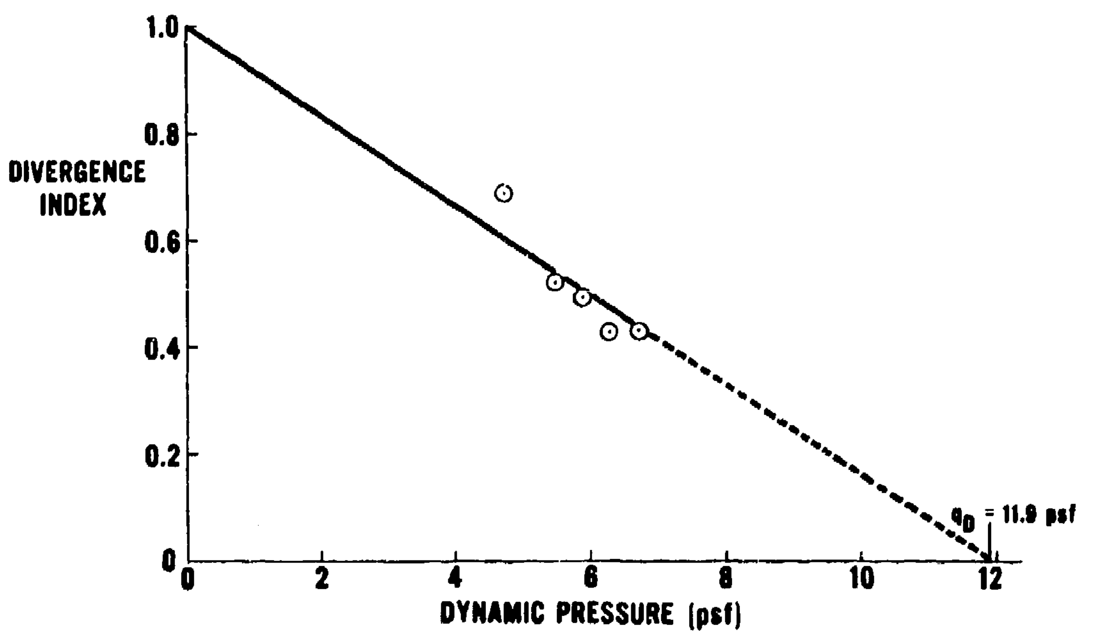

Figure 20. Divergence Index Projection of Divergence Dynamic Pressure for the Nonrotated Model, Λ = -15°.

The second subcritical projection method used in the wind tunnel testing is an adaptation of Southwell's technique [17]. Southwell's technique was originally developed to project beam buckling by reducing the influence of geometric imperfections. The similarity between wing divergence and conventional buckling of structures has been noted by many (Reference 18 is one example). In discussions concerning wind tunnel testing for divergence, it was proposed that a Southwell type technique could be used as a subcritical projection method.

Equation 12 can be rearranged as follows

$$\frac{\varepsilon}{q} = \frac{1}{q_D B}(\alpha + B\varepsilon) \tag{17}$$

For constant angle of attack, Equation 17 is a linear relationship between ε/q and ε where the slope is the inverse of the divergence dynamic pressure:

$$\frac{d(\varepsilon/q)}{d\varepsilon} = 1/q_D \tag{18}$$

Equation 18 is analogous to the relation between load and beam deflection in Reference 17.

As in the case of the divergence index method, strain is measured at each dynamic pressure and angle of attack. For two or more dynamic pressures, the strain data at constant angle of attack is fitted by a least squares method. The inverse of the slope of this fit is the projected divergence dynamic pressure. As new strain data is collected, the divergence dynamic pressure is updated, as shown in Table 20 for the data presented in Table 18. The data obtained for the nonrotated model is presented in Figure 21. The subcritical projections compare favorably with the divergence index projections.

Each of the 20 wing configurations was tested subcritically using both the divergence index and Southwell methods. Only the projections are presented in this report since the compilation of the intermediate data is voluminous. However, one set of data, the data for a configuration that is divergence free, is interesting enough to include in this report.

Table 21 is a tabulation of the dynamic pressure, angle of attack and strain data obtained while testing the 15° rotated model at 0°

TABLE 20

SOUTHWELL DIVERGENCE PROJECTIONS
FOR THE NONROTATED MODEL, Λ = -15°

Dynamic Pressure (psf)	Divergence Dynamic Pressure Projection (psf)		
	α = 1°	α = 2°	α = 3°
4.03	-	-	-
4.73	14.4	13.5	14.8
5.48	11.9	12.7	11.4
5.88	12.4	13.0	11.6
6.29	11.9	11.3	11.1
6.72	11.7	11.4	11.4

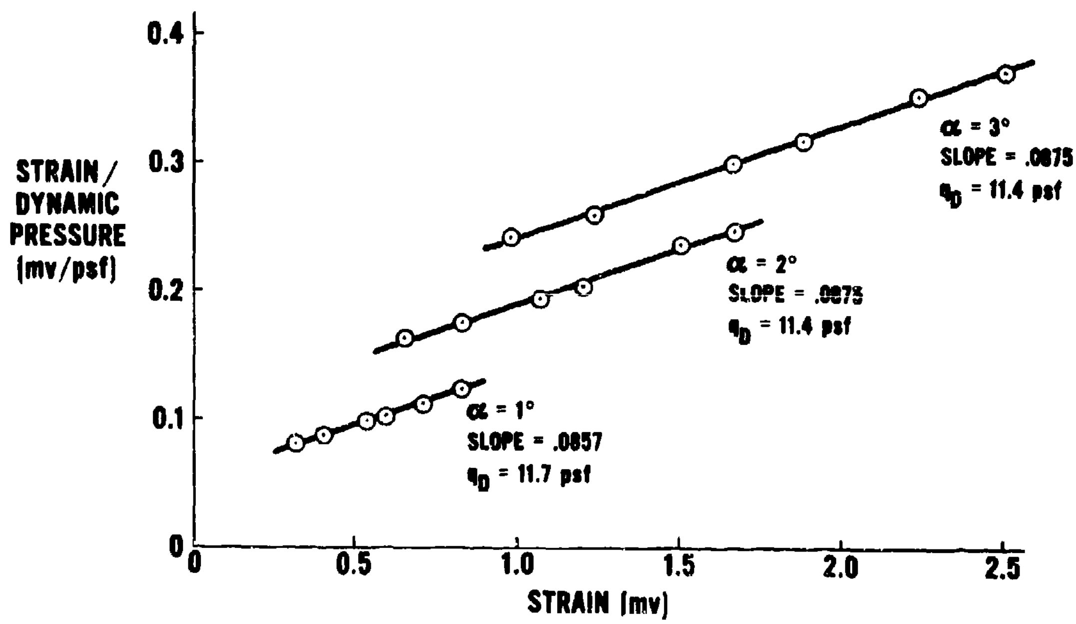

Figure 21. Southwell Plot for the Nonrotated Model, Λ = -15°.

sweep. The slopes from the angle of attack versus strain data, Figure 22, were used in the calculation of the divergence index. Figure 23 is the divergence index plot and, although there is a lot of scatter, the trend is obvious. The divergence index for a divergence-free wing is greater than 1.0

The Southwell plot is shown in Figure 24. Again, there is scatter in the slopes, yet a trend exists. For a divergence-free wing the Southwell plot slope is negative.

After subcritical testing was completed on the 20 configurations, the aluminum model at -30° sweep was selected to obtain a "hard", or actual, divergence data point. The Southwell-type subcritical divergence projection technique was used up to 80% of the divergence velocity. The wing angle of attack was adjusted to minimize the bending strain and fixed for the remainder of the run. The velocity of the tunnel was raised incrementally until the wing divergence occurred at which time the wind tunnel was immediately shut down.

Fortunately, divergence did not cause damage to the model. As previously described, the airfoil sleeve was sectioned in order to reduce the stiffness. However, under the large deflections associated with the diverging model, the sleeve sections pressed against one another causing the sleeve to restrain the model. This characteristic of the model made it possible to find the actual divergence points for each of the four models. Several repeated cases demonstrated that the models gave consistent divergence results. The models were not tested to divergence at the -60° sweep position because of the greater possibility of damage due to the sleeve striking the fairing. Similarly, no divergence points were obtained at zero sweep because of the possibility of encountering a high frequency (~25 Hz) flutter instability.

2. DISCUSSION OF RESULTS AND CORRELATION

The divergence dynamic pressures measured during the wind tunnel tests have been nondimensionalized by plate weight divided by plate area and plotted versus wing leading edge sweep in Figure 25. For those configurations where the actual divergence points were not obtained the Southwell predictions were plotted. All of the divergence dynamic pressures, analytical and experimental, are presented in Table 22.

TABLE 21

DYNAMIC PRESSURE AND STRAIN DATA FOR THE 15° ROTATED MODEL, $\Lambda = 0°$

Dynamic Pressure (psf)	Strain (mv) $\alpha = 1°$	$\alpha = 2°$	$\alpha = 3°$
5.48	.600	1.012	1.400
6.29	.655	1.122	1.534
7.16	.726	1.233	1.703
8.08	.816	1.385	1.917
9.06	.912	1.483	2.034
10.10	.962	1.638	2.278
11.19	1.060	1.757	2.439

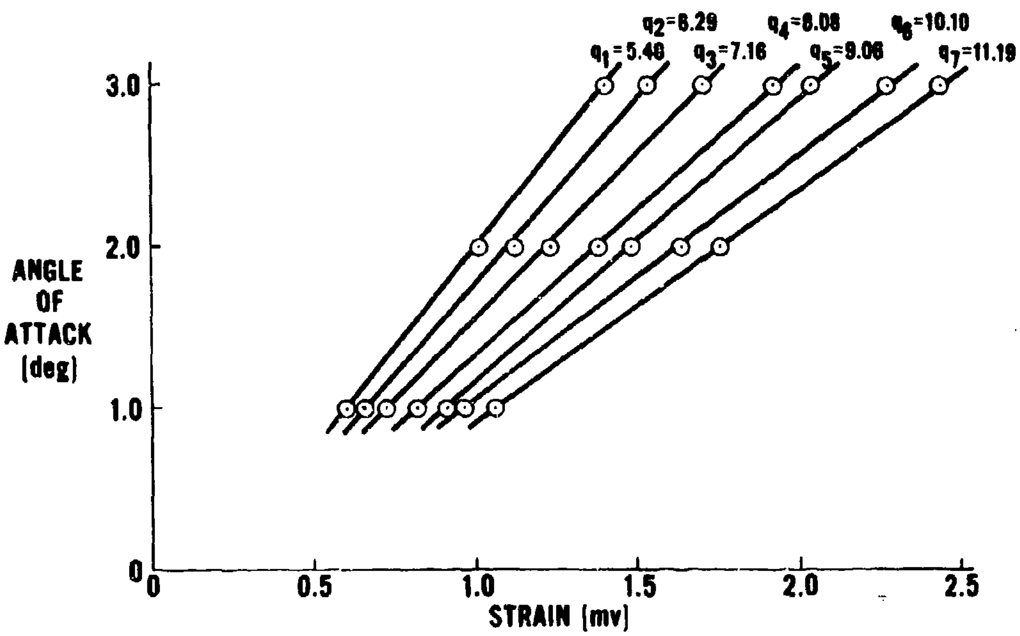

Figure 22. Angle of Attack versus Strain Data for the 15° Rotated Model, $\Lambda = 0°$.

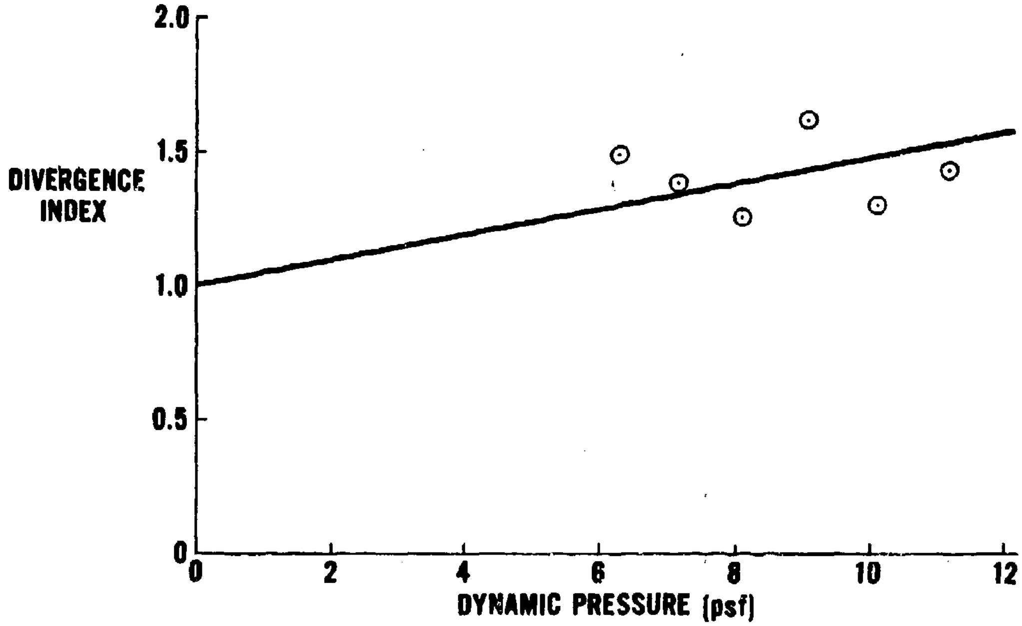

Figure 23. Divergence Index Projection for the 15° Rotated Model, Λ = 0°.

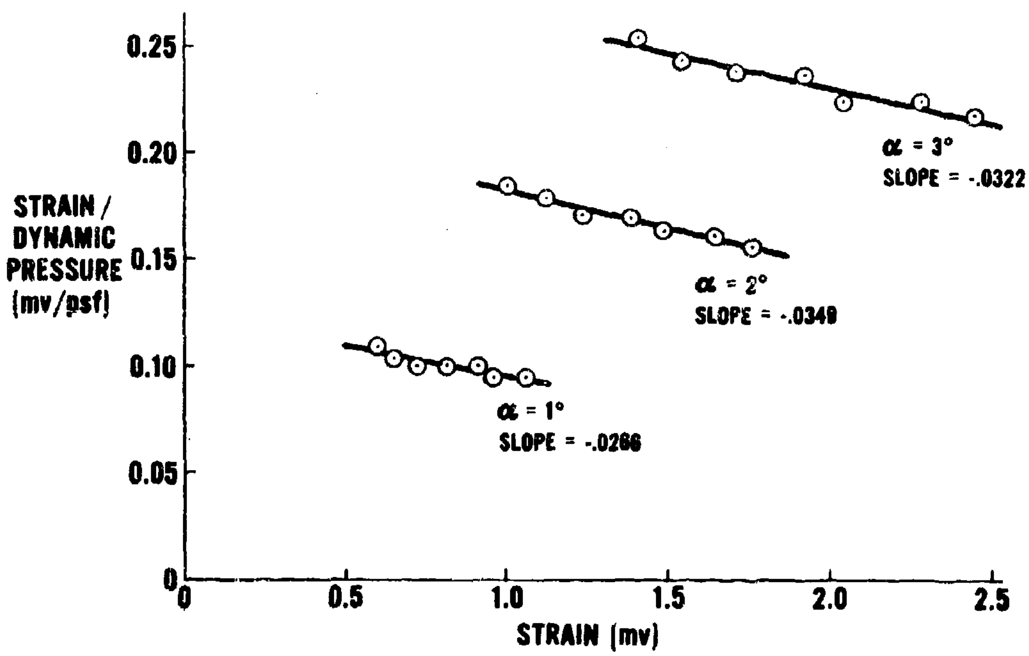

Figure 24. Southwell Plot for the 15° Rotated Model, Λ = 0°.

TABLE 22

DIVERGENCE DYNAMIC PRESSURES

		Test		NASTRAN		TSO			
	Sweep	Actual	Southwell	Doublet Lattice (1)*	Doublet Lattice (2)*	Doublet Lattice (1)*	Doublet Lattice (2)*	Woodward (1)*	Woodward (2)*
Aluminum	0°	--	34.4	36.6		37.4		42.3	
	-15°	15.5	15.9	15.3		15.8		16.9	
	-30°	12.3	11.3	11.7		12.6		13.1	
	-45°	11.5	10.4	11.3		12.1		13.1	
	-60°	--	11.9	12.4		13.8		16.6	
Nonrotated Graphite-epoxy	0°	--	21.7	39.6	28.8	39.7	27.0	49.6	32.8
	-15°	11.4	11.2	14.4	12.8	14.2	12.3	15.3	13.4
	-30°	10.1	8.5	10.6	9.9	11.0	10.1	11.4	10.5
	-45°	9.2	8.5	10.0	9.7	10.4	9.9	11.2	10.7
	-60°	--	9.3	10.9	10.7	11.7	11.6	14.1	13.8
7.5° Rotated Graphite-epoxy	0°	--	116.1	93.2	75.7	82.6	250.4†	203.8	∞
	-15°	16.9	17.6	17.8	17.1	17.4	17.4	18.7	19.2
	-30°	11.7	10.5	11.3	11.1	11.6	11.7	12.1	12.2
	-45°	10.1	9.5	10.1	10.1	10.3	10.5	11.2	11.3
	-60°	--	9.8	10.6	10.6	11.2	11.4	13.5	13.7
15° Rotated Graphite-epoxy	0°	--	∞	185.4	173.3	∞	∞	1407.5	614.4
	-15°	--	29.3	21.2	23.0	19.2	23.6	20.9	26.2
	-30°	12.1	10.9	11.1	11.4	11.1	11.7	11.5	12.2
	-45°	9.8	8.9	9.3	9.5	9.3	9.5	10.1	10.3
	-60°	--	7.2	9.4	9.5	9.8	9.6	11.8	11.8

*(1) Analysis based on GVT performed before the wind tunnel test.
*(2) Analysis based on GVT performed after the wind tunnel test.
†1st torsion divergence mode.

Units: psf

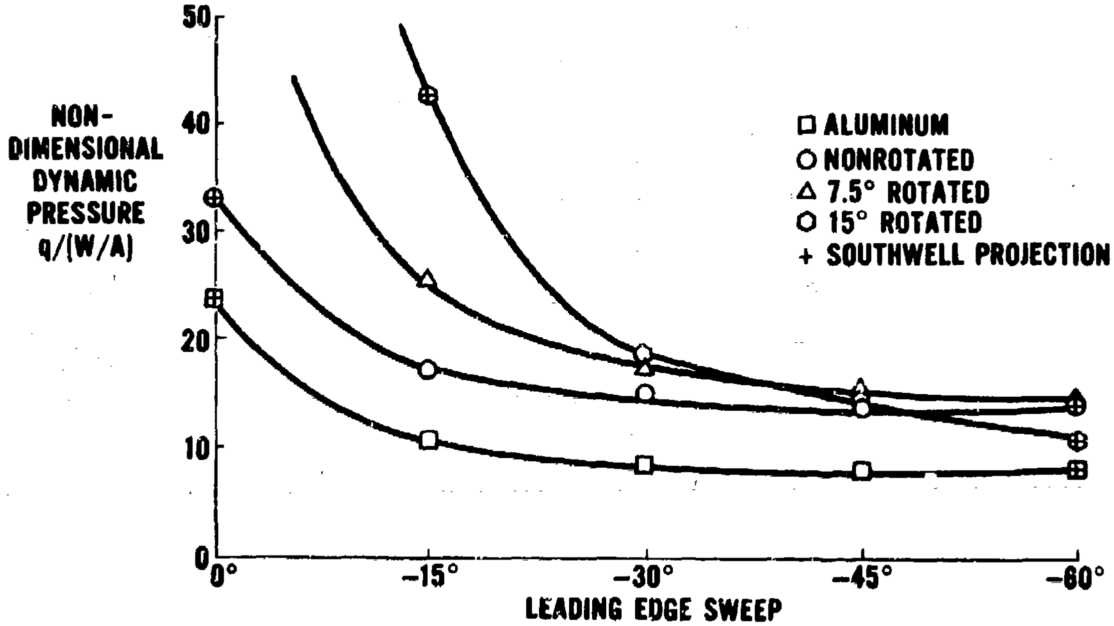

Figure 25. Nondimensional Divergence Dynamic Pressures versus Sweep.

Two observations concerning the use of a composite material in place of aluminum can be made from the comparison in Figure 25. One is that for all sweeps the composite plates are more effective per unit weight than the aluminum plate in preventing divergence. The second observation is that the divergence speed of the model could be altered by simply rotating the composite laminate in relation to the reference line of the wing. This is especially evident at sweep angles between 0° and -20° where forward rotation of the composite laminate has the greatest effect.

Rotating the laminate is a form of aeroelastic tailoring. The effect of laminate rotation may be further appreciated by studying Figure 26 which presents the laminate bending and torsional stiffness and the coupling parameter for each of the composite plates as defined by the method of Reference 5. Torsional stiffness is nearly constant between plus and minus 5° rotation and increases sharply at higher rotation angles. At 15° rotation, torsional stiffness is about 60% higher than at 0° rotation. The coupling parameter has a nearly constant slope, increasing negatively from 0° rotation. Negative coupling parameter produces a wash-out, bend-twist characteristic about the

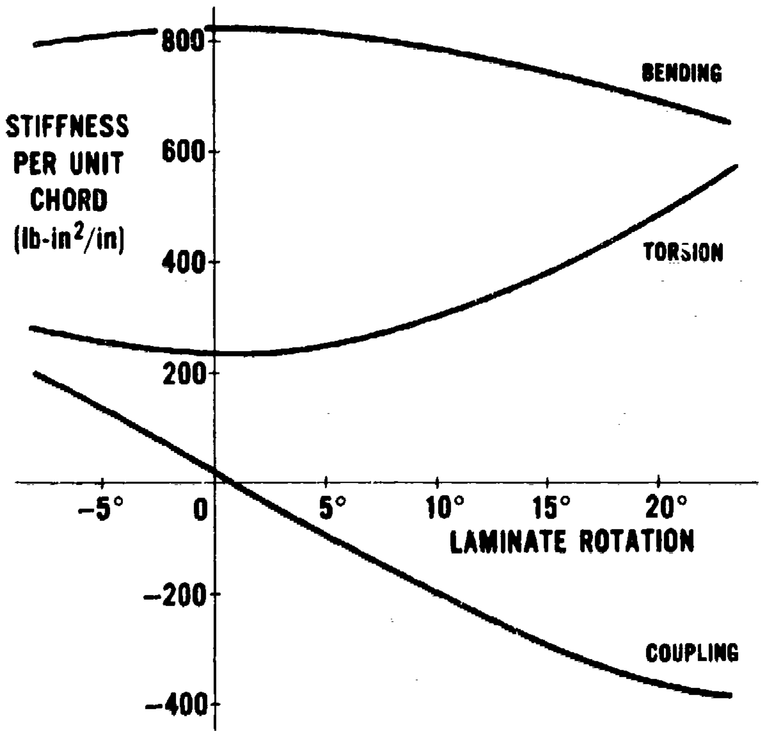

Figure 26. Stiffness Variation Due to Rotation of $[0_4,(-45,+45)_2]_S$ Graphite-epoxy Laminates.

structural axis. At the low forward sweeps, the divergence mode is primarily a torsion mode. Therefore, the increasing torsional stiffness and decreasing coupling parameter due to 15° rotation have the greatest effect countering the wash-in tendencies and increasing the divergence speed.

Figure 25 shows that the 15° rotated model has the lowest divergence dynamic pressure of the three composite models at -60° sweep. At -45° sweep, the 15° rotated model has a divergence dynamic pressure that is less than the 7.5° rotated model. At the greater forward sweeps, the divergence mode is primarily bending and bending stiffness becomes predominant in determining divergence dynamic pressure. Figure 26 shows the bending stiffness is nearly constant over the ±5° rotation range, but is about 11% less for 15° rotation than for the nonrotated laminate. Although the torsional stiffness and wash-out coupling are greatest for this laminate, the bending stiffness is lowest resulting in low divergence speeds at the greater forward sweeps.

Figure 27 presents the "hard" divergence points compared with the subcritical projections based on the Southwell method for the 7.5° rotated model. Similar results were obtained for the other models. The Southwell method projected divergence dynamic pressures within 10% for the configurations where subcritical data were obtained at test points greater than 50% of the divergence dynamic pressure. It was not possible to obtain data at 50% of the divergence dynamic pressures for the 0° sweep cases due to the low flutter speeds. Therefore, the quality of convergence of the projections at 0° sweep was poor.

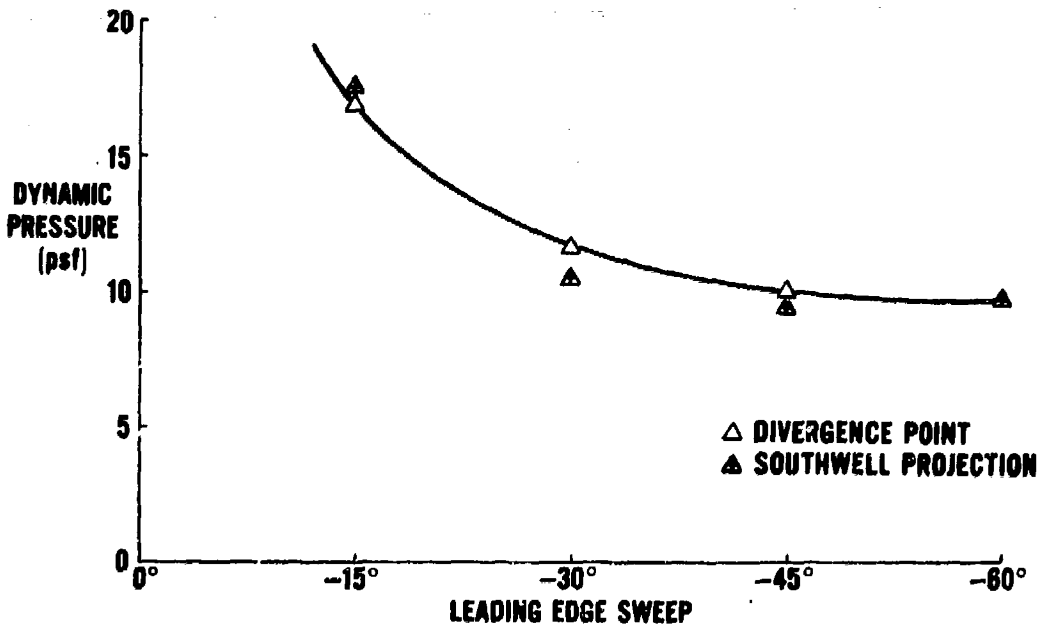

Figure 27. Comparison of Measured and Projected Divergence Dynamic Pressures for the 7.5° Rotated Model.

As seen in Figure 28 for the aluminum model, the divergence dynamic pressure decreases rapidly when the wing is swept from 0° to -15° and remains nearly constant from -30° to -60° sweep. This trend is predicted very well by TSO and NASTRAN analyses. The TSO and NASTRAN analytical predictions using doublet lattice aerodynamics are in close agreement with the experimental data. As discussed in a previous section, the TSO analysis with Woodward aerodynamics consistently predicts slightly higher divergence dynamic pressures than the TSO analysis with doublet lattice aerodynamics.

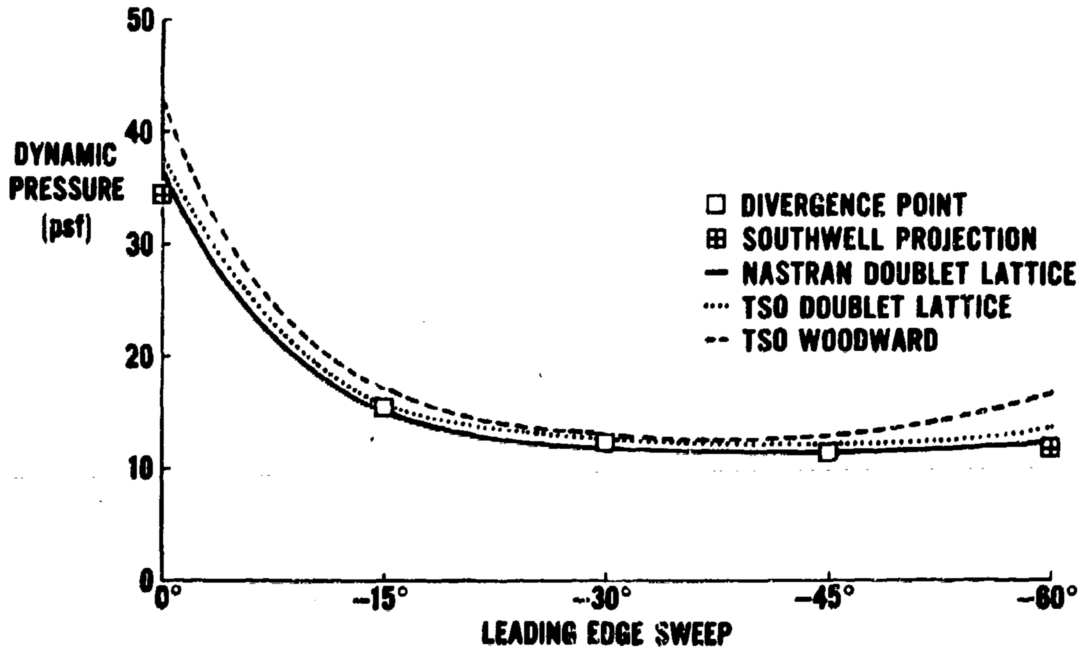

Figure 28. Comparison of Analytical and Test Divergence Dynamic Pressures for the Aluminum Model.

The analytical and test divergence data for the nonrotated model are presented in Figure 29. For the 0° sweep case, the flutter dynamic pressure was lower than the divergence dynamic pressure. Consequently, testing was restricted to below 35% of the divergence dynamic pressure, and the subcritical projections did not converge. The correlation between test and analytical divergence dynamic pressures at -15° sweep is poor. This poor correlation caused concern, and thus, vibration and load-deflection tests were performed after the wind tunnel tests. The results and a discussion of the results are presented later in this section of the report.

Figure 30 presents the analytical and test divergence data for the 7.5° rotated model. Rotation of the laminate 7.5° forward of the reference line significantly increases the divergence dynamic pressure at 0° sweep. As was the case for the nonrotated composite plate at this sweep, the Southwell divergence projection did not converge because it was not possible to test to sufficiently high dynamic pressures due to the low flutter speeds. The calculated divergence dynamic pressure at 0° sweep for the 7.5° rotated model was at least four times the

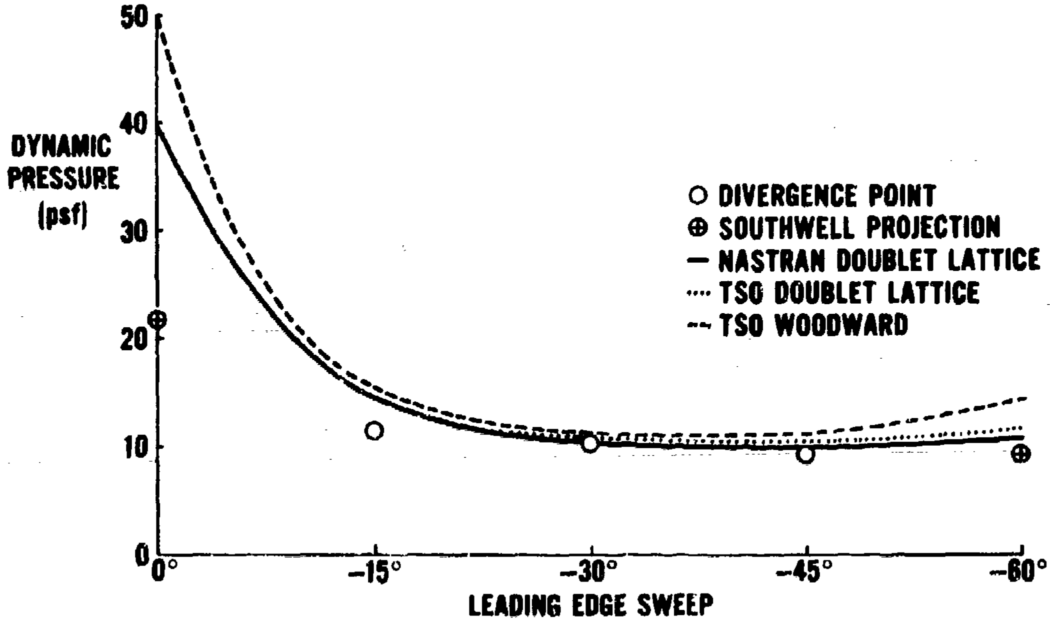

Figure 29. Comparison of Analytical and Test Divergence Dynamic Pressures for the Nonrotated Model.

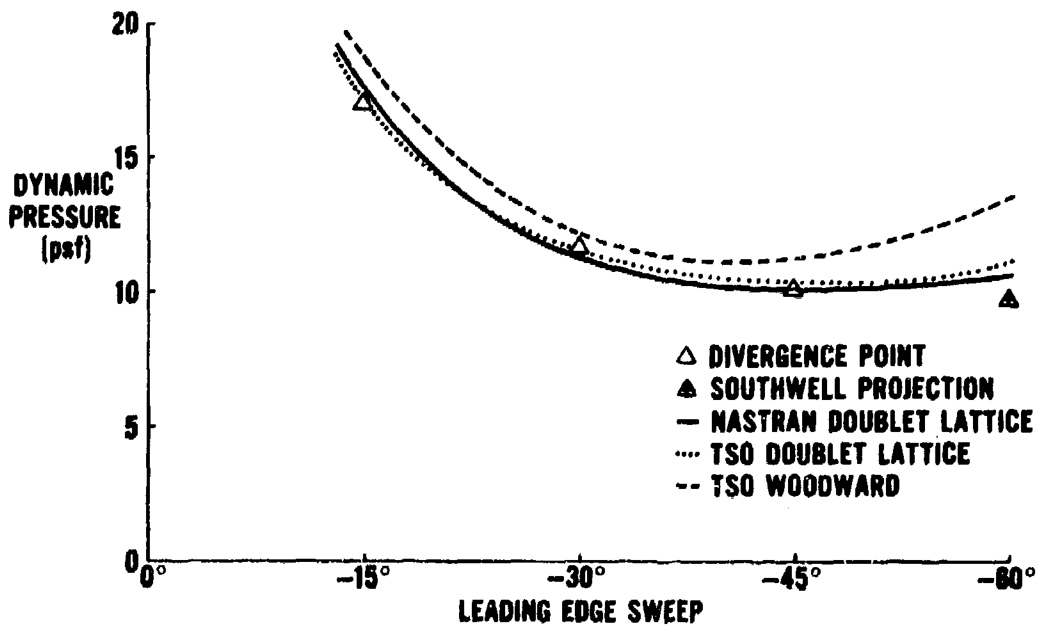

Figure 30. Comparison of Analytical and Test Divergence Dynamic Pressures for the 7.5° Rotated Model.

divergence dynamic pressure for the nonrotated model (Table 22). The NASTRAN and TSO doublet lattice analytical results compare very well with test data for this plate at sweeps greater than 15° forward. The TSO-Woodward analytical results are consistently higher than the test data.

Figure 31 presents the analytical and test divergence data for the 15° rotated model. As seen in this figure and in Table 20, the analytical divergence dynamic pressure is very high at 0° sweep. As discussed earlier, the subcritical techniques indicated a divergence-free wing for this plate and sweep. At -15° sweep, divergence was very difficult, if not impossible, to define. Subcritical projections were obtained, but as the tunnel dynamic pressure was increased, the projected divergence dynamic pressure increased. An unusual phenomenon, a low amplitude, low frequency (0.5 Hz) sinusoidal oscillation of the wing, occurred at approximately the analytically predicted divergence speed. As the dynamic pressure increased, the amplitude of the oscillation increased while the frequency remained constant. The cause of the phenomenon and its mechanism are not understood. It is not predicted by any of the analytical methods and thus may be associated with a characteristic of the model tested. Thus a meaningful comparison between the analytical and test results is not possible. At -30° and -45° sweep, comparisons of analytical and test results are good. However, at -60° sweep, the Southwell projection is 12.4% less than the lowest analytical prediction. Also, the trend of increasing divergence dynamic pressure predicted by the analysis for sweeps greater than 45° forward is opposite to the trend observed in the test results.

The divergence characteristics varied with sweep angle and structural plate. Generally, the severity of divergence, described as the rate of change of deflection as the wing diverged, was greater at the higher forward sweep angles. Rotating the composite laminate forward lessened the severity of the divergence at all forward sweep angles where "hard" divergence points were obtained. At -15° sweep, the rate of deformation associated with divergence was mild, while at -45° sweep, the rate was rapid. The rapid rate of deformation caused the sleeve sections to compress as a spring which resulted in a post-divergence oscillation (7 Hz).

At -60° sweep, the test results are consistently lower than all of the analytical results for all models. Previous testing involving the

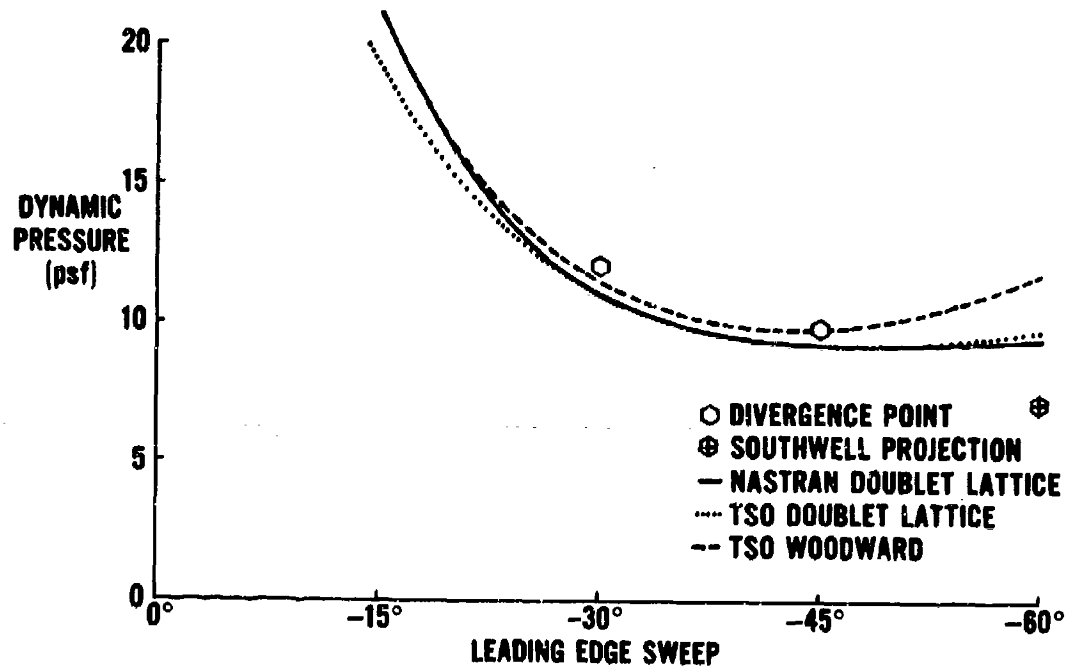

Figure 31. Comparison of Analytical and Test Divergence Dynamic Pressures for the 15° Rotated Model.

fairing revealed that turbulence was generated around the cavity of the fairing. For this test, cover plates were used to minimize the cavity and reduce the turbulence. The size of the cavity was largest at -60°. The turbulence generated by the fairing cavity could have affected the aerodynamic loading on the inboard aft portion of the model. Thus the center of pressure would be more forward. Since the analysis does not account for the turbulence near the fairing, the calculated center of pressure would be further aft than the actual location on the model. For -60° sweep, the effect of cavity turbulence would be greatest, possibly explaining the difference between the analytical and test results.

The effect of laminate rotation on loading is illustrated in Figure 32. Measured strain is plotted versus dynamic pressure for the nonrotated and 15° rotated models for -30° sweep at 3° angle of attack. For dynamic pressures greater than 50% of the divergence dynamic pressure of the nonrotated model, the strain level is lower for the 15° rotated model than for the nonrotated model. Therefore, increasing the divergence dynamic pressure by laminate rotation decreased the level of strain under aerodynamic loading.

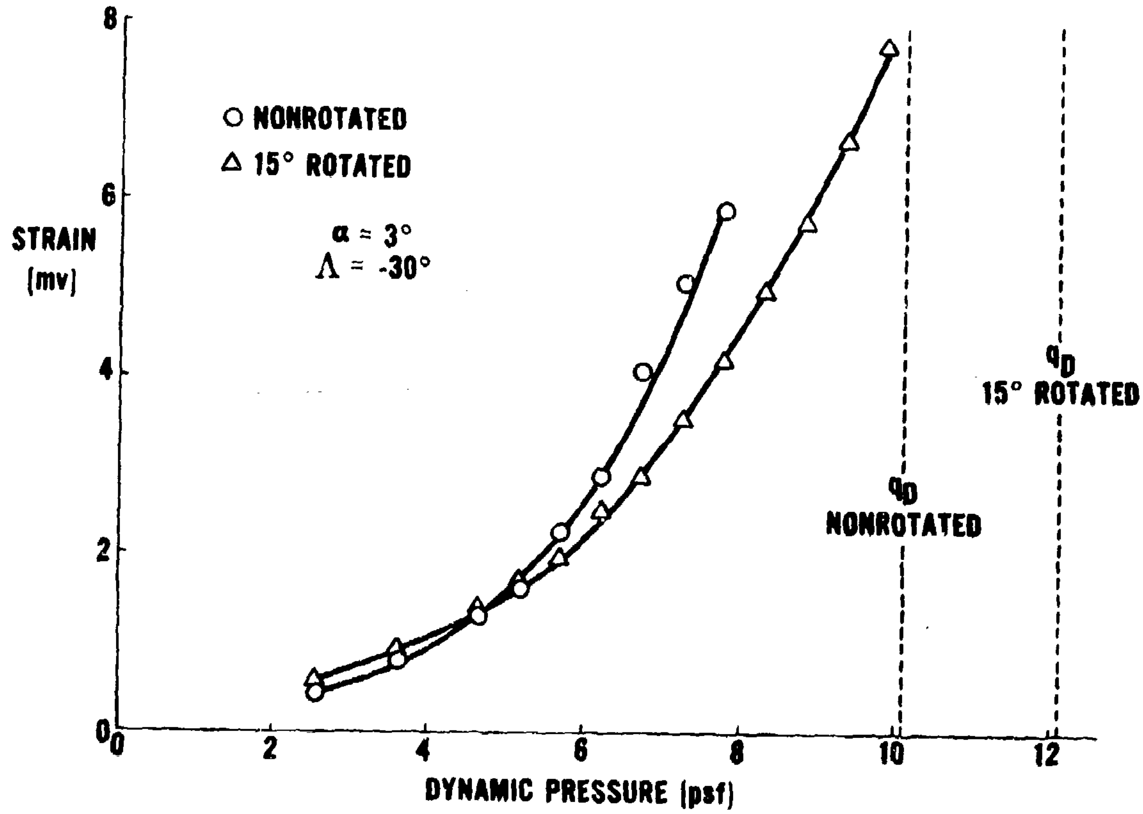

Figure 32. Comparison of Strain Levels for Two Composite Models.

3. POST TUNNEL TESTING AND ANALYSIS

As indicated in the previous section, a comparison of the test results with analytical results shows some inconsistencies. Eliminating the unswept results from this discussion due to the unreliable projections because of flutter, and the -60° sweep positions due to the question of the analytical aerodynamics at this high sweep, the following discussion will concentrate on the three interim sweep positions (-15°, -30° and -45°).

Comparing the analytical results with the hard divergence points, the aluminum and the 7.5° rotated models differ by less than 5%. However, analysis of the nonrotated model predicted unconservative divergence dynamic pressures; in the case of the 15° forward sweep, the analysis predicted a 24% higher divergence dynamic pressure than was measured. For the 15° rotated model, the analytical results are conservative; divergence at 15° forward sweep was undefinable.

During manufacturing of the sleeve, the channels were mounted on the aluminum plate which was used as part of the mold. When the sleeve was attached to the aluminum plate, the model was in an unstressed state. However, the composite plates are thinner, requiring the sleeve channels and dowels to compress the foam when bolted to the plate. The resulting tension in the bolts caused stress to be applied to the composite plates. This stress has the general effect of stiffening the model, particularly in torsion, and increasing the torsional frequencies.

Prior to the wind tunnel testing, the sleeve never experienced a high load condition. During wind tunnel testing, some model configurations were loaded so the deflection was approximately a foot at the tip. While testing the aluminum model to find the "hard" divergence points, the model experienced higher deflections and, in some cases, severe high amplitude oscillations. The result of the high deflection was to loosen the bond in the sleeve between the channels and the foam. In order to provide a better correlation between the analyses and test, the ground vibration tests were repeated and the analytical models were redefined.

Table 23 compares the results from the ground vibration tests. The greatest change is the reduction in the first torsional frequency. Since the mass of the model remains unchanged, the model torsional stiffness must have been lowered. Although not shown, the plate frequencies were unchanged. Therefore, the reduction in model torsional stiffness is due to the reduction in stiffness due to the sleeve.

Input to NASTRAN and TSO analyses were modified to account for changes in the composite models. The stiffness of the finite element beams in TSO and the constrained plate elements in NASTRAN was reduced until the analytical model frequencies matched the frequencies measured during the ground vibration test conducted after the wind tunnel test. The results of the revised analyses are shown in Table 22. As expected, the nonrotated post test analyses showed an overall reduction in the divergence speeds. The revised analyses predict divergence dynamic pressures less than 8% above the test values. For the 7.5° rotated model, the analytical results changed very little (<1%). For the 15° rotated model, the revised analyses predicted divergence dynamic pressures that are within 4% of the test results.

TABLE 23

COMPARISON OF MODEL NATURAL FREQUENCIES
MEASURED BEFORE AND AFTER THE WIND TUNNEL TEST

Mode	Aluminum (1)	Aluminum (2)	Graphite-epoxy Nonrotated (1)	Nonrotated (2)	7.5° Rotated (1)	7.5° Rotated (2)	15° Rotated (1)	15° Rotated (2)
1B	3.32	3.29	3.57	3.51	3.40	3.39	3.19	3.18
2B	16.97	16.78	17.04	17.67	16.96	16.93	15.36	15.40
1T	36.09	36.95	31.57	26.90	32.04	26.58	31.42	27.76
3B	43.48	43.61	46.53	45.68	44.36	43.48	40.70	40.20
2T	87.07	88.87	64.88	63.16	65.88	65.85	68.74	71.68
4B	81.85	81.43	86.22	84.28	83.08	81.91	75.99	76.28

Units: Hz

(1) GVT performed before wind tunnel test.
(2) GVT performed after wind tunnel test.

Although the overall comparison has been improved by matching the analysis to the post wind tunnel testing, the increase of divergence dynamic pressure for the 15° rotated model was not expected since the model torsional stiffness had decreased. A possible explanation for the increase in divergence dynamic pressure is, as the plies are rotated forward, the coupling between the sleeve and plate increases. For the 15° rotated model, the coupling caused by the sleeve must have been detrimental, that is, the coupling caused a reduction in the divergence dynamic pressure. Therefore, a reduction in the sleeve stiffness would cause an increase in the divergence dynamic pressures. For the nonrotated model, the sleeve channels are nearly perpendicular to the primary bending plies and provide minimal coupling between bending and torsion. Therefore, a reduction in the torsional stiffness component would result in a reduction of the divergence dynamic pressure. This is especially evident at low forward sweeps where torsional stiffness has the greatest effect.

SECTION VI

CONCLUSIONS

Results of analyses, laboratory tests, and wind tunnel tests of a rather simple, variable sweep model that could be swept forward 15°, 30°, 45° and 60° from the leading edge unswept position, and could also accommodate structural plates of aluminum and graphite-epoxy materials, have illustrated the principle involved in the structural design technology of aeroelastic tailoring. Several conclusions can be drawn from this research which are briefly discussed below.

The high stiffness to weight ratio of the graphite-epoxy is more efficient than aluminum in providing the stiffness required to increase the divergence dynamic pressure. The ability to tailor the composite material for bend-twist coupling significantly adds to the efficiency from a weight standpoint.

It has been shown that simply rotating a 0°±45° composite laminate forward significantly increases the divergence dynamic pressure of a forward swept wing at leading edge sweep angles to about -20°. A smaller increase in divergence dynamic pressure occurs at -30° and -45° sweep. A reversal in the trend occurs at -60° sweep.

The analytical methods used predict the divergence dynamic pressures very well for all models at -30° and -45° sweep. For -15° sweep, the correlation between analytical and test results is very good for all models except the 15° rotated model where an unusual oscillatory phenomenon occurred in the wind tunnel. The large deflections obtained during testing apparently caused a reduction in torsional stiffness of the composite models, probably due to loosening of the aerodynamic sleeve. This effect was most noticeable at the 0° sweep angle and affected the correlation of analytical and test results. The analytical results were consistently higher than the measured values at -60° sweep, apparently associated with turbulence from the fairing cavity.

The divergence dynamic pressures predicted by the static and dynamic (velocity-damping) analyses, using Woodward and Doublet Lattice aerodynamics, respectively, agree favorably at sweep angle of -15°, -30° and -45°. The Woodward static analysis is least accurate at -60° sweep, predicting higher dynamic pressure than measured.

While the divergence dynamic pressure is not significantly increased at -30° sweep by rotating the composite laminate 15° forward, the load level at a given angle of attack is significantly reduced at dynamic pressures greater than 60% of the divergence dynamic pressure.

The subcritical projection methods described herein accurately predict divergence dynamic pressure at 80% and less of the divergence dynamic pressure. It may be possible to use methods like these in flight testing for divergence.

The severity of the motion of the wing at divergence onset increases with forward sweep.

APPENDIX A

MODE SHAPES

Three sets of mode shapes are presented in the following pages. Figures A-1 through A-4 are the experimentally measured mode shapes. Figures A-5 through A-8 are the mode shapes resulting from the TSO analysis of each model. Figures A-9 through A-12 are the mode shapes resulting from the NASTRAN analysis of each model.

a. First Bending

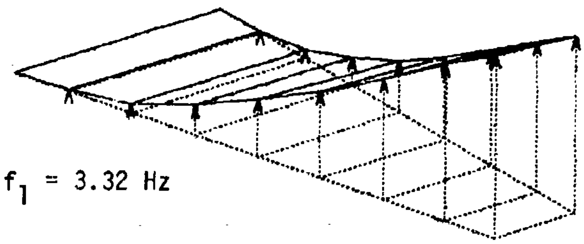

b. Second Bending

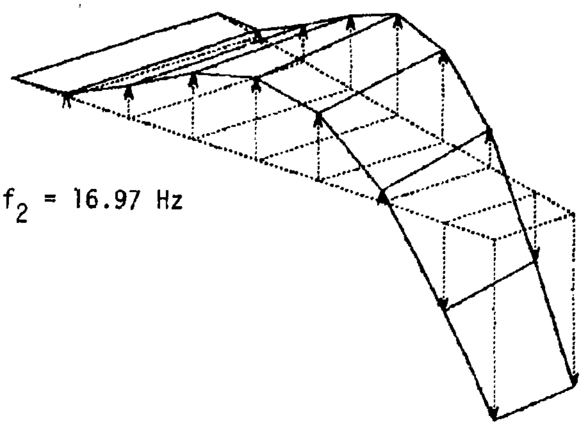

c. First Torsion

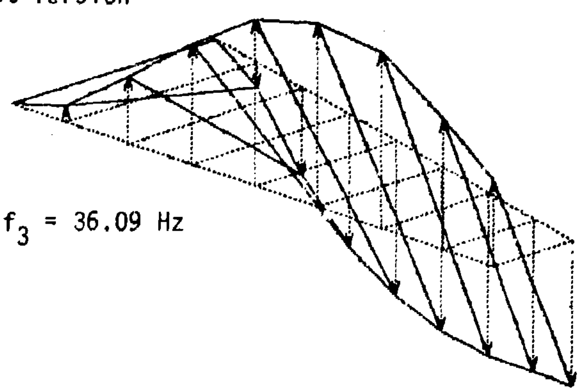

Figure A-1. Measured mode shapes for the aluminum model.

a. First Bending

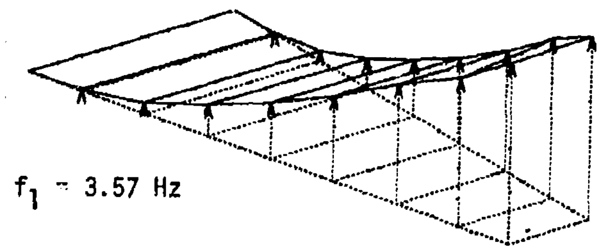

b. Second Bending

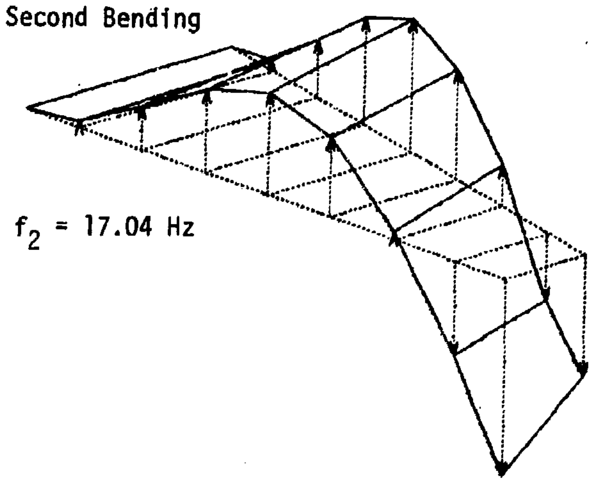

c. First Torsion

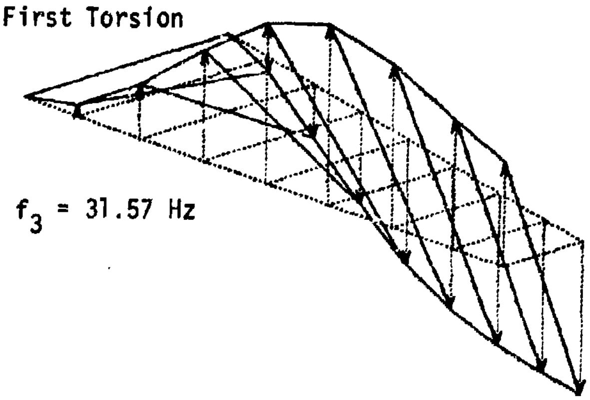

Figure A-2. Measured mode shapes for the nonrotated model.

a. First Bending

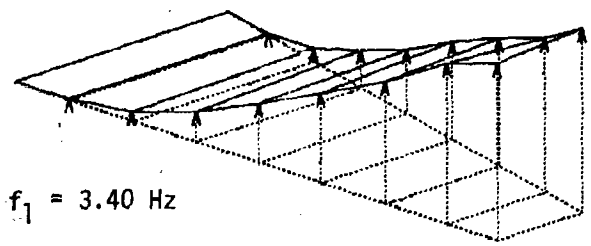

b. Second Bending

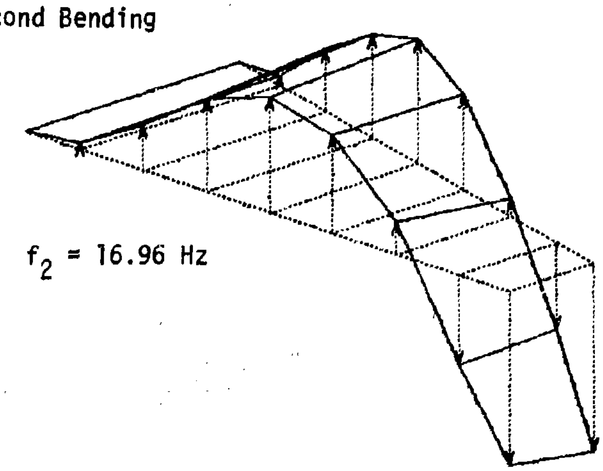

c. First Torsion

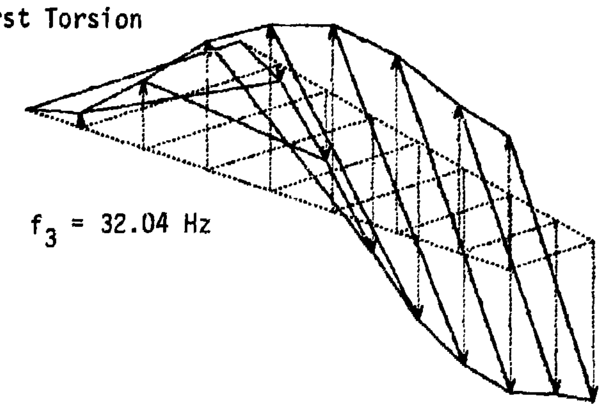

Figure A-3. Measured mode shapes for the 7.5° rotated model.

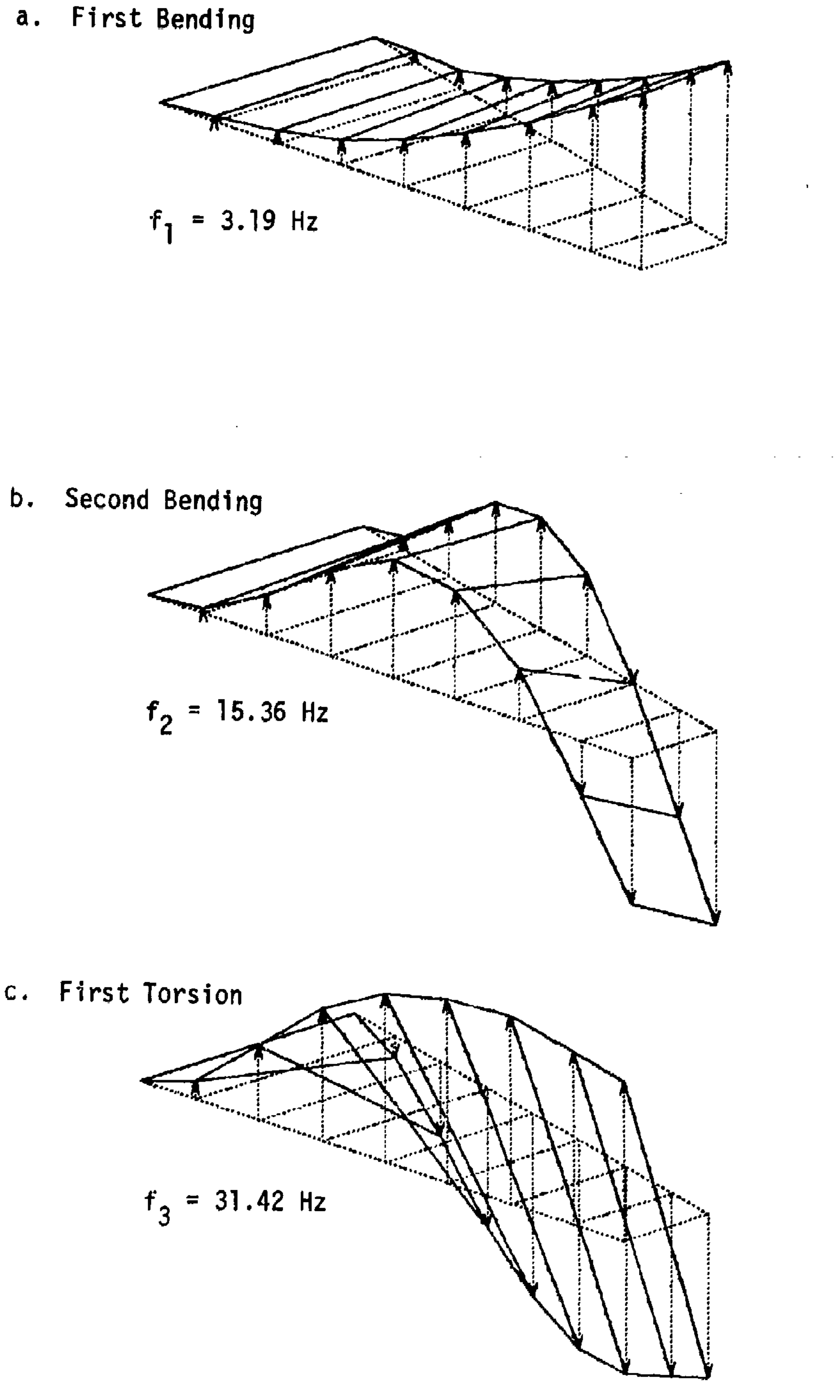

Figure A-4. Measured mode shapes for the 15° rotated model.

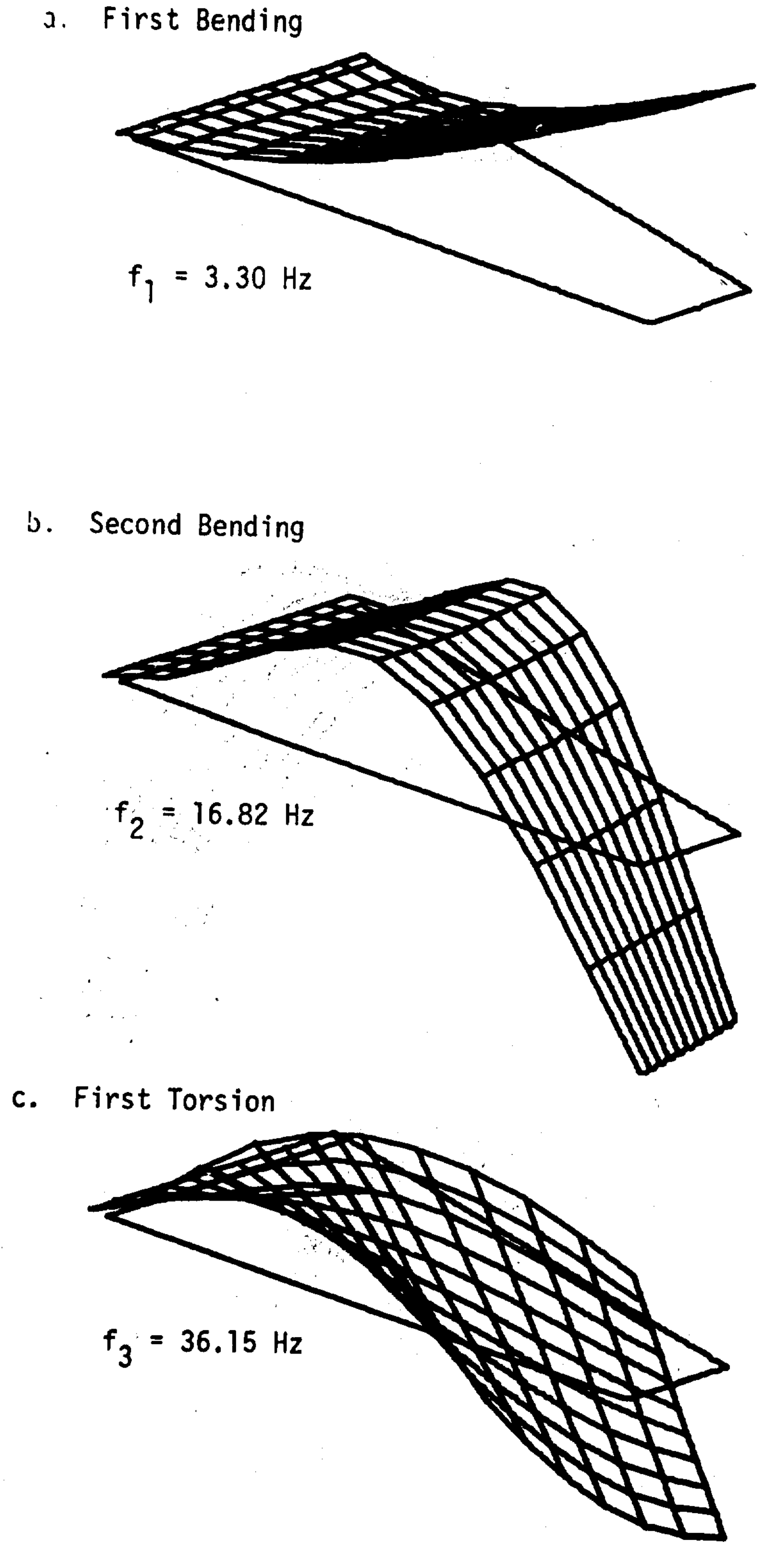

Figure A-5. TSO analysis mode shapes for the aluminum model.

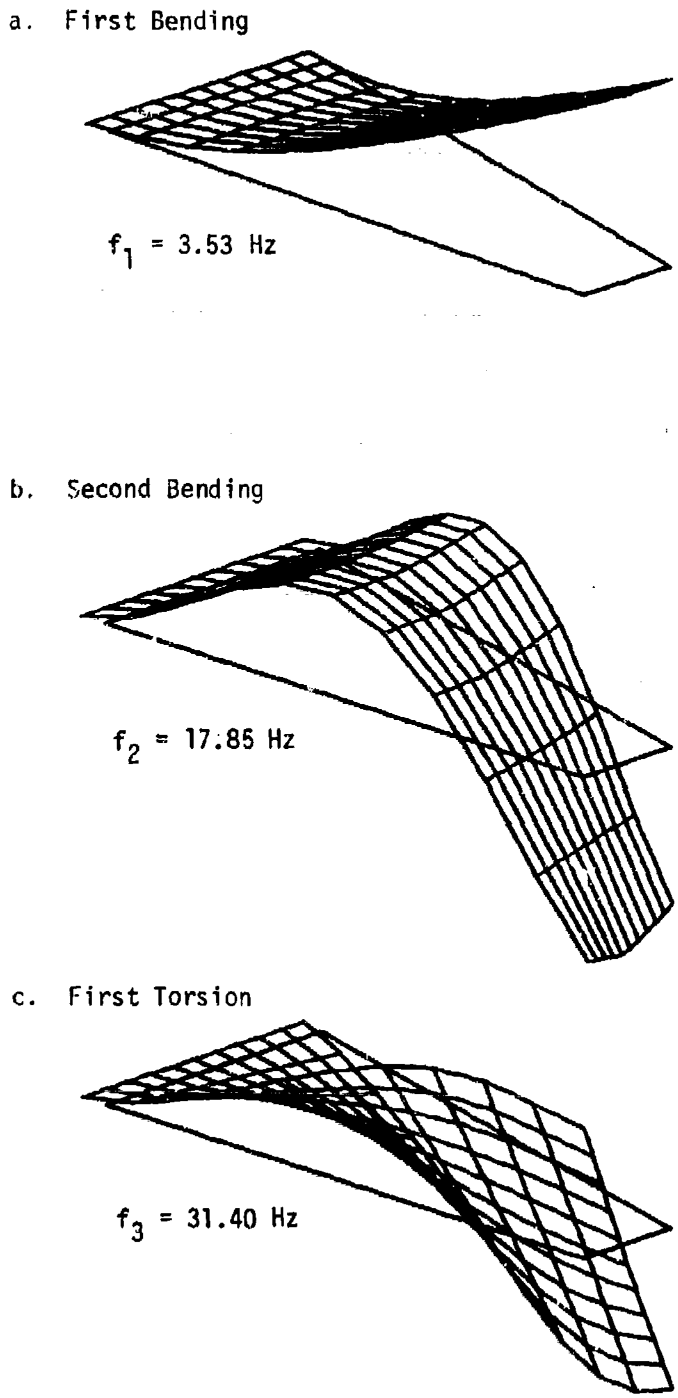

Figure A-6. TSO analysis mode shapes for the nonrotated model.

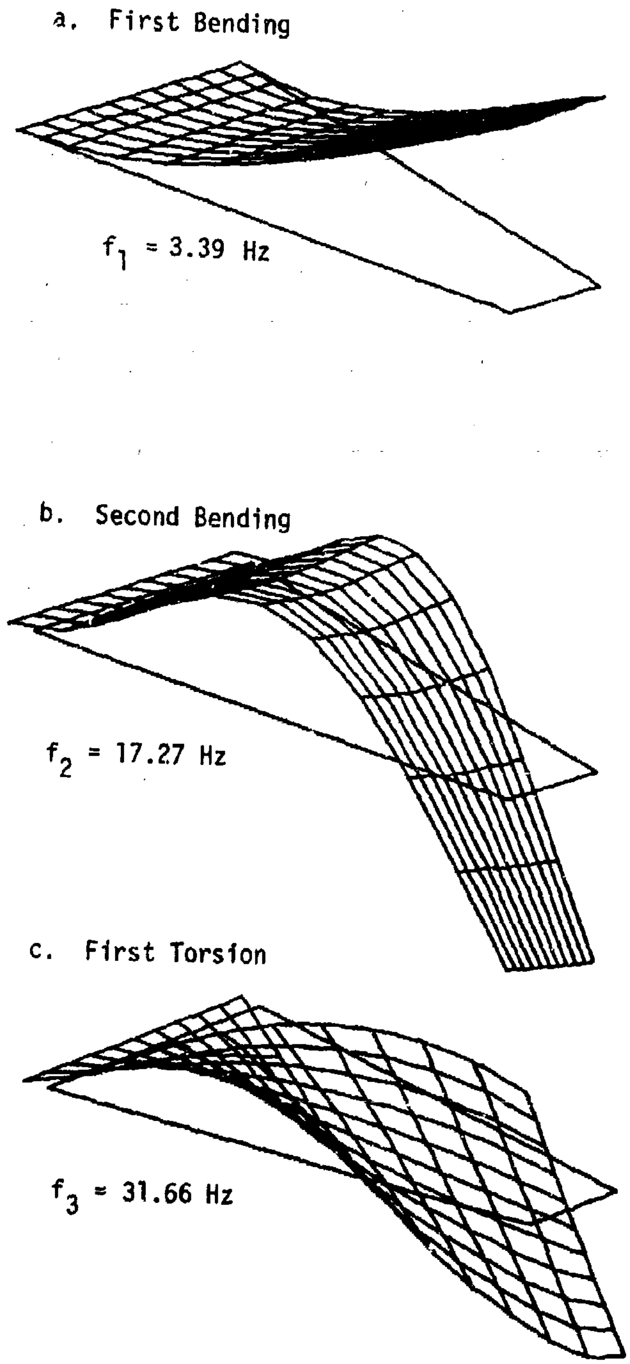

Figure A-7. TSO analysis mode shapes for the 7.5° rotated model.

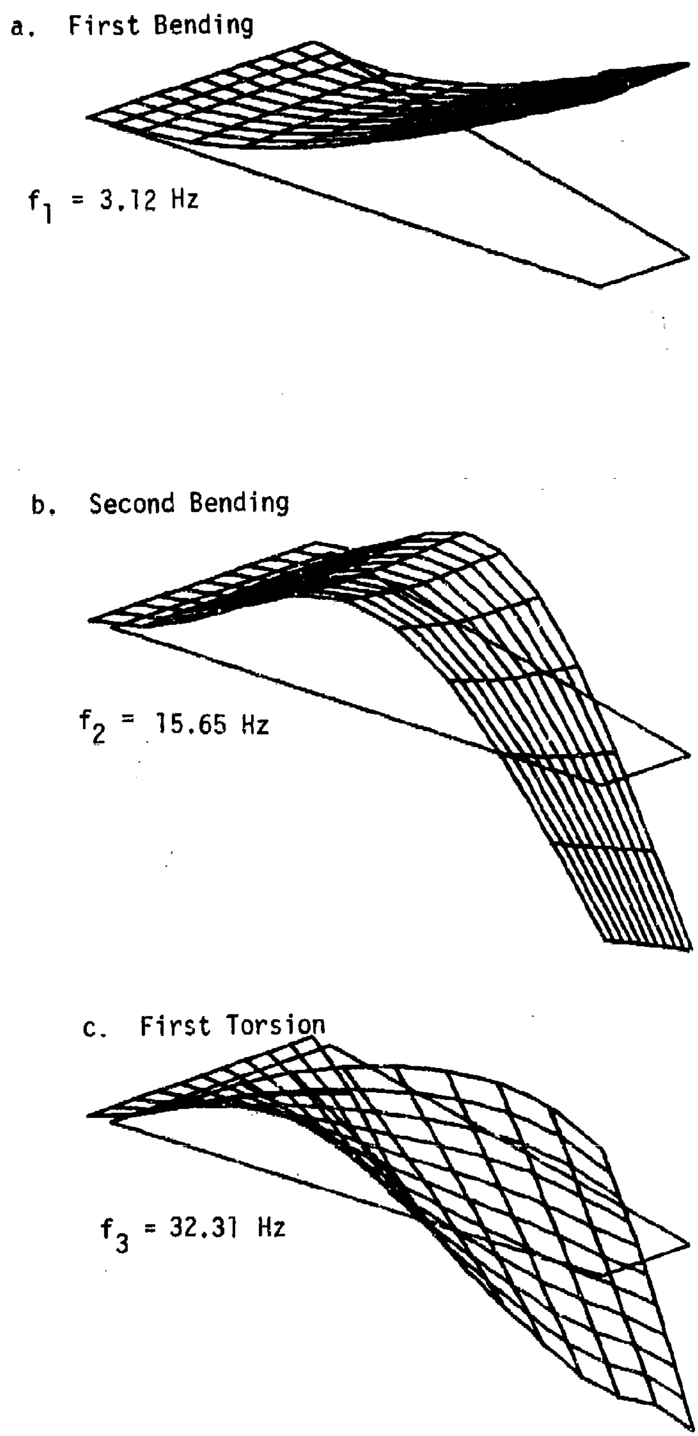

Figure A-8. TSO analysis mode shapes for the 15° rotated model.

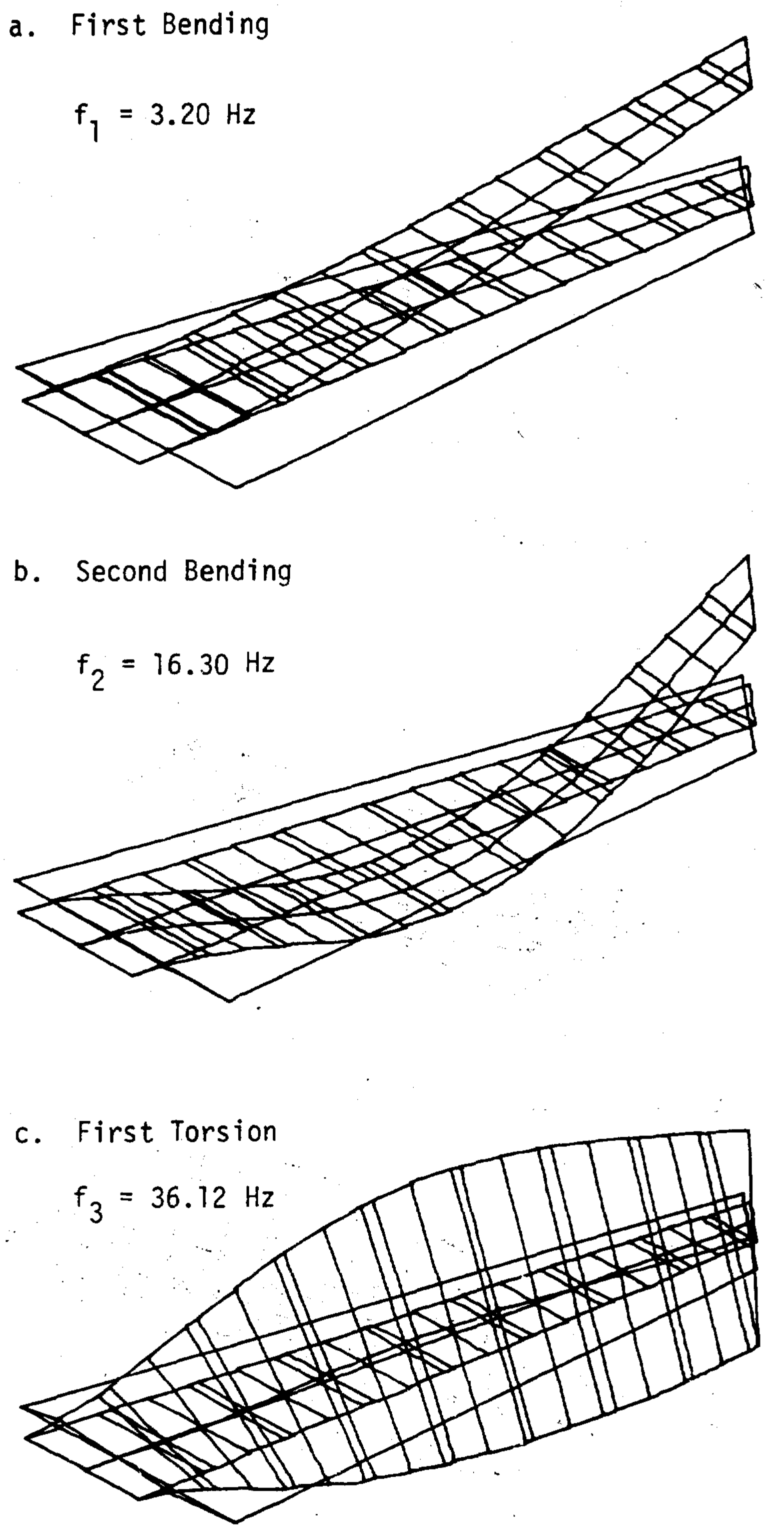

Figure A-9. NASTRAN analysis mode shapes for the aluminum model.

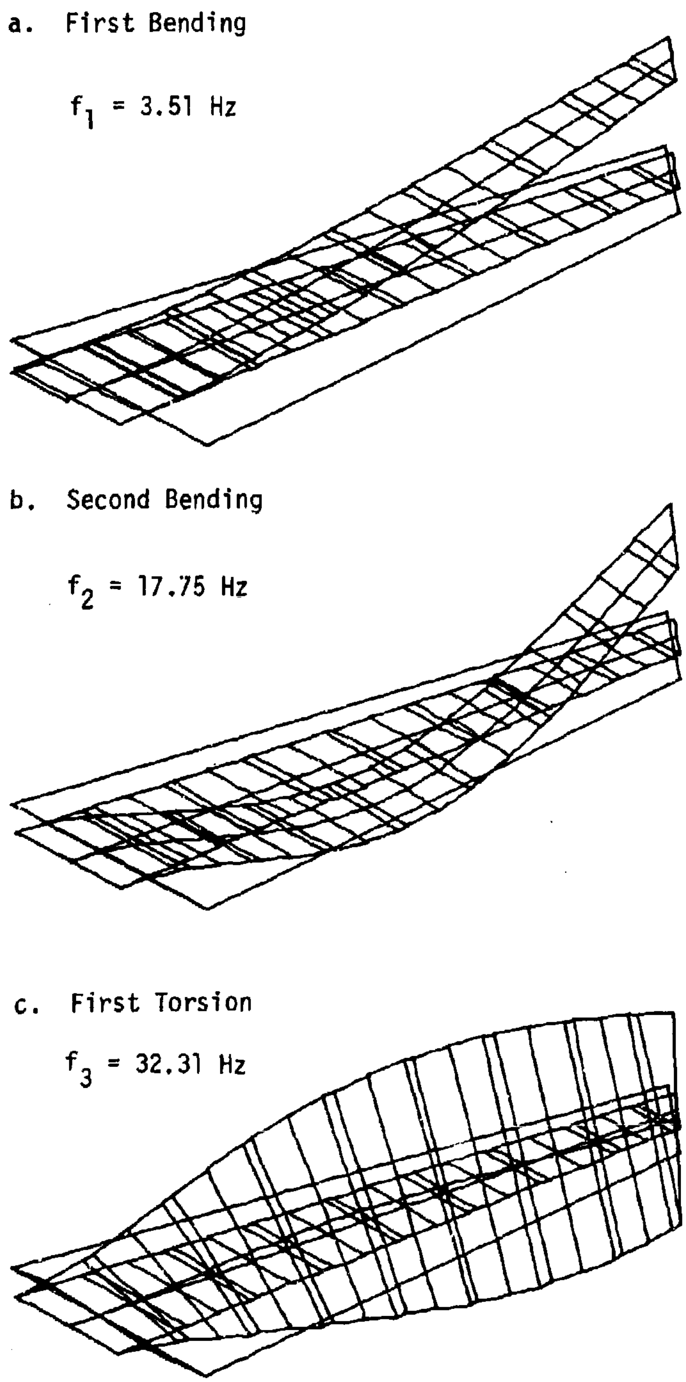

Figure A-10. NASTRAN analysis mode shapes for the nonrotated model.

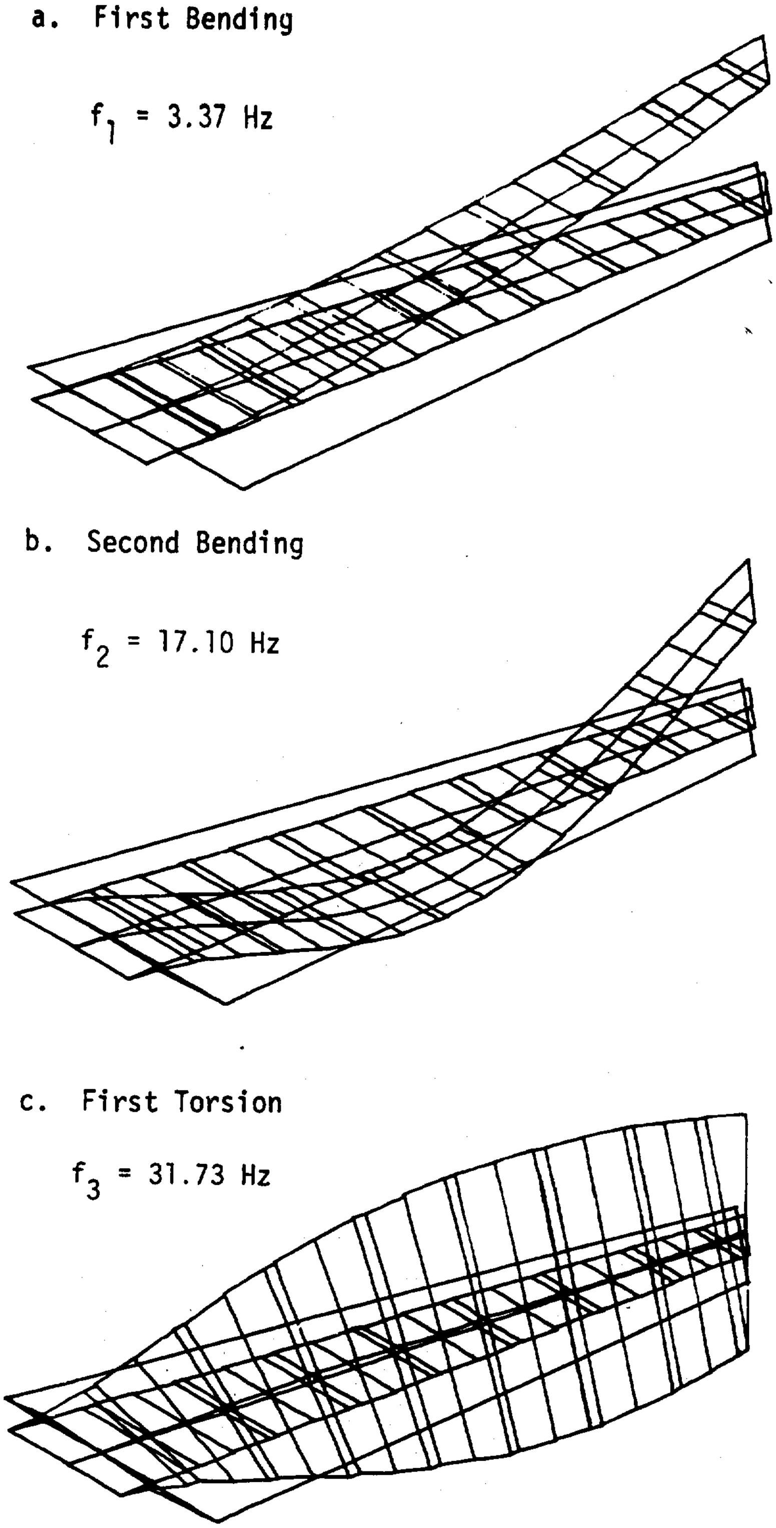

Figure A-11. NASTRAN analysis mode shapes for the 7.5° rotated model.

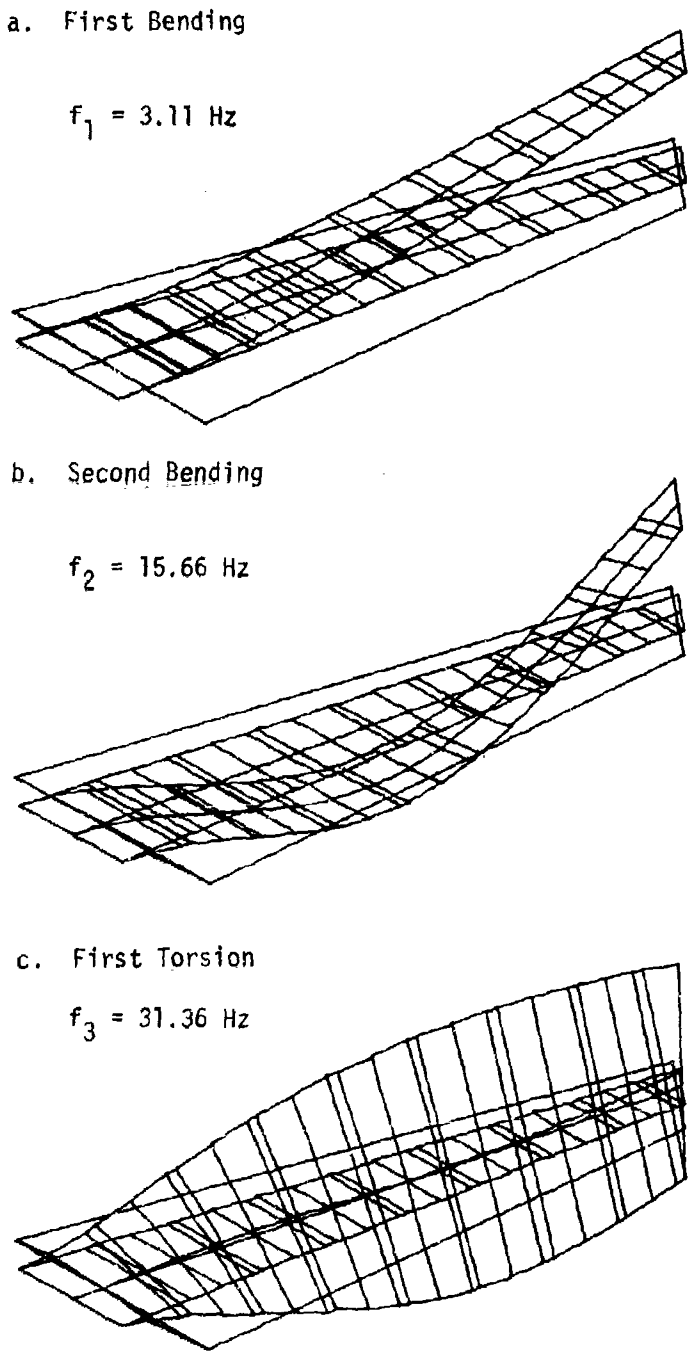

Figure A-12. NASTRAN analysis mode shapes for the 15° rotated model.

APPENDIX B

STACKING SEQUENCE ANALYSIS

The tables presented in this Appendix represent some of the qualitative analyses performed with the CWING computer procedure. The aerodynamics were calculated for the airfoil planform. The divergence dynamic pressures were calculated for the aluminum plate and eight graphite-epoxy plates. Each graphite-epoxy plate had plies of 0° and ±45° in varying percentages ranging from all 0° to all ±45°.

ALUMINUM

DIVERGENCE DYNAMIC PRESSURES (PSF) FOR FORWARD SWEEP ANGLES (DEGS)				
0	15	30	45	60
25.07	12.73	10.89	13.06	25.89

FSW GRAPHITE PLATE
((0)8)S

PLY ANGLES (DEGS)	DIVERGENCE DYNAMIC PRESSURES (PSF) FOR FORWARD SWEEP ANGLES (DEGS)				
	0	15	30	45	60
-5,+45,-45	2.93	2.90	3.43	5.08	10.94
0,+45,-45	6.20	5.44	5.88	8.05	16.26
5,+45,-45	******	25.38	13.85	13.84	23.79
10,+45,-45	******	******	399.59	22.99	29.44
15,+45,-45	******	******	******	25.90	26.79
20,+45,-45	******	******	******	17.68	19.49
25,+45,-45	******	******	******	10.55	13.43

FSW GRAPHITE PLATE
((-45,+45)4)S

PLY ANGLES (DEGS)	DIVERGENCE DYNAMIC PRESSURES (PSF) FOR FORWARD SWEEP ANGLES (DEGS)				
	0	15	30	45	60
-5,+40,-50	10.39	4.68	3.88	4.59	9.09
0,+45,-45	7.24	4.01	3.54	4.31	8.66
5,+50,-40	5.51	3.51	3.25	4.08	8.29
10,+55,-35	4.40	3.10	3.01	3.87	7.98
15,+60,-30	3.64	2.78	2.81	3.70	7.71
20,+65,-25	3.10	2.53	2.64	3.57	7.51
25,+70,-20	2.72	2.34	2.53	3.50	7.43

FSW GRAPHITE PLATE
((0)4 / (-45,+45)2)S

PLY ANGLES (DEGS)	DIVERGENCE DYNAMIC PRESSURES (PSF) FOR FORWARD SWEEP ANGLES (DEGS)				
	0	15	30	45	60
-5,+45,-45	4.39	4.03	4.54	6.44	13.66
0,+45,-45	8.27	6.64	6.82	9.06	18.36
5,+45,-45	45.43	14.67	11.17	12.59	23.49
10,+45,-45	******	314.94	19.67	15.93	26.61
15,+45,-45	******	******	32.80	16.69	25.56
20,+45,-45	******	******	35.17	14.35	21.49
25,+45,-45	******	******	24.46	11.03	16.94
-5,+40,-50	4.53	4.14	4.64	6.57	13.90
0,+45,-45	8.27	6.64	6.82	9.06	18.36
5,+50,-40	35.03	13.66	10.79	12.36	23.22
10,+55,-35	******	91.40	18.24	15.64	26.51
15,+60,-30	******	******	30.59	16.97	26.27
20,+65,-25	******	******	39.04	15.39	22.95
25,+70,-20	******	******	30.86	12.37	18.64

FSW GRAPHITE PLATE
((-45,+45)2 / (0)4)S

FSW GRAPHITE PLATE

PLY ANGLES (DEGS)	DIVERGENCE DYNAMIC PRESSURES (PSF) FOR FORWARD SWEEP ANGLES (DEGS)				
	0	15	30	45	60
-5,+45,-45	8.43	4.89	4.37	5.37	10.81
0,+45,-45	9.26	5.15	4.54	5.54	11.10
5,+45,-45	10.16	5.39	4.68	5.65	11.29
10,+45,-45	11.16	5.59	4.76	5.71	11.36
15,+45,-45	12.06	5.71	4.79	5.70	11.31
20,+45,-45	12.77	5.75	4.76	5.62	11.13
25,+45,-45	13.12	5.69	4.67	5.50	10.86
-5,+40,-50	11.59	5.67	4.81	5.74	11.41
0,+45,-45	9.26	5.15	4.54	5.54	11.10
5,+50,-40	7.68	4.72	4.32	5.37	10.87
10,+55,-35	6.58	4.39	4.15	5.25	10.71
15,+60,-30	5.82	4.14	4.02	5.18	10.65
20,+65,-25	5.32	3.98	3.97	5.19	10.72
25,+70,-20	5.07	3.94	4.00	5.31	10.07

FSW GRAPHITE PLATE
((-45,+45)3 / (0)2)S

PLY ANGLES (DEGS)	DIVERGENCE DYNAMIC PRESSURES (PSF) FOR FORWARD SWEEP ANGLES (DEGS) 0	15	30	45	60
-5,+45,-45	7.50	4.16	3.66	4.46	8.97
0,+45,-45	7.59	4.18	3.68	4.49	9.00
5,+45,-45	7.67	4.21	3.69	4.49	9.02
10,+45,-45	7.75	4.22	3.70	4.50	9.03
15,+45,-45	7.80	4.23	3.70	4.50	9.02
20,+45,-45	7.84	4.24	3.70	4.49	9.01
25,+45,-45	7.85	4.23	3.69	4.48	8.98
-5,+40,-50	10.77	4.85	4.02	4.76	9.42
0,+45,-45	7.59	4.18	3.68	4.48	9.00
5,+50,-40	5.82	3.67	3.40	4.25	8.64
10,+55,-35	4.68	3.27	3.16	4.06	8.34
15,+60,-30	3.90	2.95	2.96	3.90	8.10
20,+65,-25	3.35	2.69	2.81	3.78	7.94
25,+70,-20	2.97	2.53	2.71	3.73	7.91

FSW GRAPHITE PLATE
((0)6 / (-45,+45)1)S

PLY ANGLES (DEGS)	DIVERGENCE DYNAMIC PRESSURES (PSF) FOR FORWARD SWEEP ANGLES (DEGS) 0	15	30	45	60
-5,+45,-45	3.09	3.03	3.57	5.26	11.30
0,+45,-45	6.42	5.59	6.00	8.29	16.60
5,+45,-45	******	21.42	13.11	13.56	23.79
10,+45,-45	******	******	75.75	21.12	29.01
15,+45,-45	******	******	******	23.37	26.83
20,+45,-45	******	******	******	17.05	20.18
25,+45,-45	******	******	******	10.31	14.30
-5,+40,-50	3.10	3.04	3.58	5.27	11.32
0,+45,-45	6.42	5.59	6.00	8.20	16.60
5,+50,-40	******	21.00	13.01	13.52	23.75
10,+55,-35	******	******	71.92	21.05	29.02
15,+60,-30	******	******	******	23.54	27.03
20,+65,-25	******	******	******	17.39	20.47
25,+70,-20	******	******	******	11.09	14.56

FSW GRAPHITE PLATE
((0)2 / (-45,+45)3)S

PLY ANGLES (DEGS)	DIVERGENCE DYNAMIC PRESSURES (PSF) FOR FORWARD SWEEP ANGLES (DEGS) 0	15	30	45	60
-5,+45,-45	7.07	5.47	5.55	7.33	15.13
0,+45,-45	10.60	7.21	6.84	8.68	17.53
5,+45,-45	19.64	9.82	8.33	9.94	19.49
10,+45,-45	76.82	13.66	9.75	10.77	20.46
15,+45,-45	******	18.71	10.63	10.89	20.15
20,+45,-45	******	23.36	10.63	10.30	18.74
25,+45,-45	******	24.31	9.84	9.25	16.74
-5,+40,-50	7.95	5.94	5.90	7.70	15.78
0,+45,-45	10.60	7.21	6.84	8.68	17.74
5,+50,-40	15.30	8.83	7.86	9.60	19.04
10,+55,-35	25.92	10.95	8.89	10.37	20.13
15,+60,-30	72.65	13.71	9.83	10.88	20.67
20,+65,-25	******	17.32	10.58	11.06	20.58
25,+70,-20	******	21.97	11.00	10.88	19.88

FSW GRAPHITE PLATE
((-45,+45)1 / (0)6)S

PLY ANGLES (DEGS)	DIVERGENCE DYNAMIC PRESSURES (PSF) FOR FORWARD SWEEP ANGLES (DEGS) 0	15	30	45	60
-5,+45,-45	8.66	5.93	5.66	7.21	14.67
0,+45,-45	11.87	7.17	6.49	8.02	16.08
5,+45,-45	18.19	8.71	7.32	8.69	17.11
10,+45,-45	34.50	10.46	7.98	9.07	17.52
15,+45,-45	133.79	12.12	8.31	9.04	17.23
20,+45,-45	******	13.14	8.22	8.68	15.34
25,+45,-45	******	13.10	7.75	8.04	15.06
-5,+40,-50	10.44	6.53	6.13	7.66	15.43
0,+45,-45	11.07	7.17	6.49	8.32	16.08
5,+50,-40	13.56	7.71	6.83	8.33	16.61
10,+55,-35	15.78	8.28	7.14	8.60	17.32
15,+60,-30	19.09	8.93	7.45	8.81	17.31
20,+65,-25	26.02	9.72	7.75	8.98	17.47
25,+70,-20	39.46	10.76	8.07	9.09	17.47

APPENDIX C

V-g AND V-ω CURVES

Two sets of V-g and V-ω curves are presented in the following pages. Each set is comprised of one V-g and one V-ω for each of the 20 wing configurations. The first set resulted from the TSO analysis and the second set resulted from the NASTRAN analysis. All the results presented in this Appendix were calculated for sea level density.

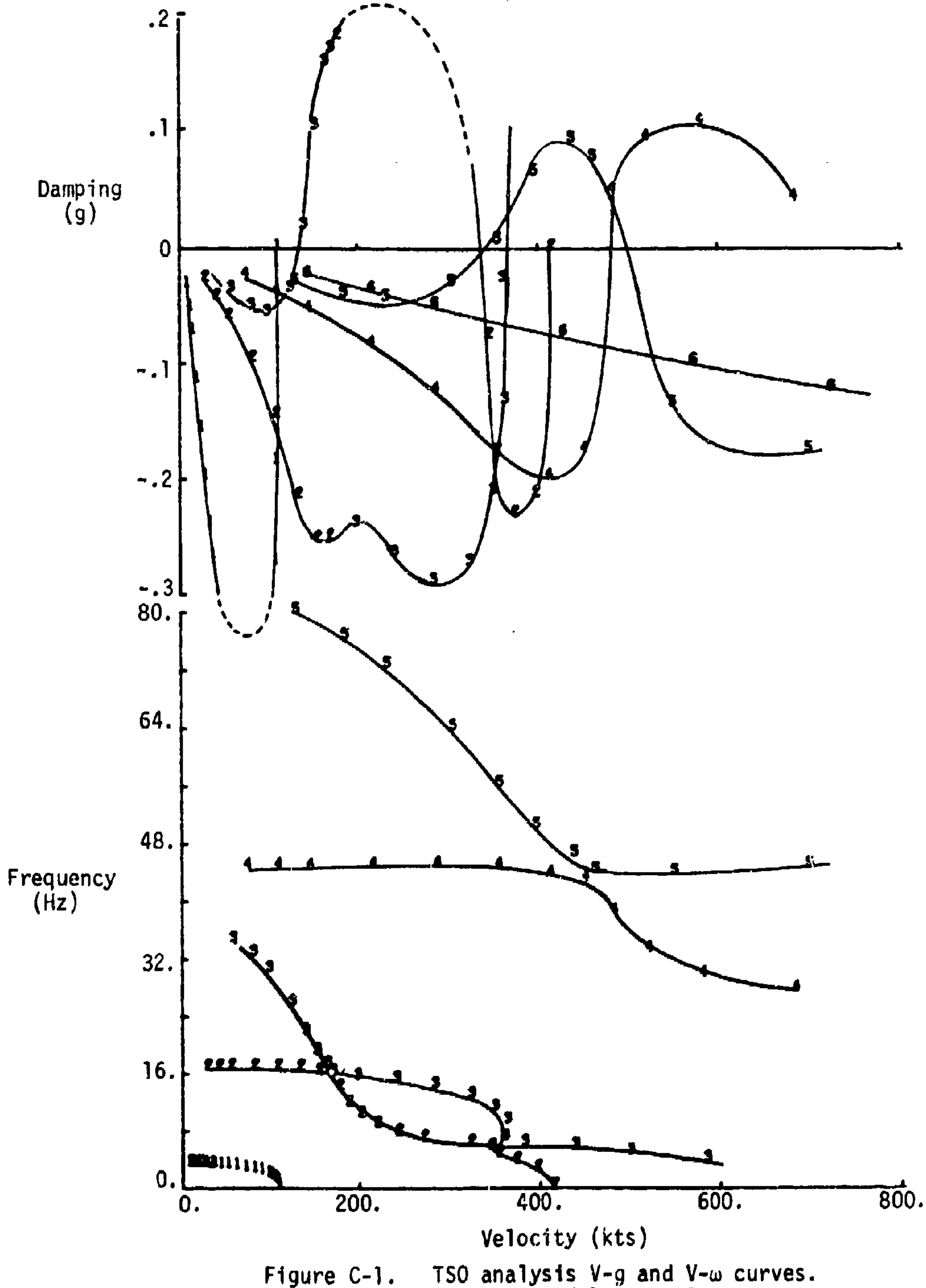

Figure C-1. TSO analysis V-g and V-ω curves.
Aluminum model, Λ = 0°.

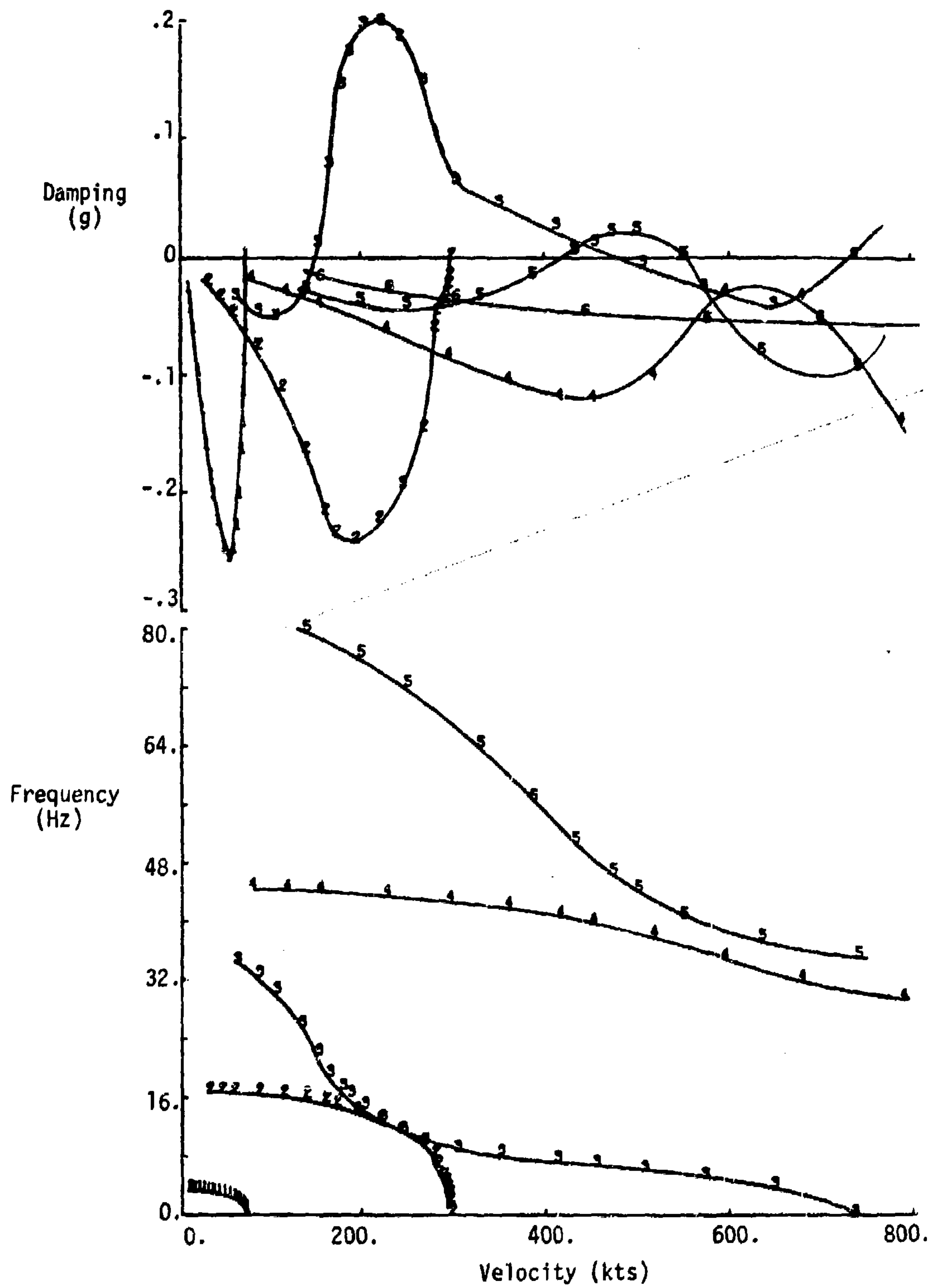

Figure C-2. TSO analysis V-g and V-ω curves. Aluminum model, Λ = -15°.

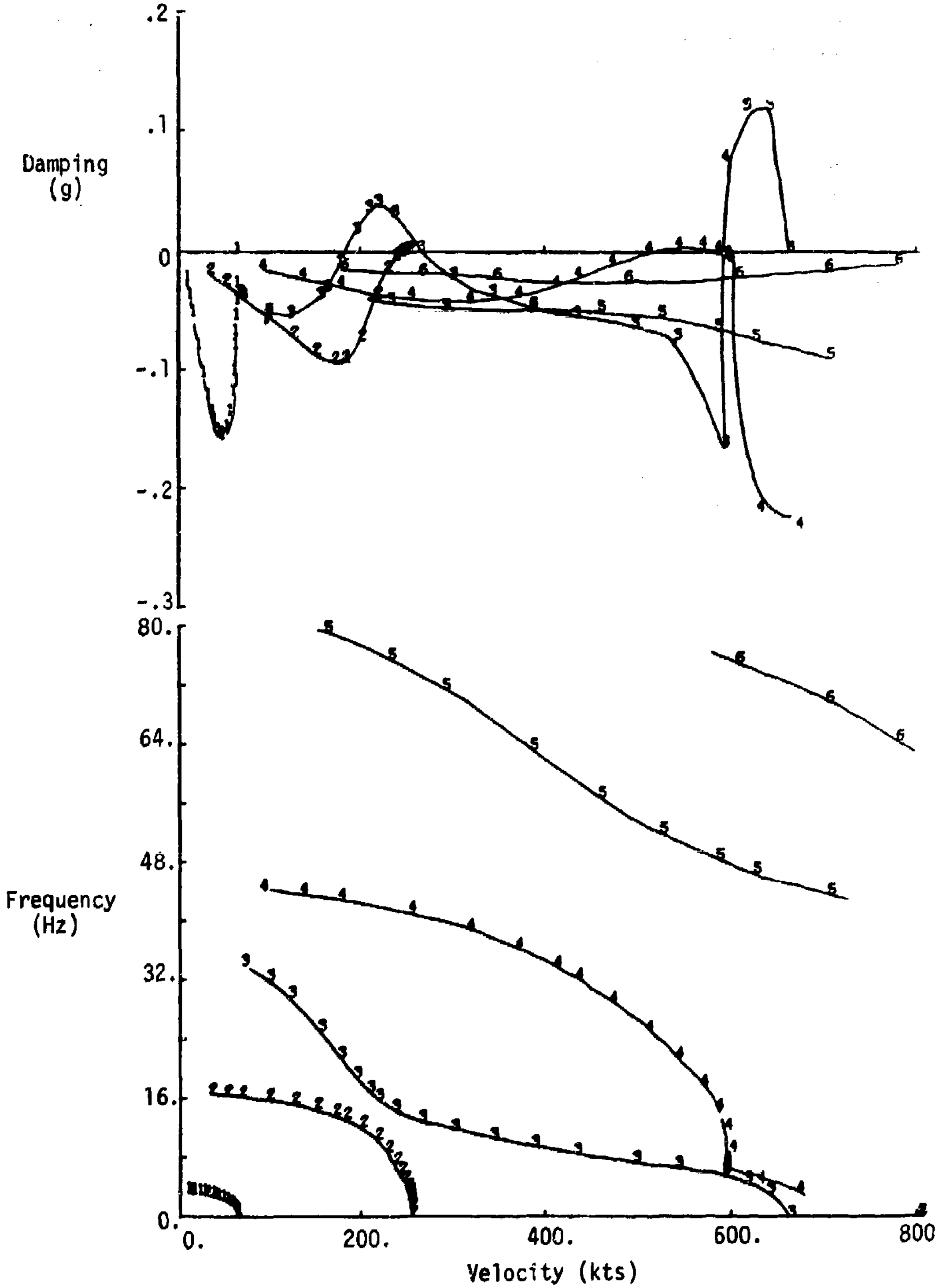

Figure C-3. TSO analysis V-g and V-ω curves.
Aluminum model, Λ = -30°.

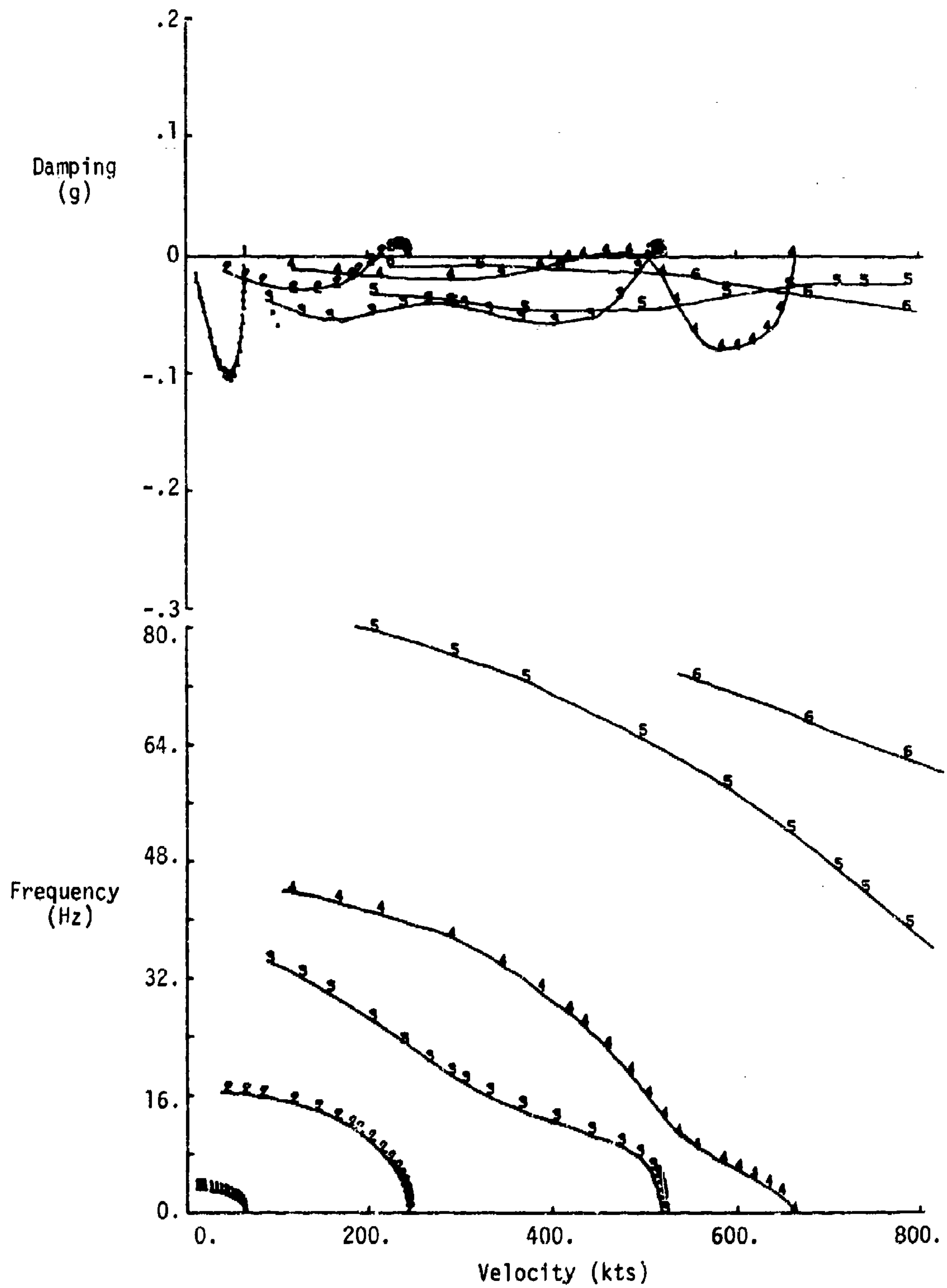

Figure C-4. TSO analysis V-g and V-ω curves.
Aluminum model, Λ = -45°.

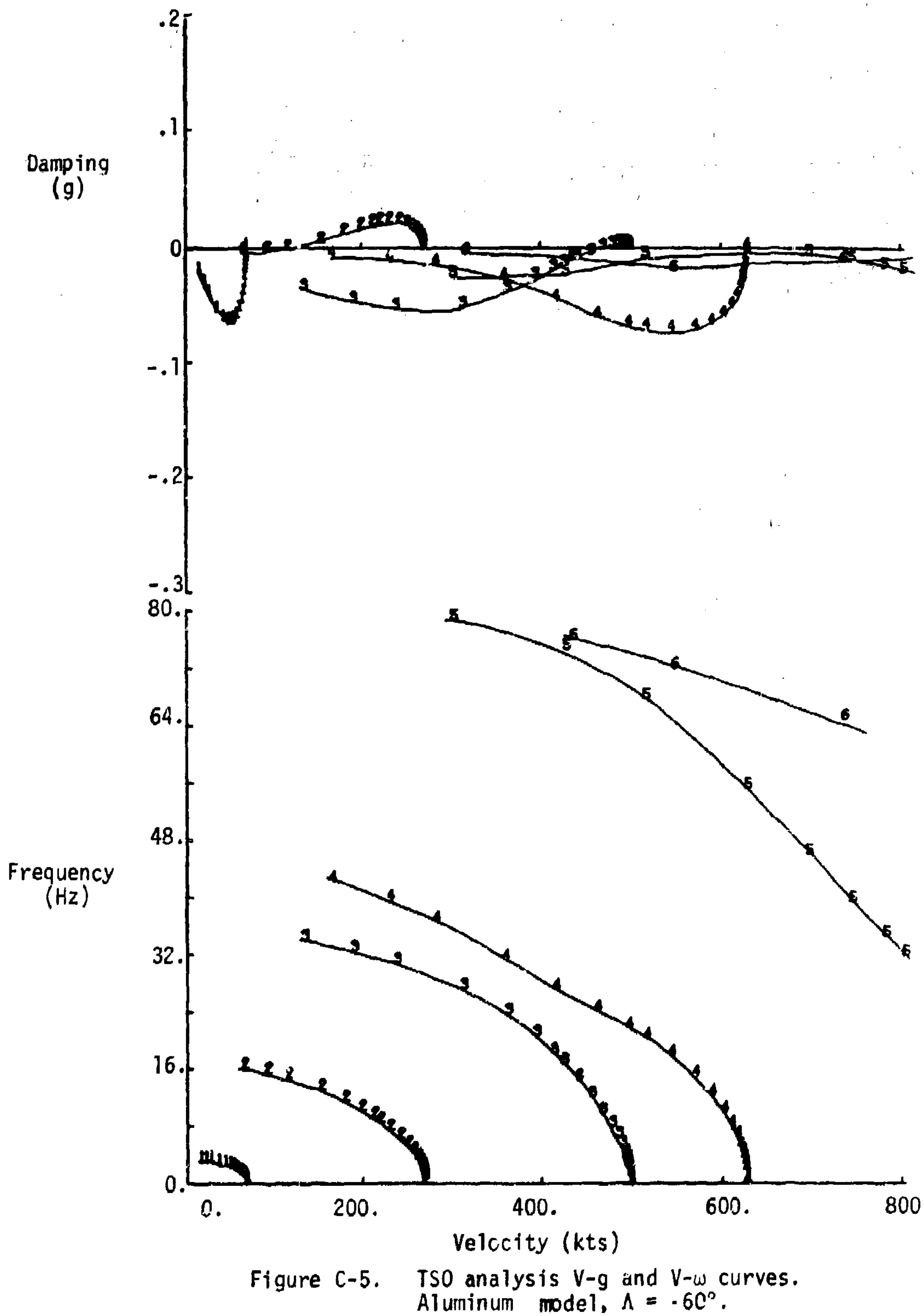

Figure C-5. TSO analysis V-g and V-ω curves.
Aluminum model, Λ = -60°.

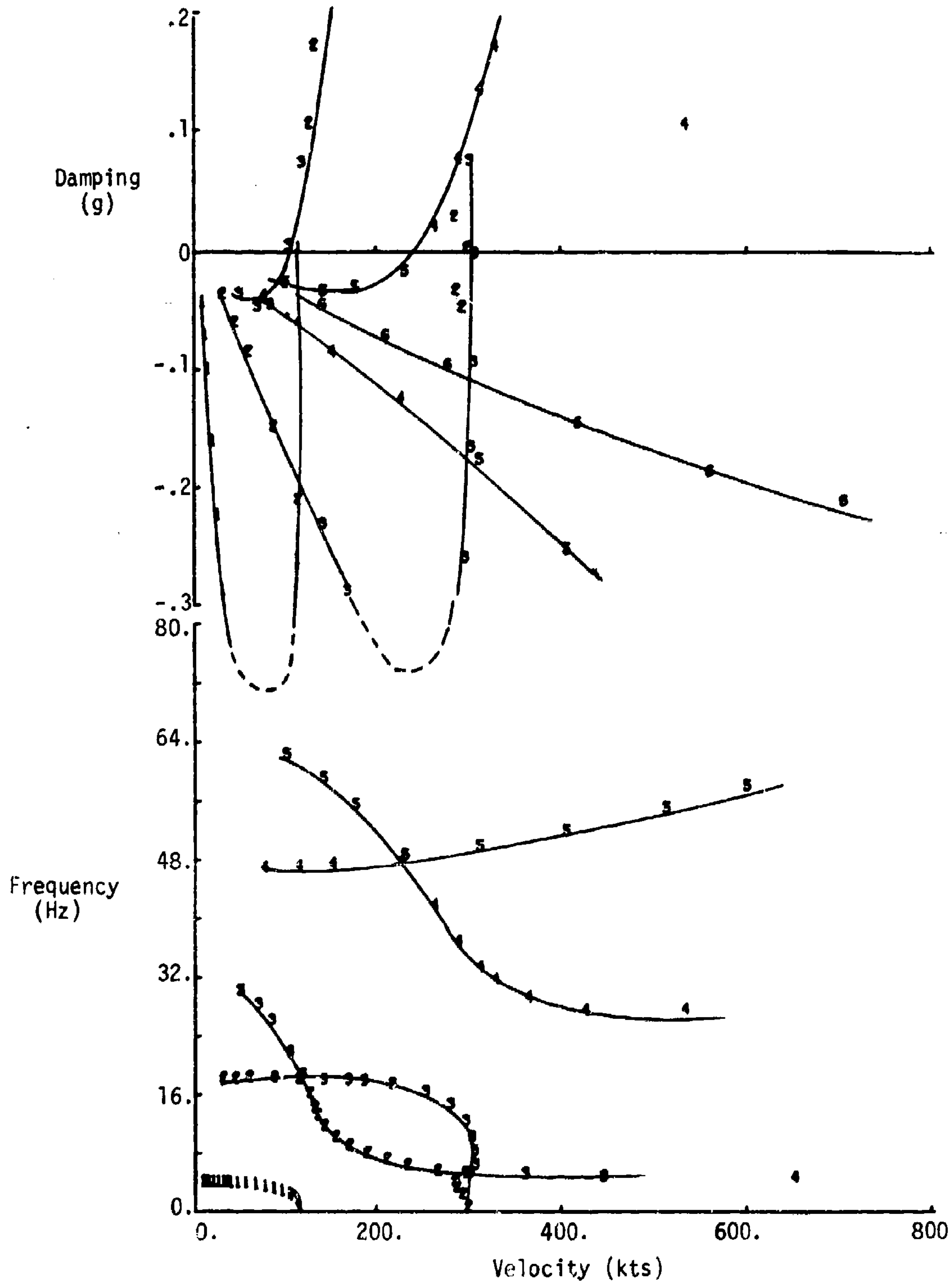

Figure C-6. TSO analysis V-g and V-ω curves. Nonrotated model, Λ = 0°.

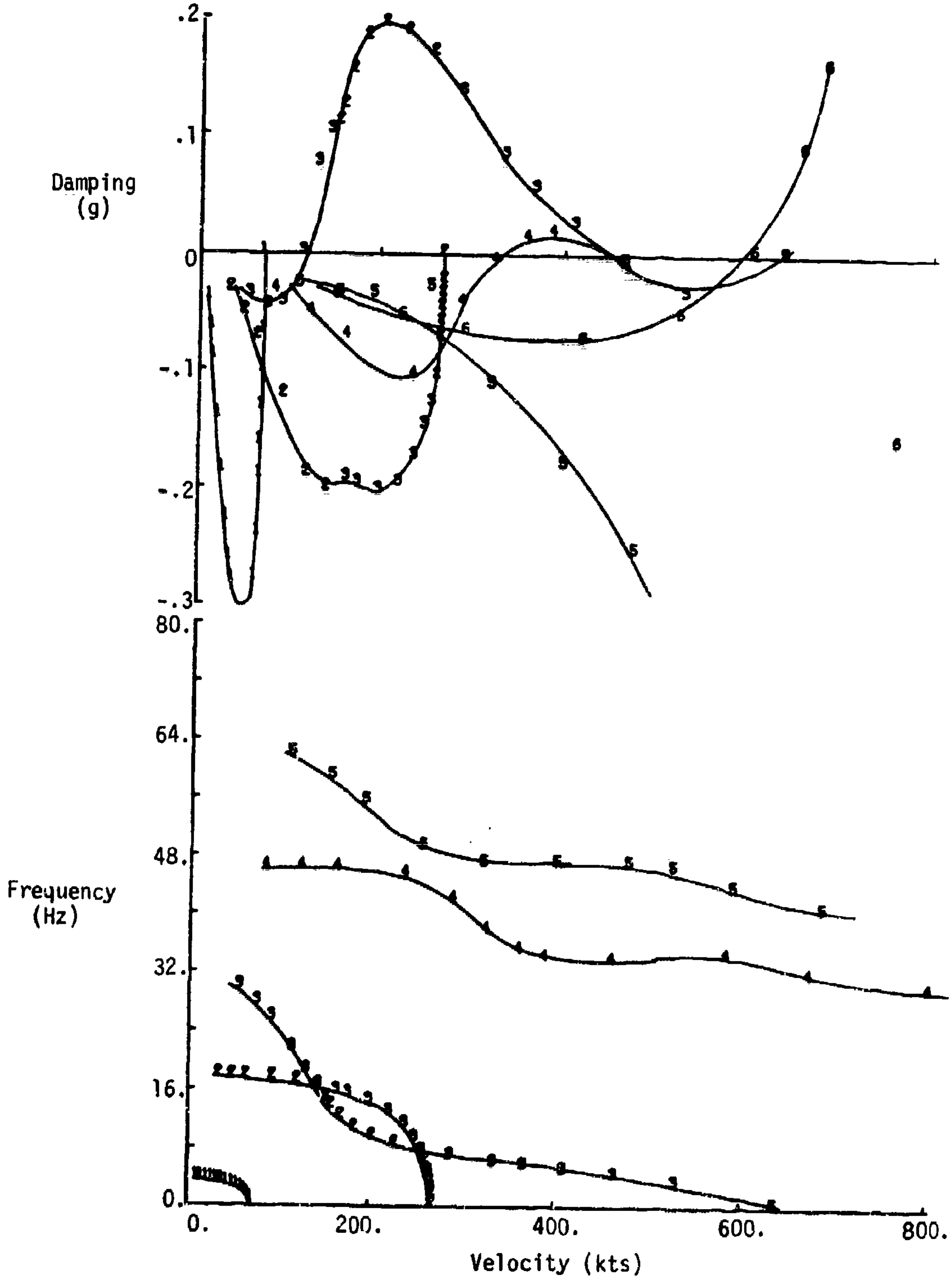

Figure C-7. TSO analysis V-g and V-ω curves. Nonrotated model, Λ = -15°.

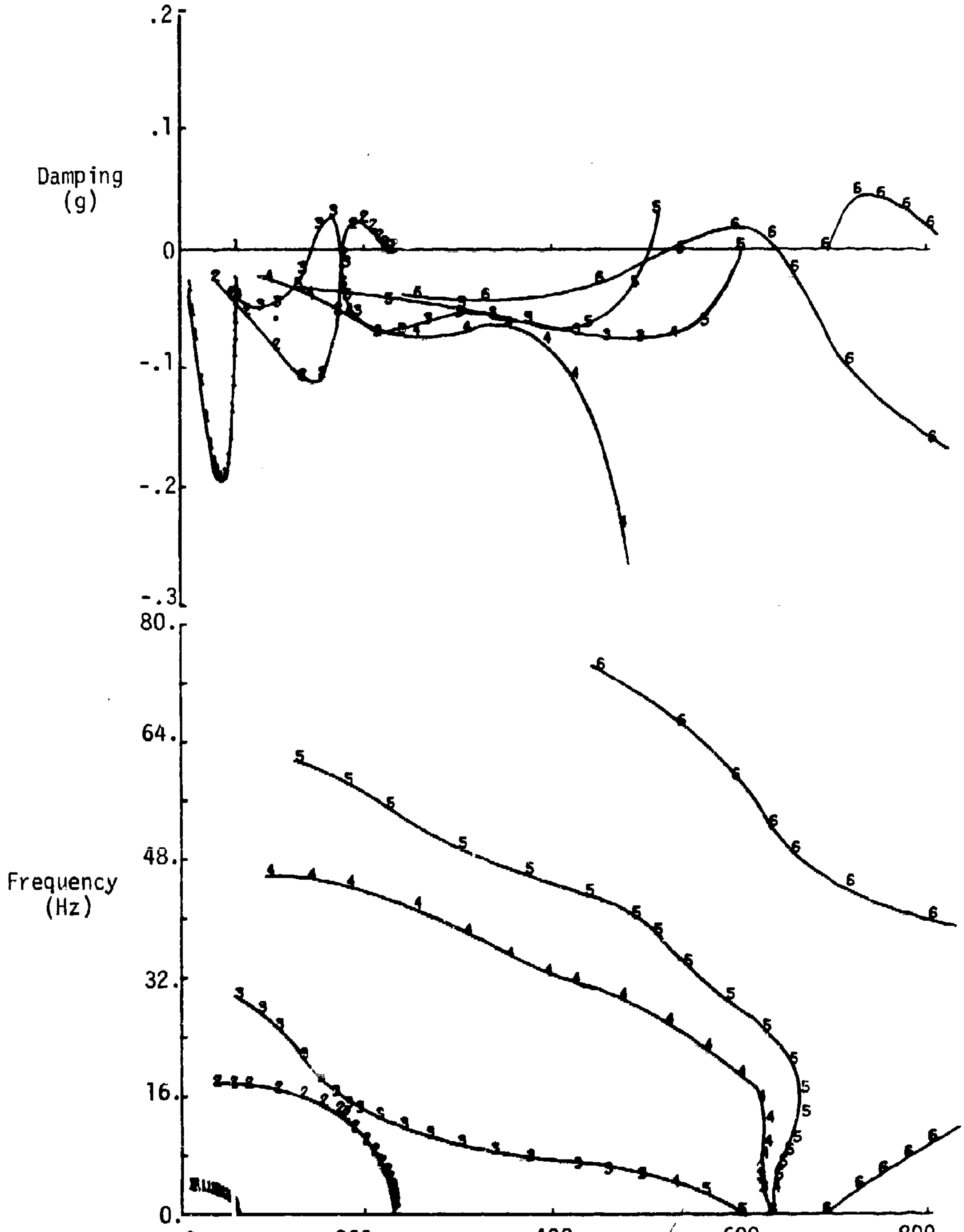

Figure C-8. TSO analysis V-g and V-ω curves. Nonrotated model, Λ = -30°.

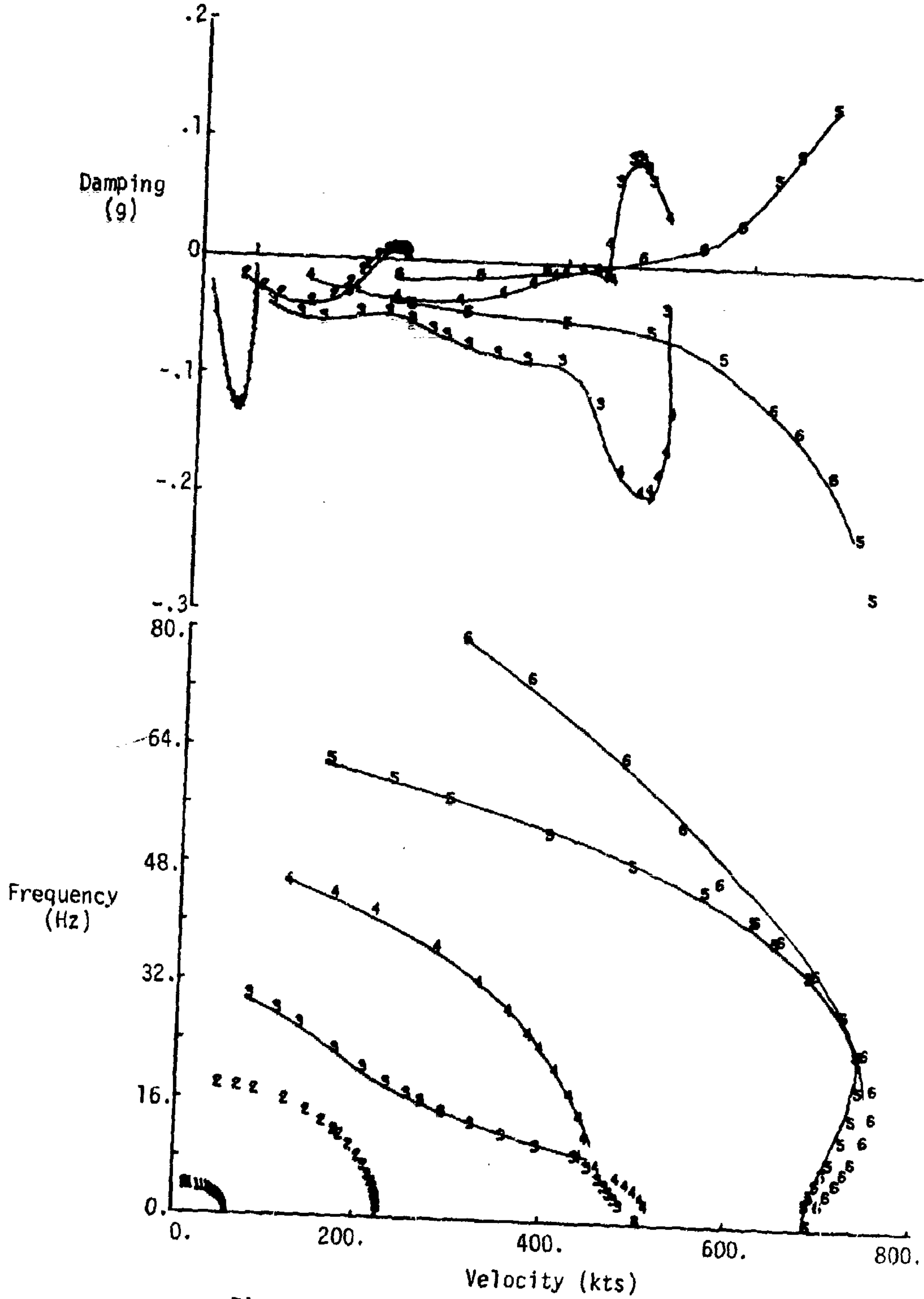

Figure C-9. TSO analysis V-g and V-ω curves.
Nonrotated model, Λ = -45°.

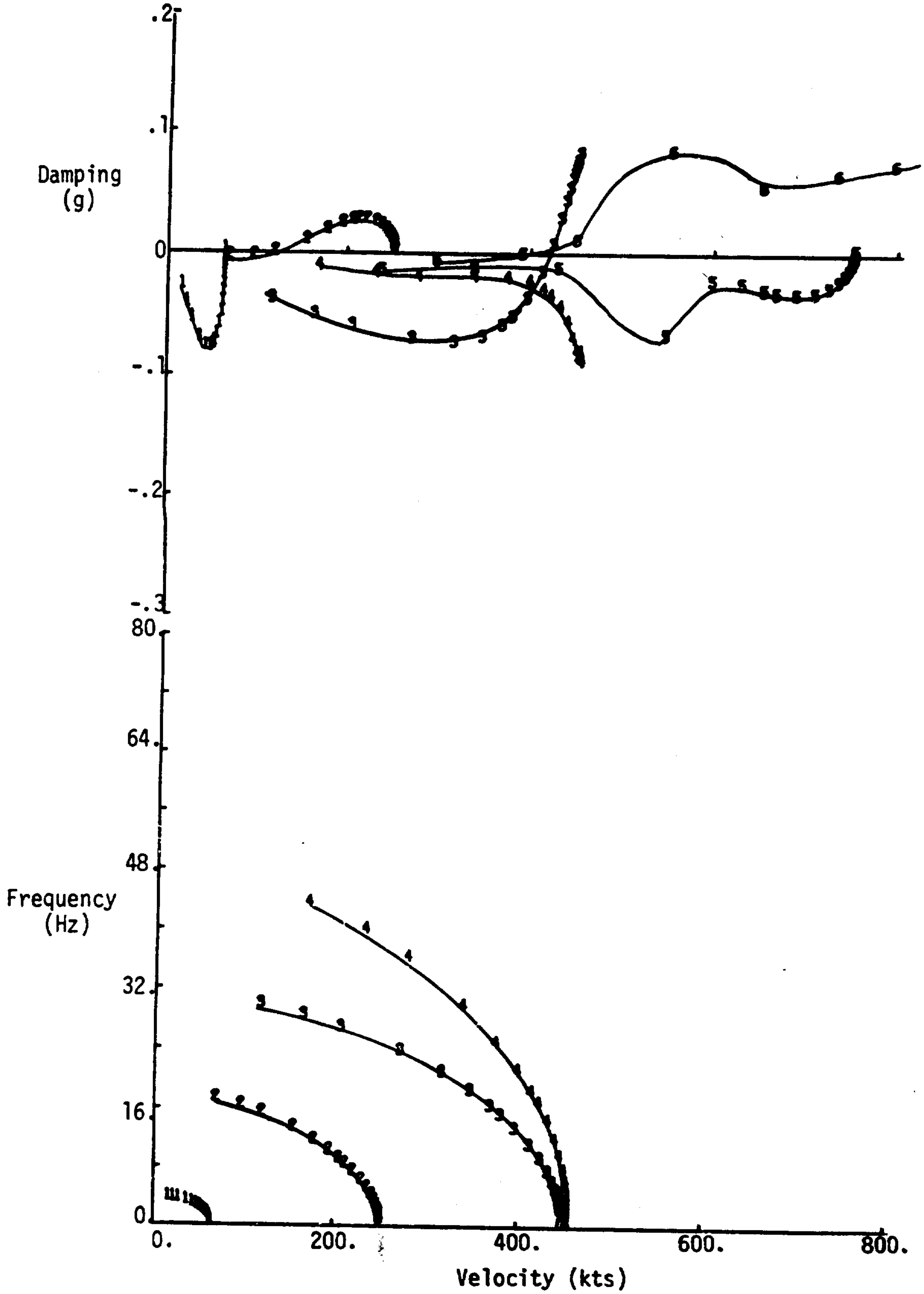

Figure C-10. TSO analysis V-g and V-ω curves.
Nonrotated model, Λ = -60°.

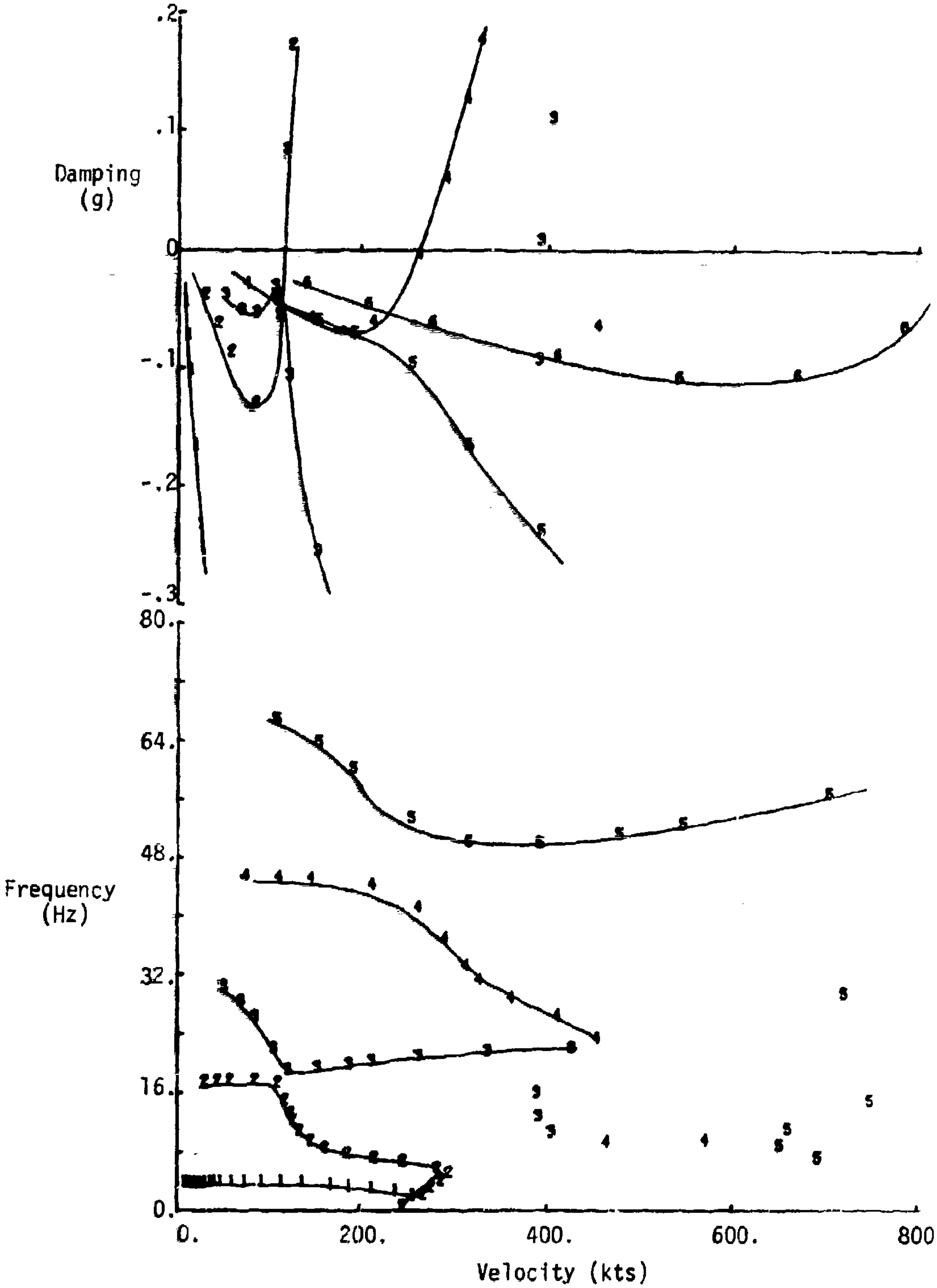

Figure C-11. TSO analysis V-g and V-ω curves.
7.5° rotated model, Λ = 0°.

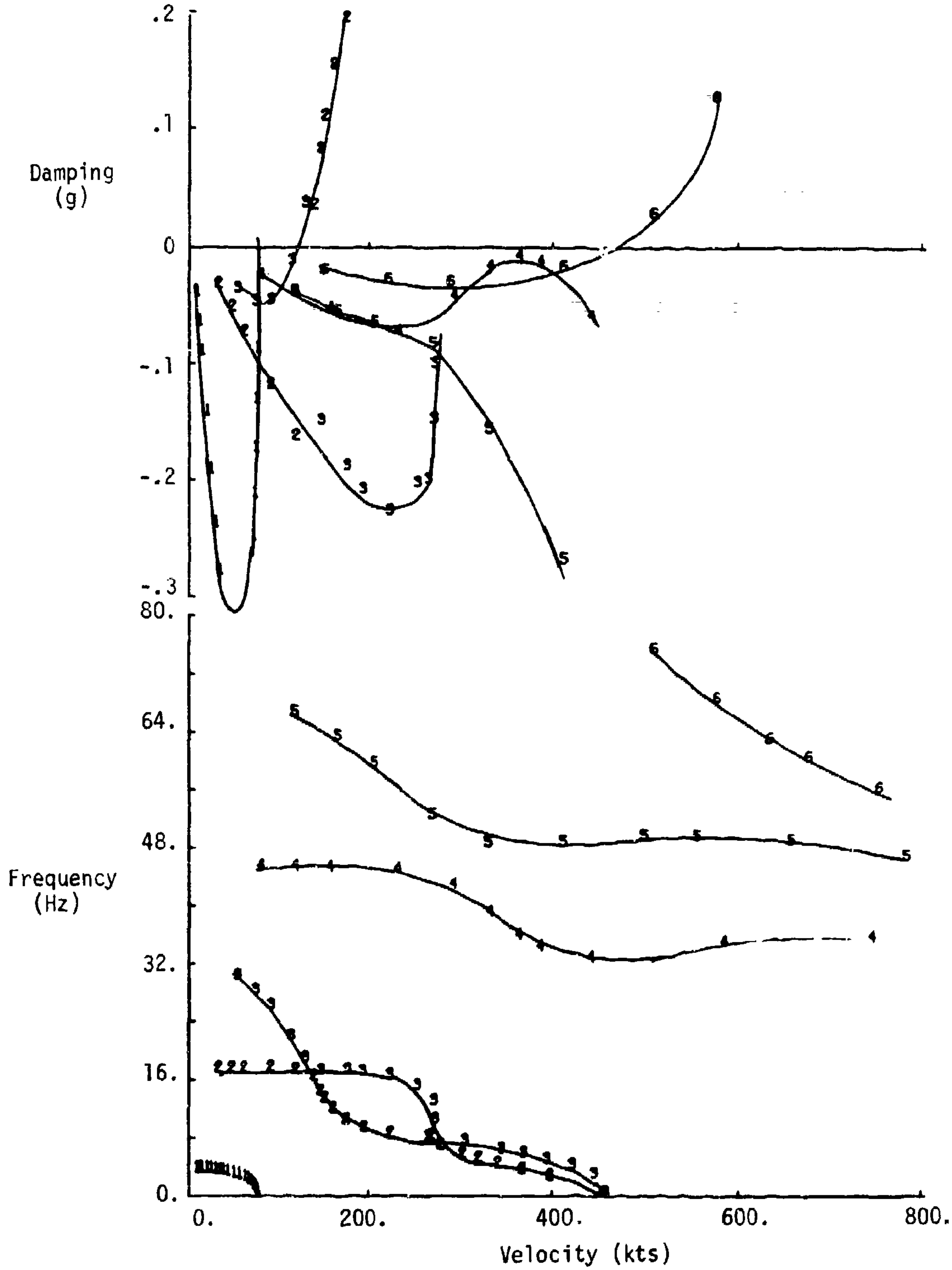

Figure C-12. TSO analysis V-g and V-ω curves.
7.5° rotated model, Λ = -15°.

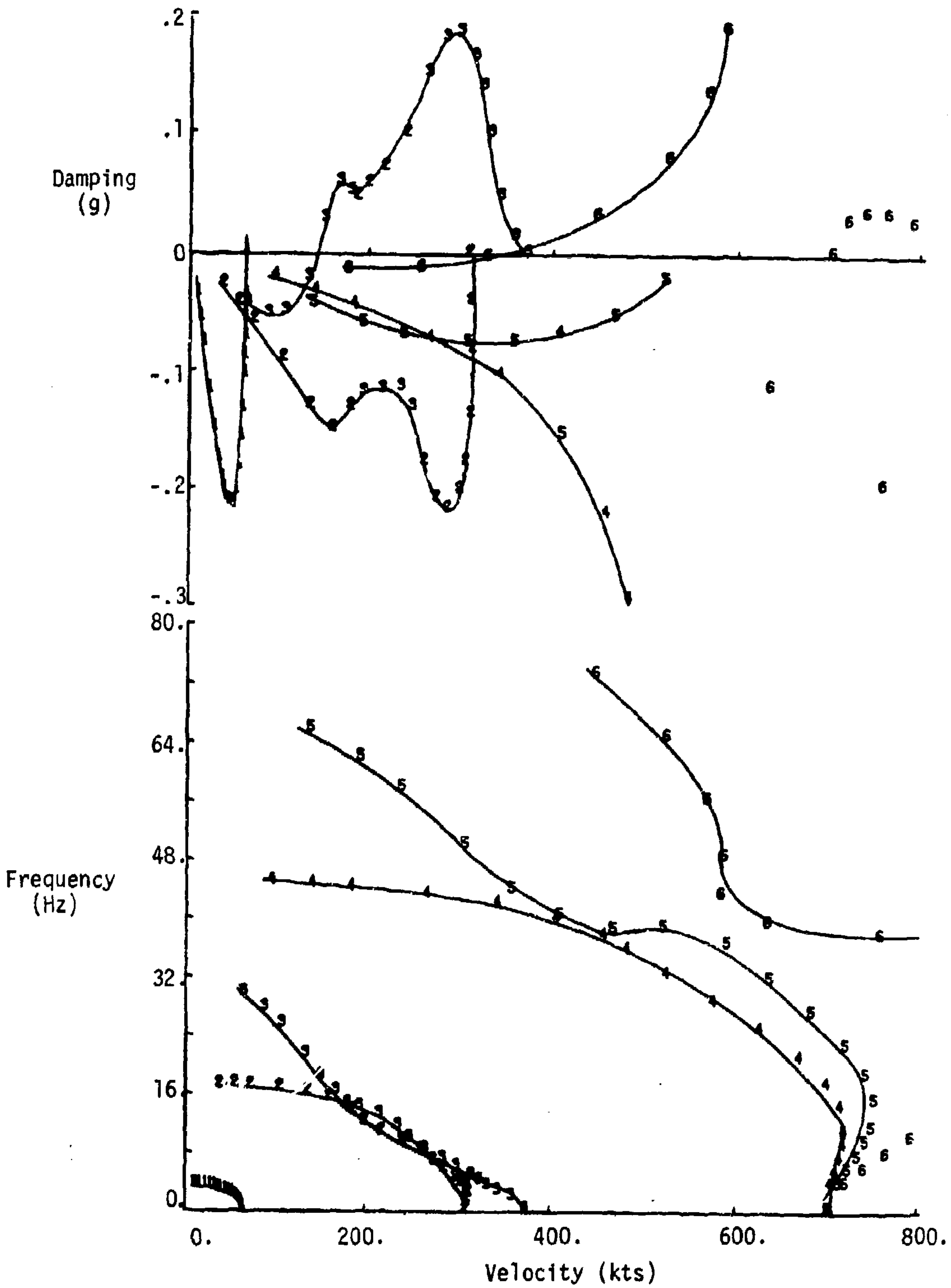

Figure C-13. TSO analysis V-g and V-ω curves
7.5° rotated model, Λ = -30°.

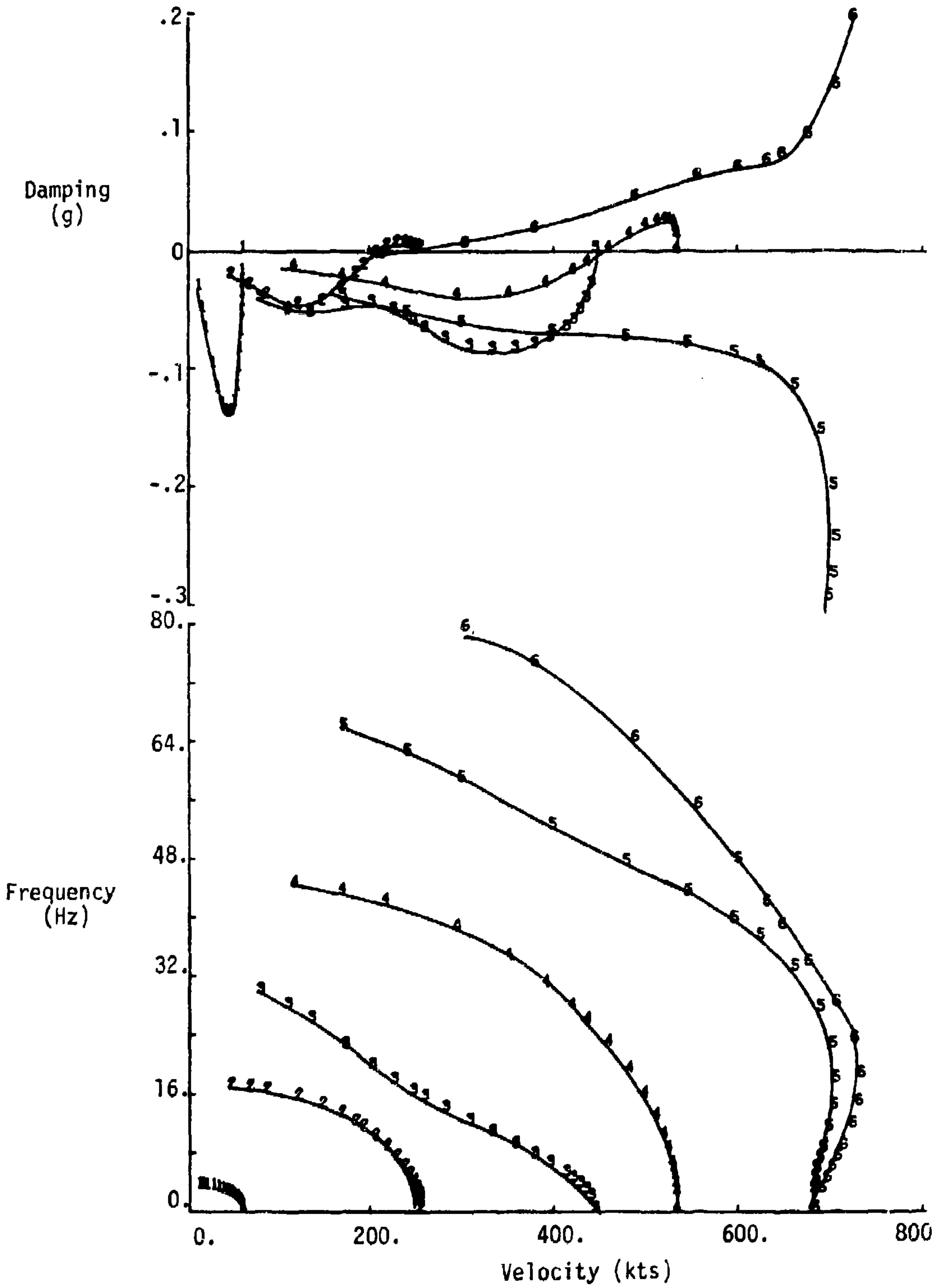

Figure C-14. TSO analysis V-g and V-ω curves.
7.5° rotated model, Λ = -45°.

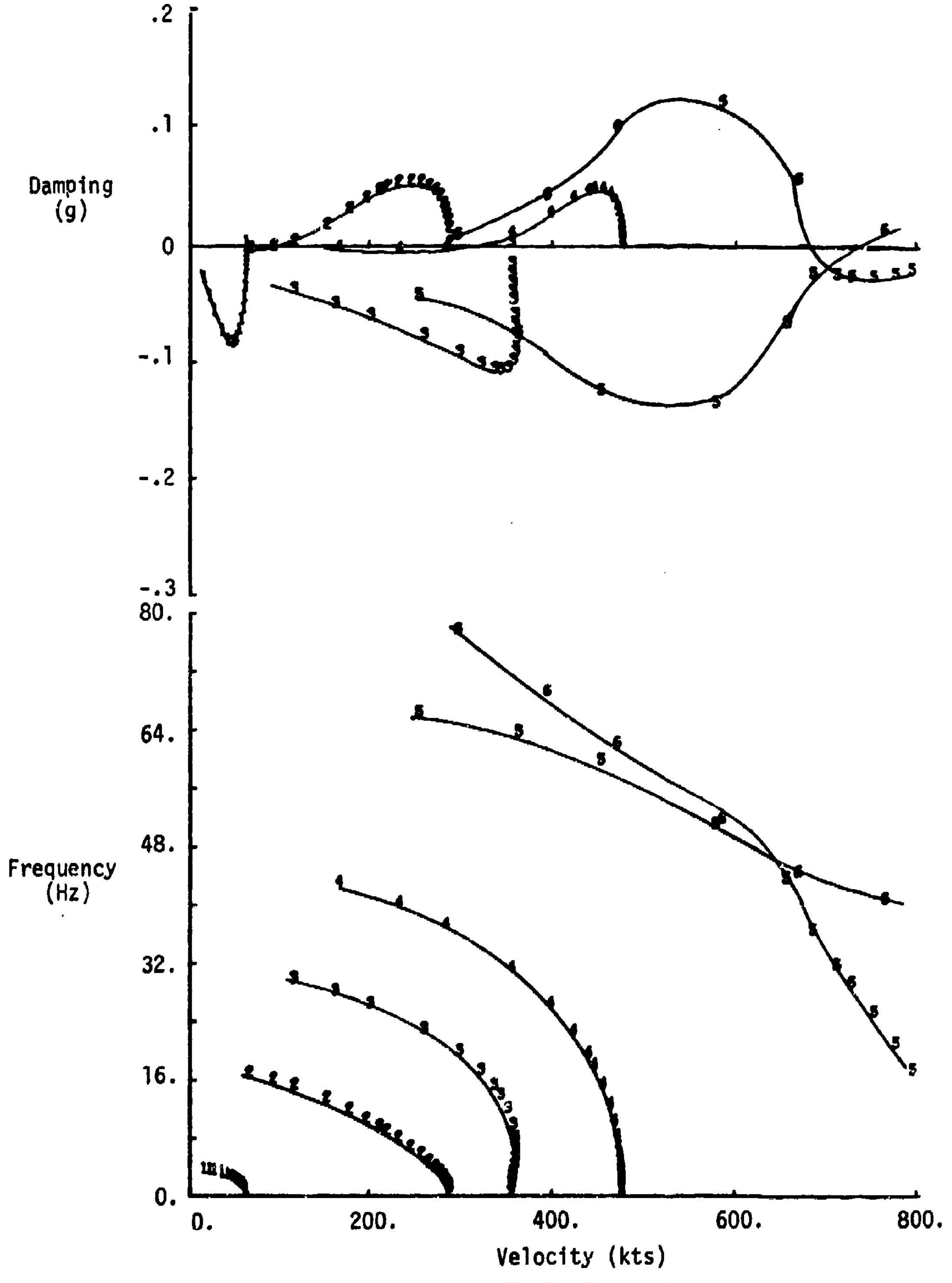

Figure C-15. TSO analysis V-g and V-ω curves, 7.5° rotated model, Λ = -60°.

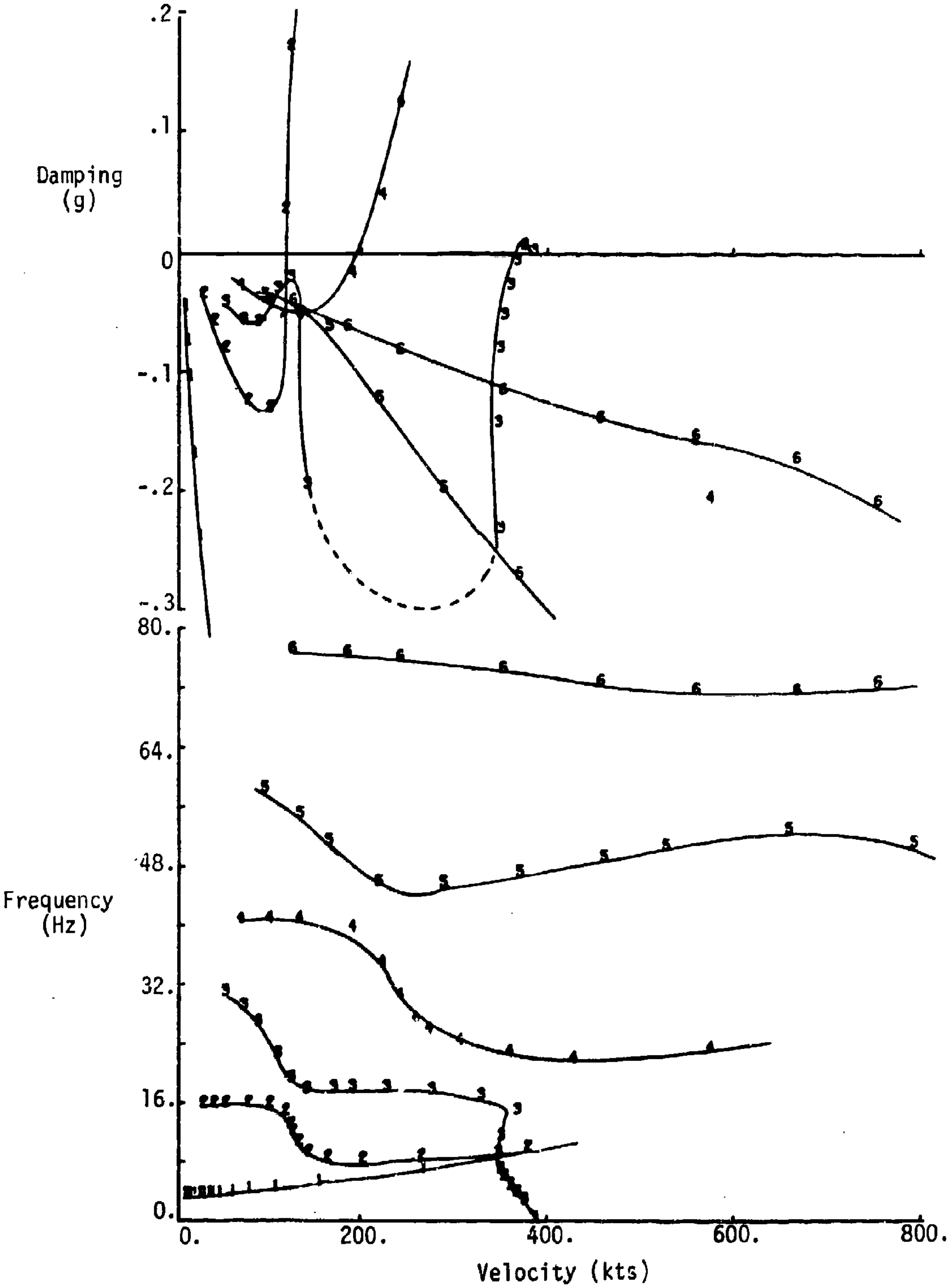

Figure C-16. TSO analysis V-g and V-ω curves. 15° rotated model, Λ = 0°.

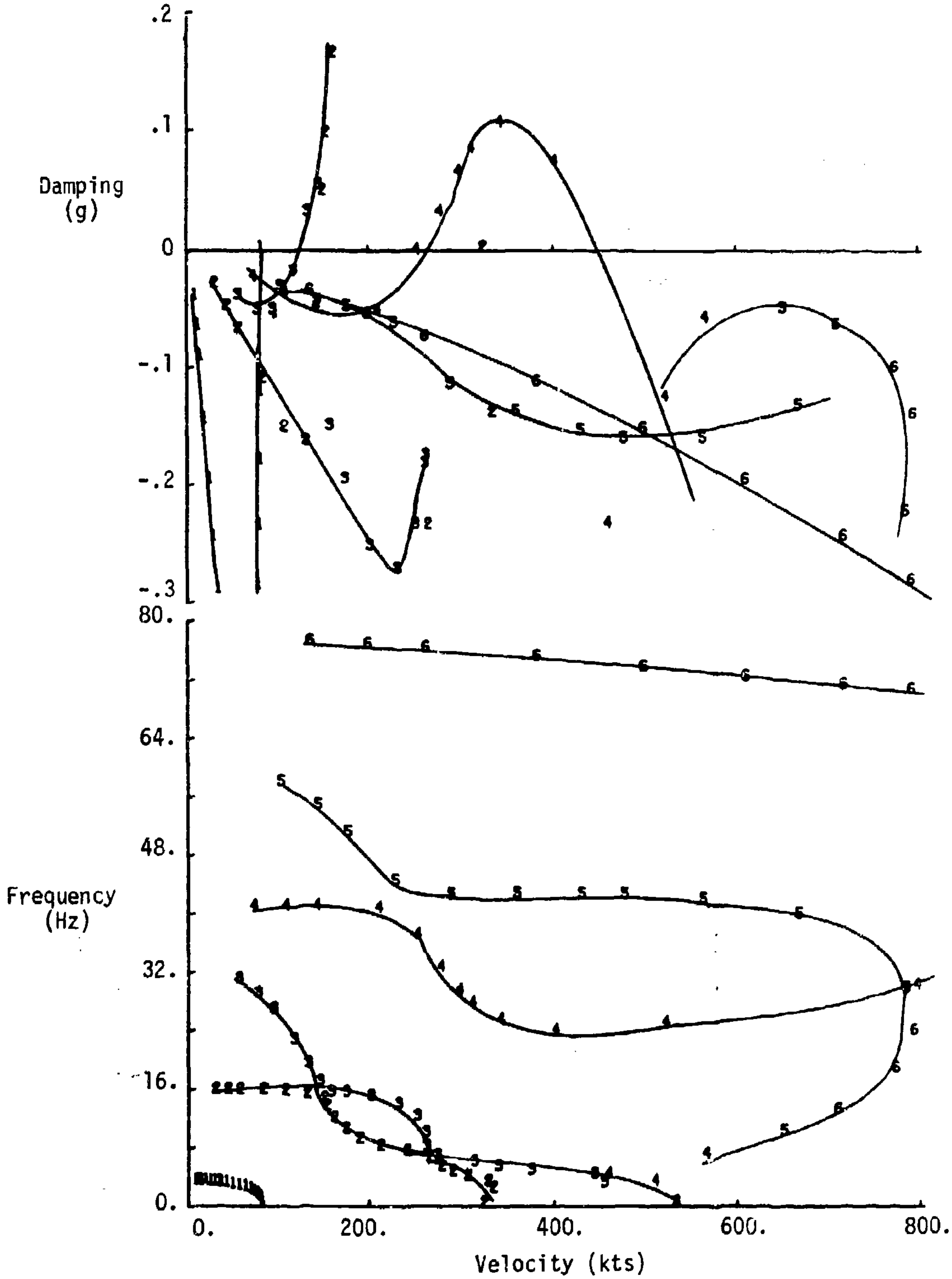

Figure C-17. TSO analysis V-g and V-ω curves. 15° rotated model, Λ = -15°.

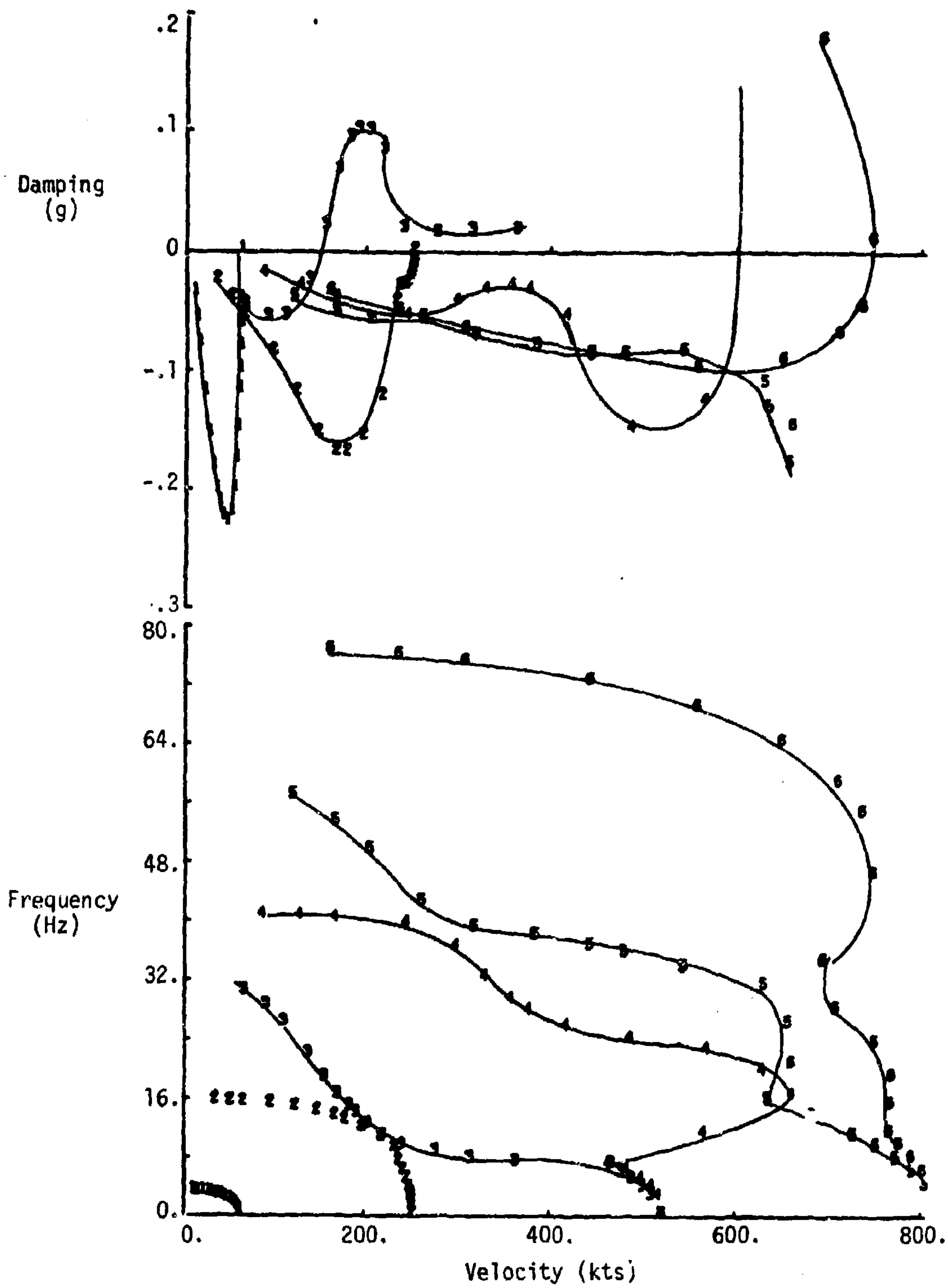

Figure C-18. TSO analysis V-g and V-ω curves.
15° rotated model, Λ = -30°.

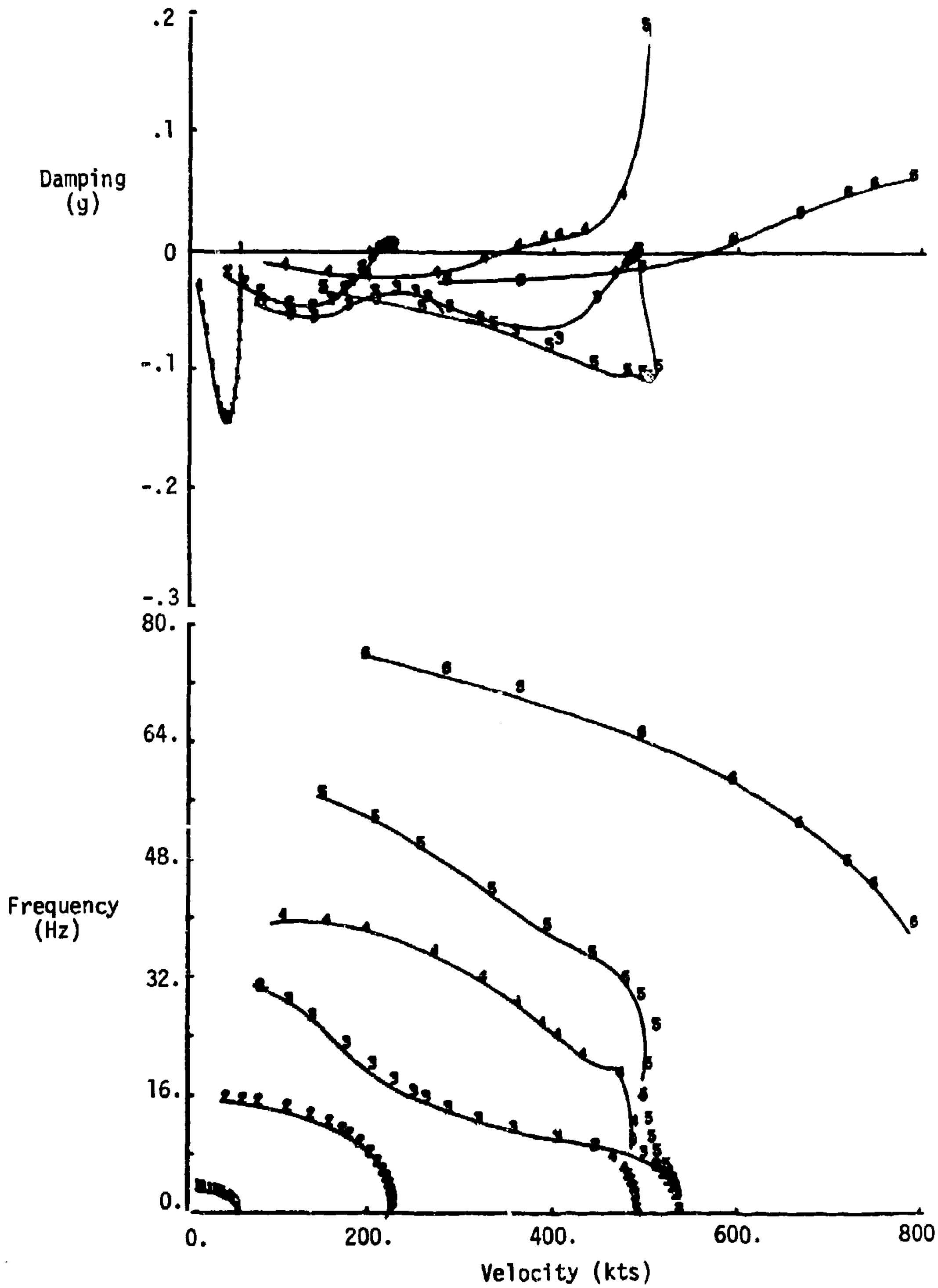

Figure C-19. TSO analysis V-g and V-ω curves.
15° rotated model, Λ = -45°.

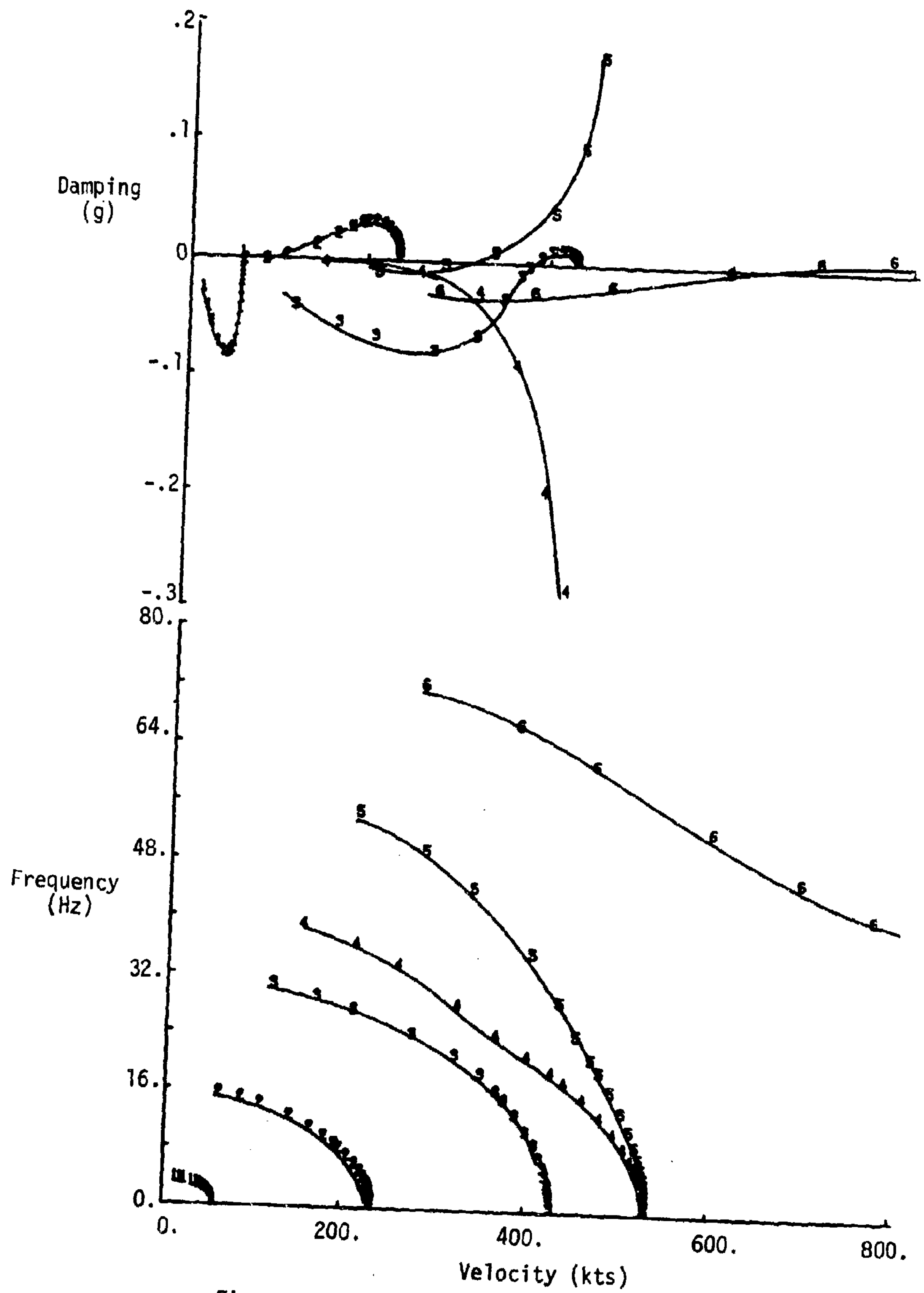

Figure C-20. TSO analysis V-g and V-ω curves.
15° rotated model, Λ = -60°.

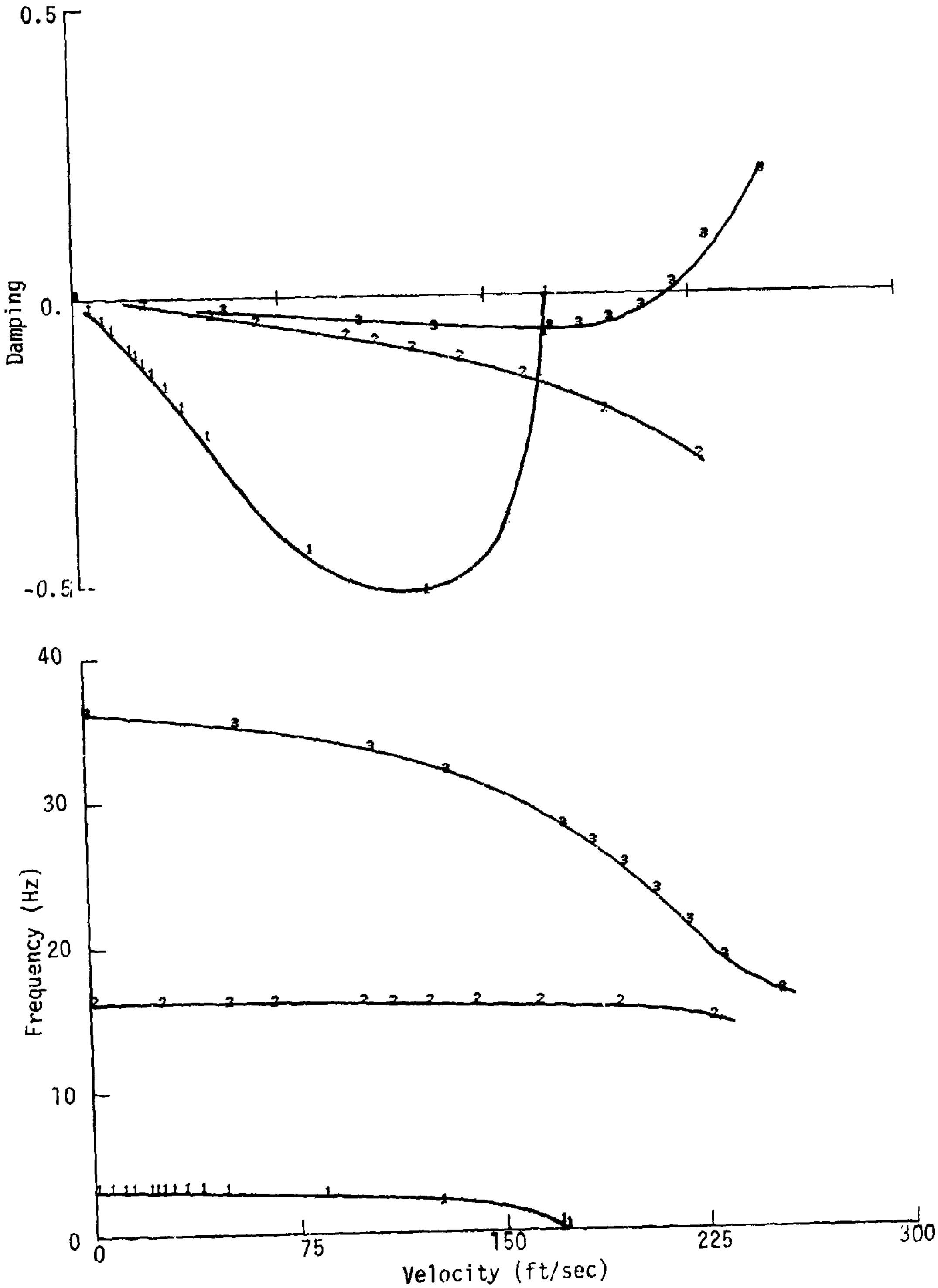

Figure C-21. NASTRAN analysis V-g and V-ω curves.
Aluminum model, Λ = 0°.

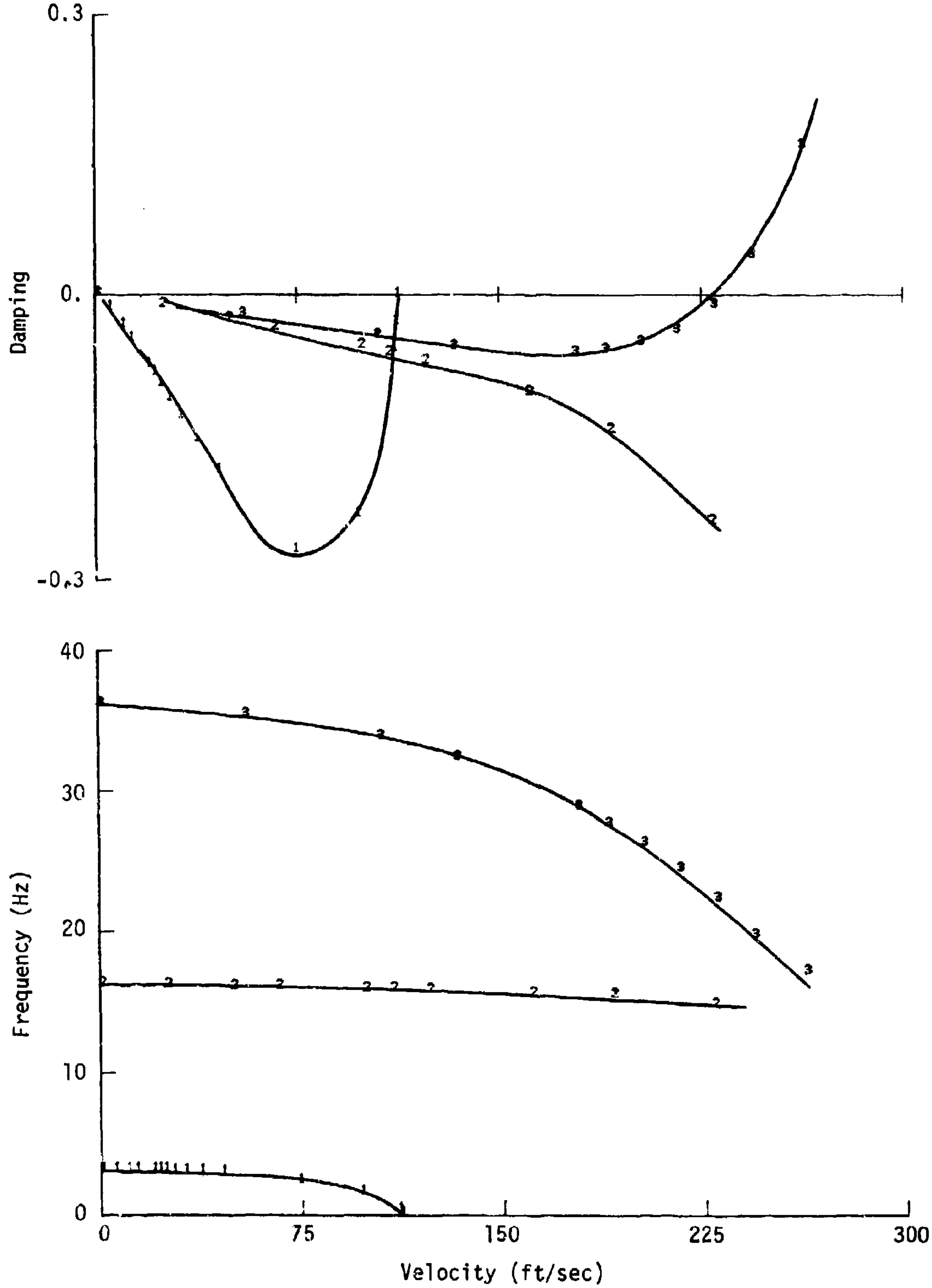

Figure C-22. NASTRAN analysis V-g and V-ω curves. Aluminum model, Λ = -15°.

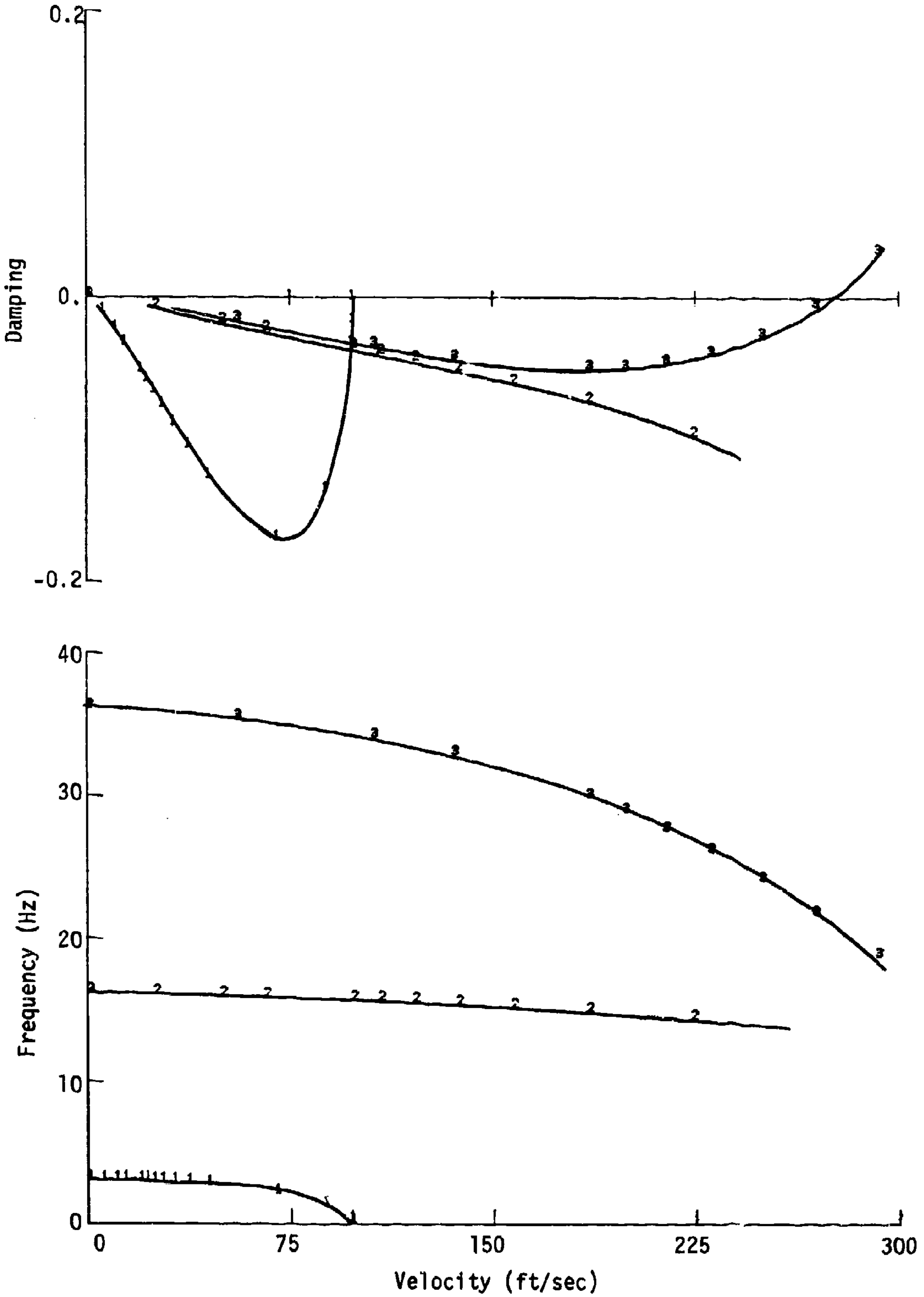

Figure C-23. NASTRAN analysis V-g and V-ω curves.
Aluminum model, Λ = -30°.

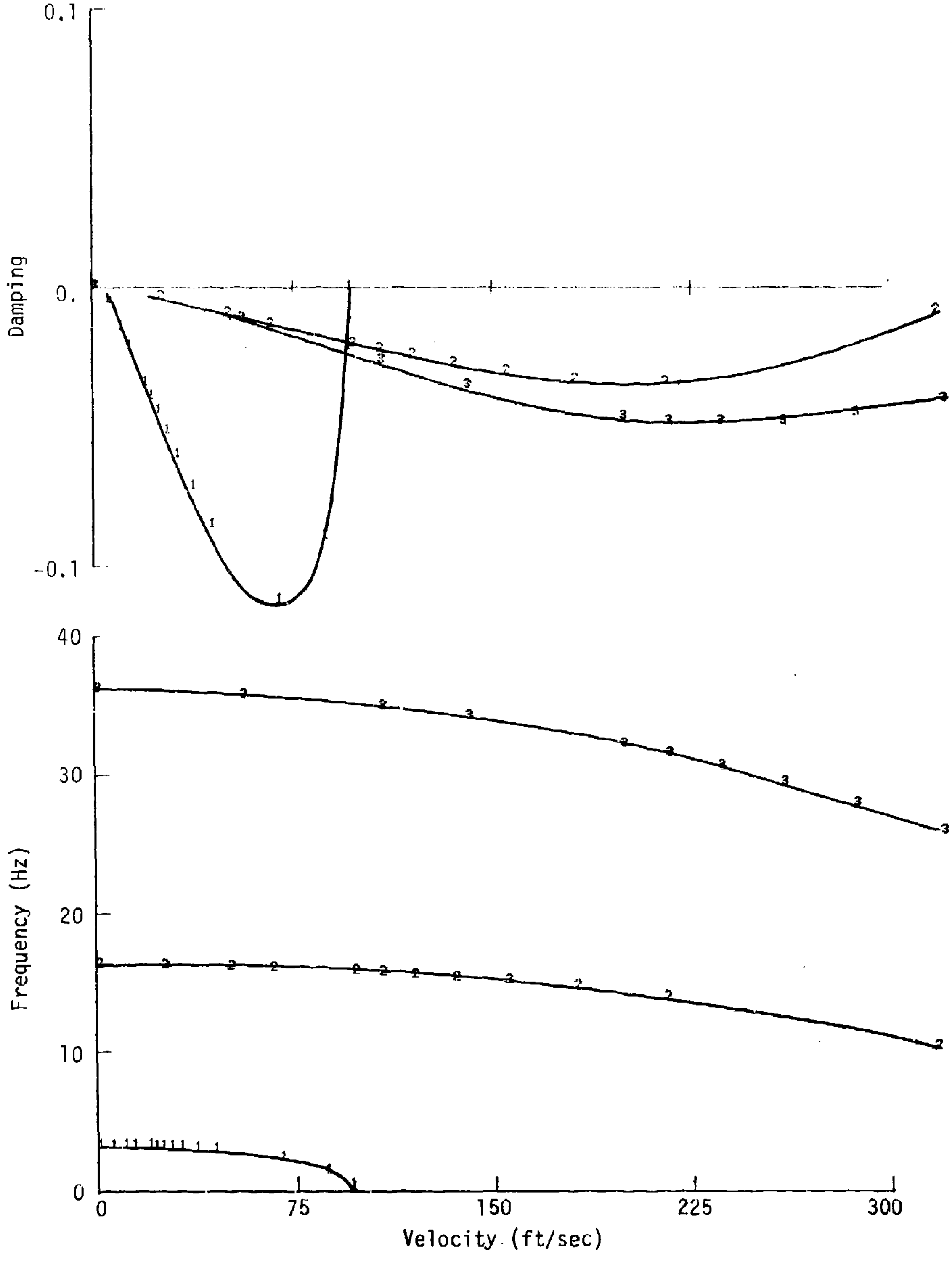

Figure C-24. NASTRAN analysis V-g and V-ω curves. Aluminum model, Λ = -45°.

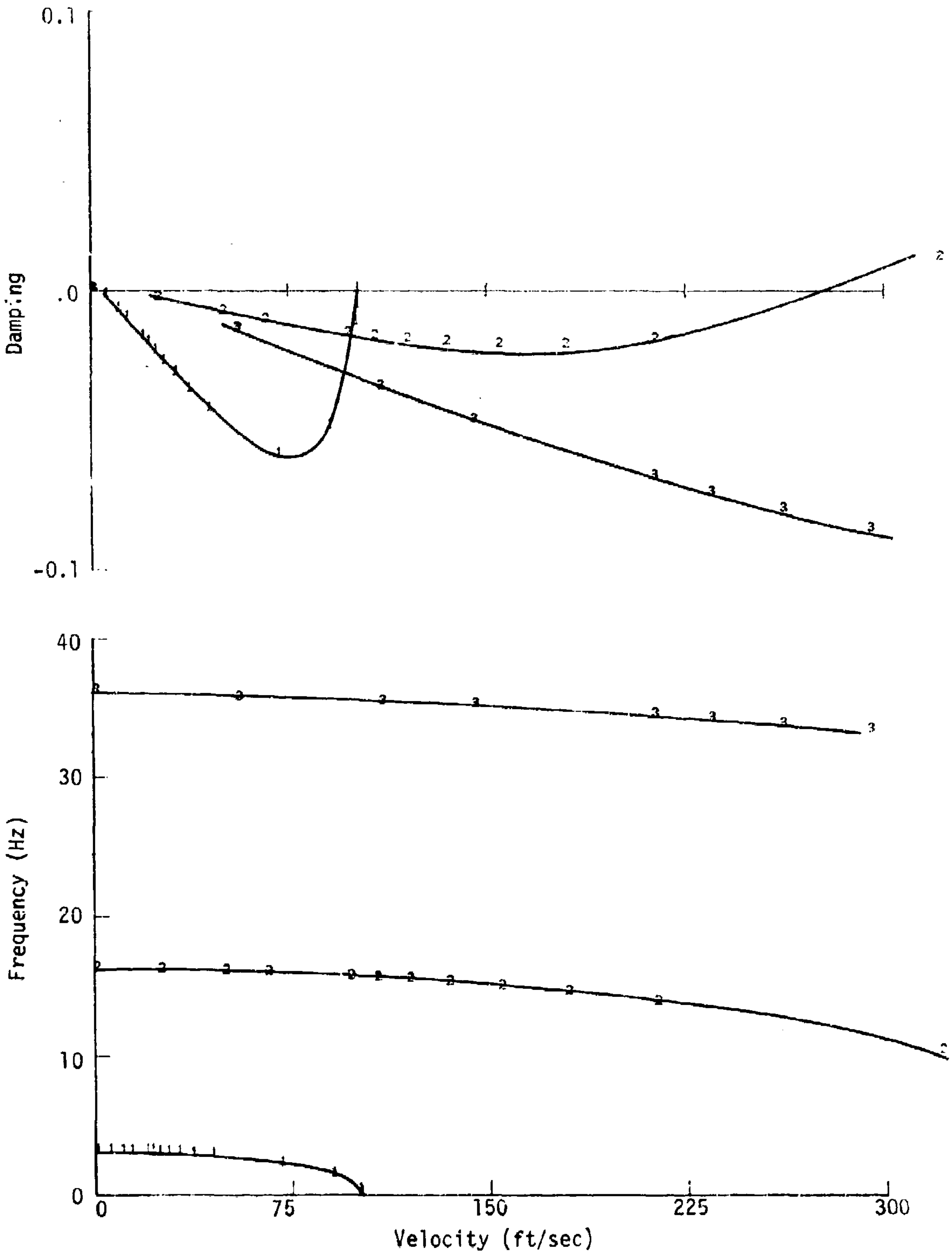

Figure C-25. NASTRAN analysis V-g and V-ω curves.
Aluminum model, Λ = -60°.

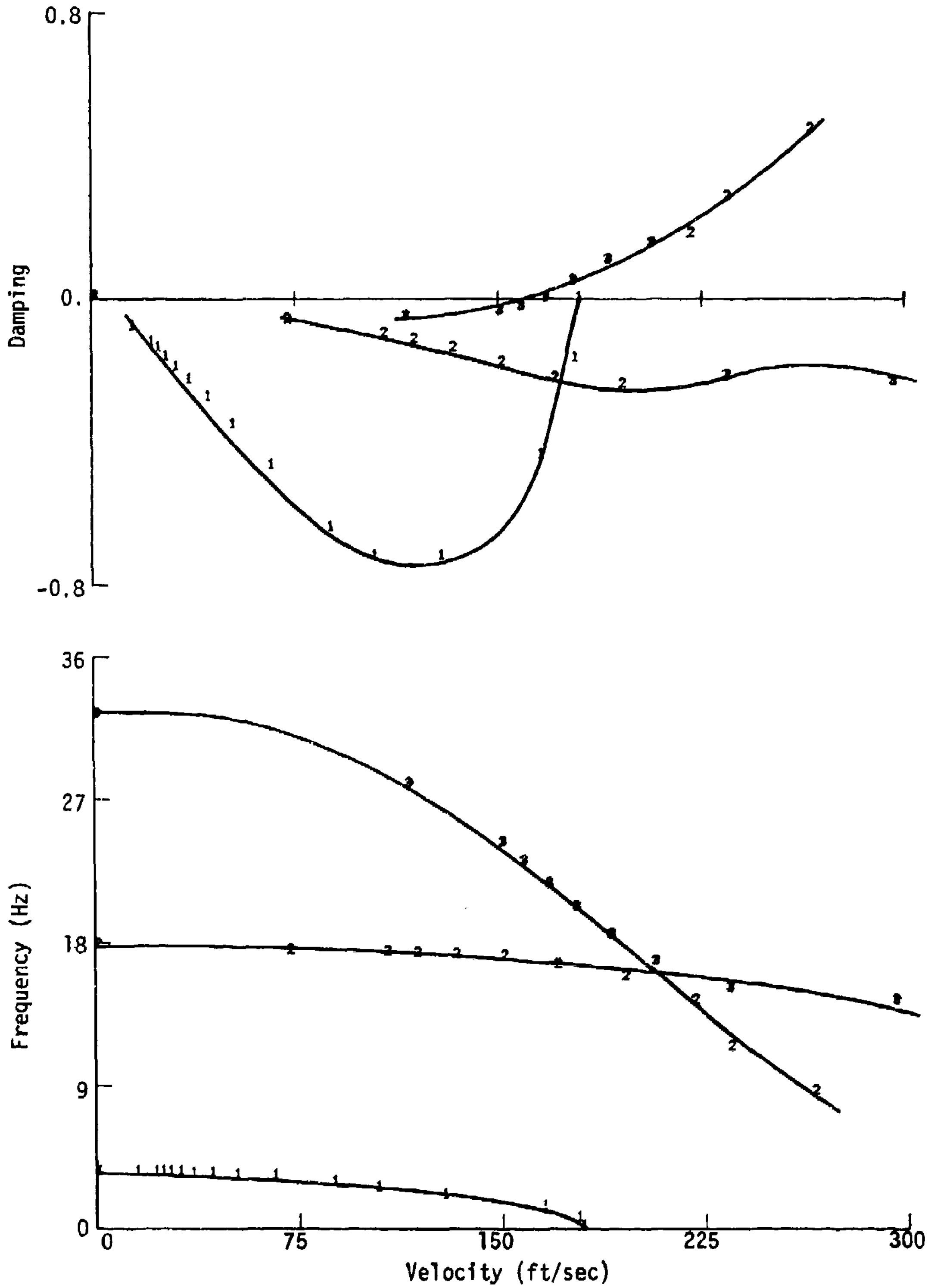

Figure C-26. NASTRAN analysis V-g and V-ω curves. Nonrotated model, Λ = 0°.

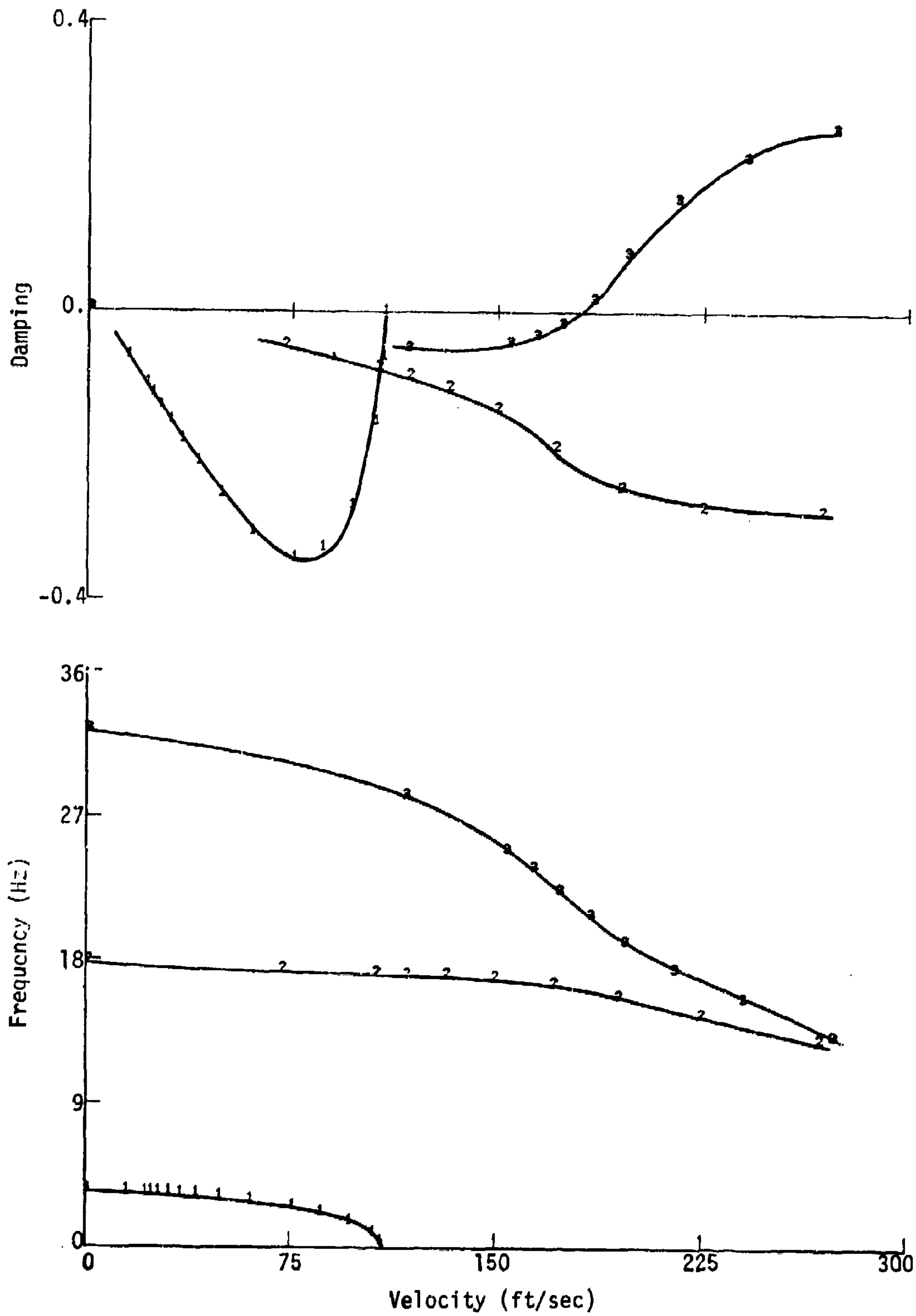

Figure C-27. NASTRAN analysis V-g and V-ω curves. Nonrotated model, Λ = -15°.

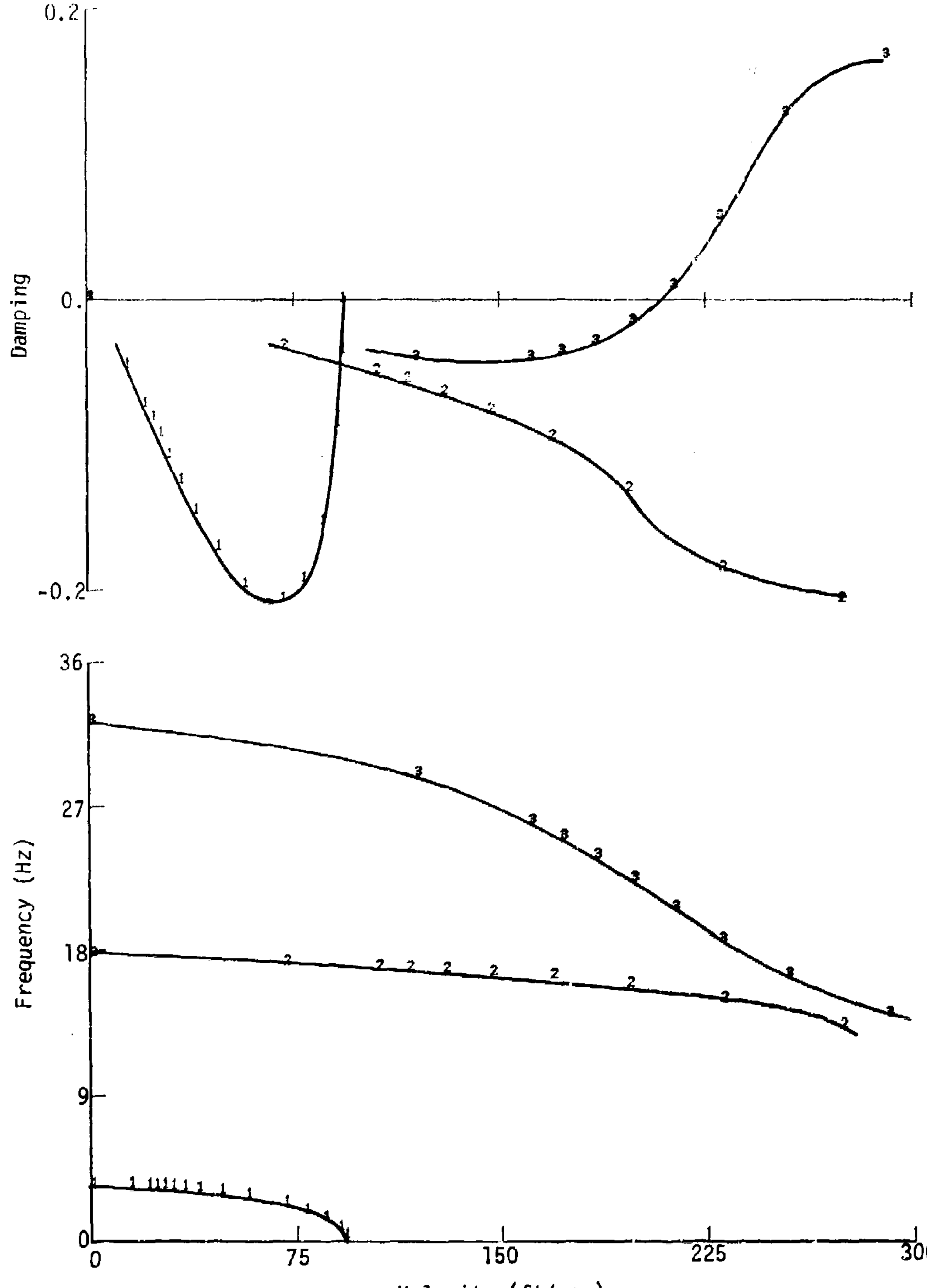

Figure C-28. NASTRAN analysis V-g and V-ω curves. Nonrotated model, Λ = -30°.

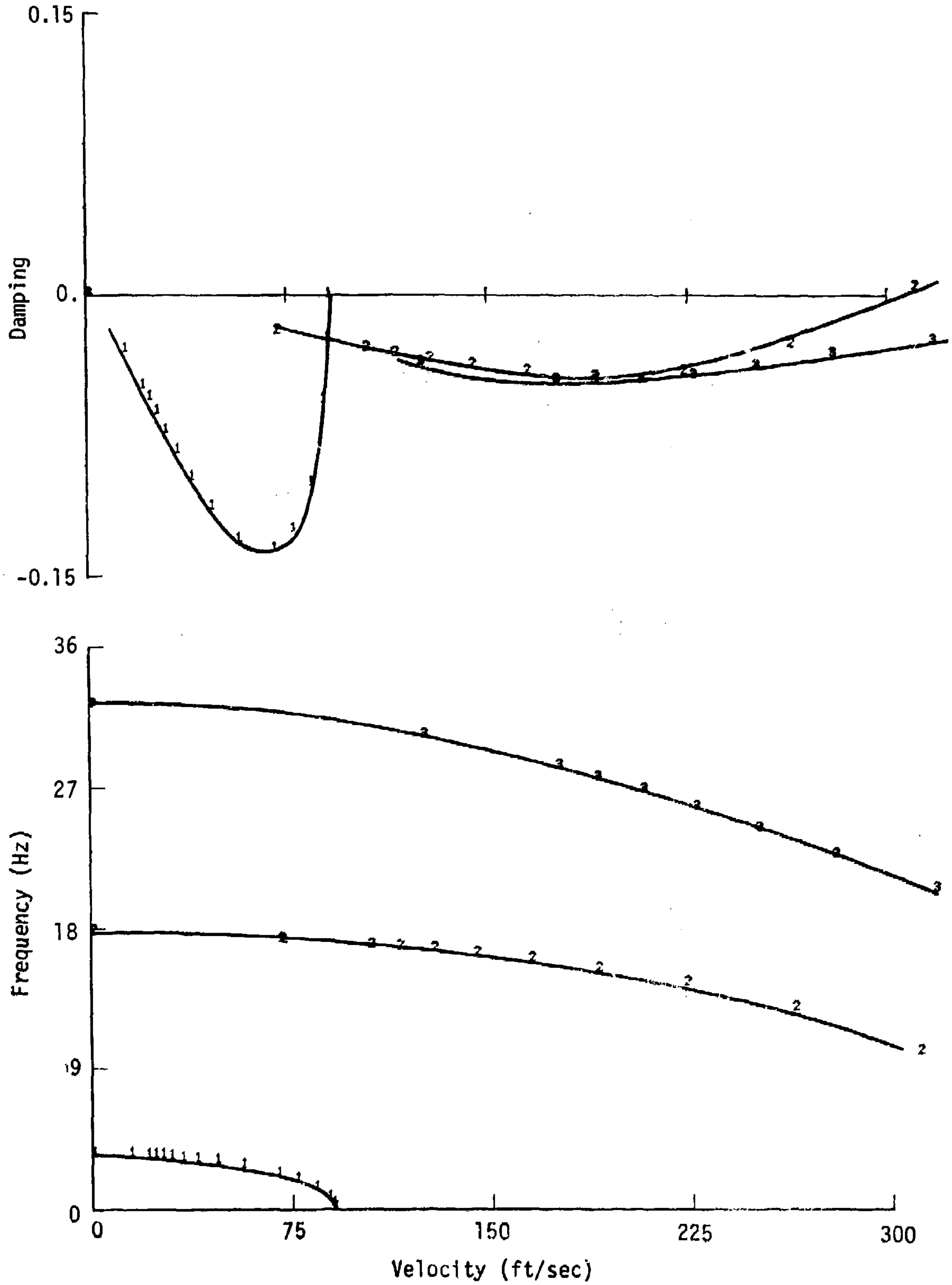

Figure C-29. NASTRAN analysis V-g and V-ω curves.
Nonrotated model, Λ = -45°.

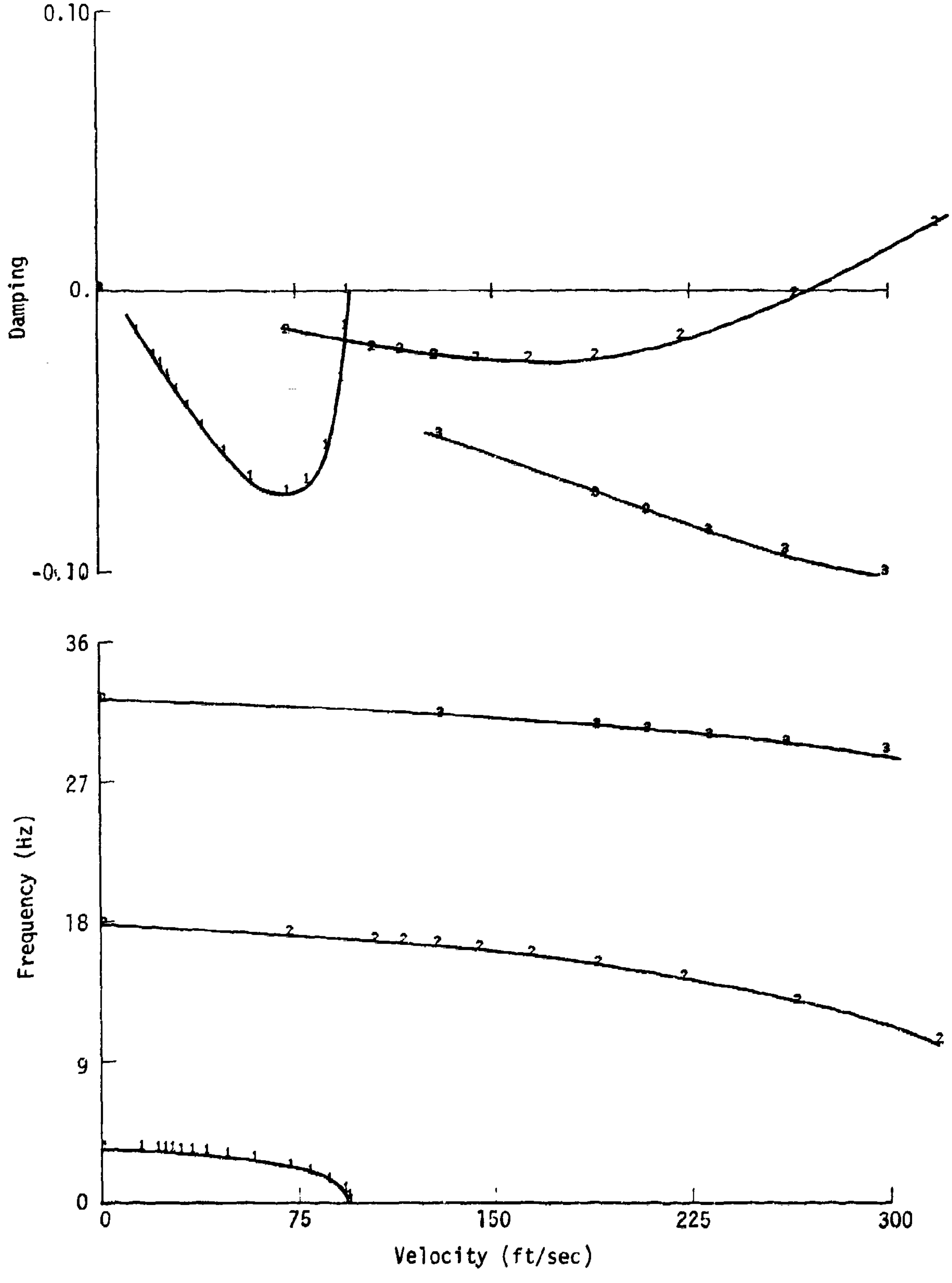

Figure C-30. NASTRAN analysis V-g and V-ω curves.
Nonrotated model, Λ = -60°.

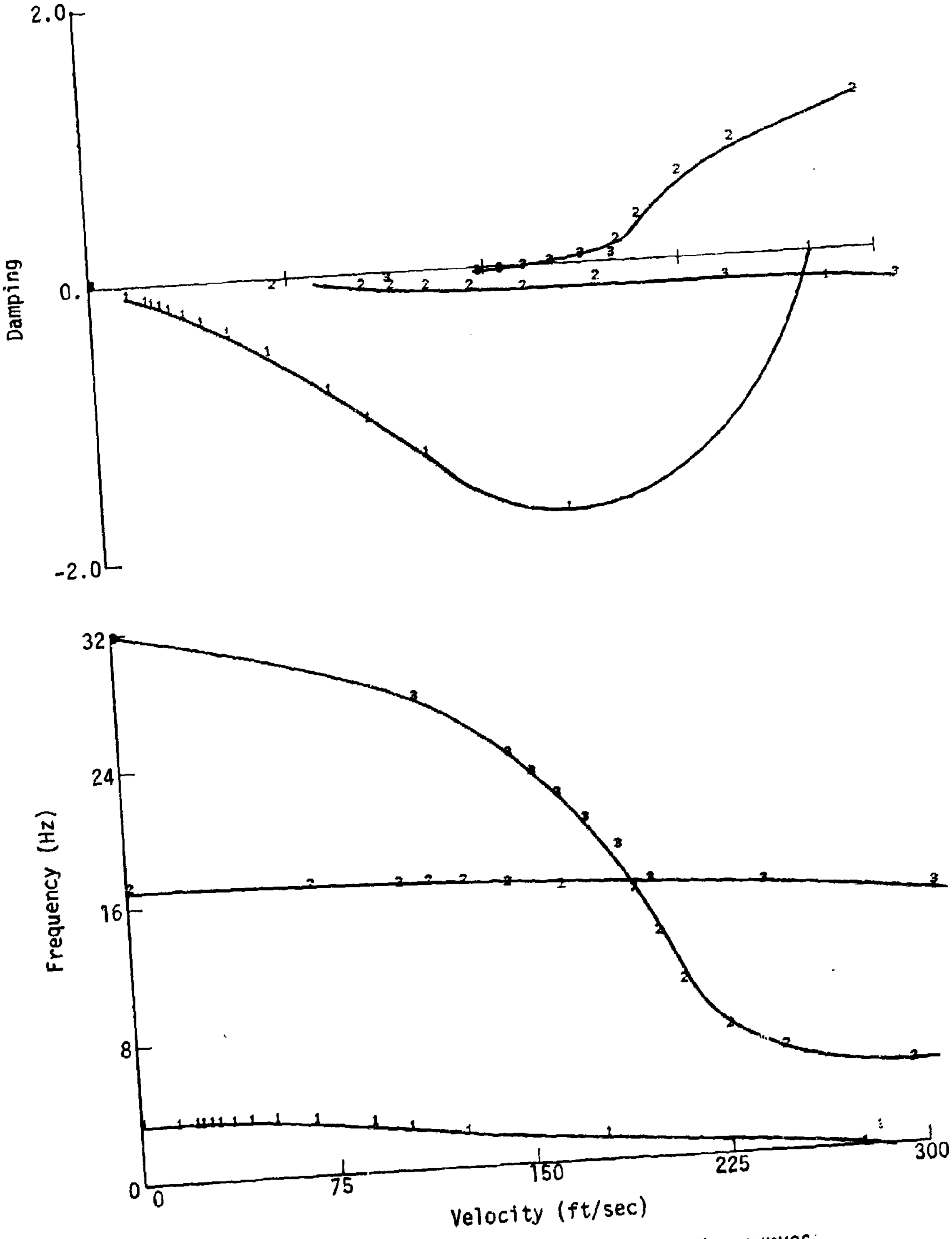

Figure C-31. NASTRAN analysis V-g and V-ω curves. 7.5° rotated model, Λ = 0°.

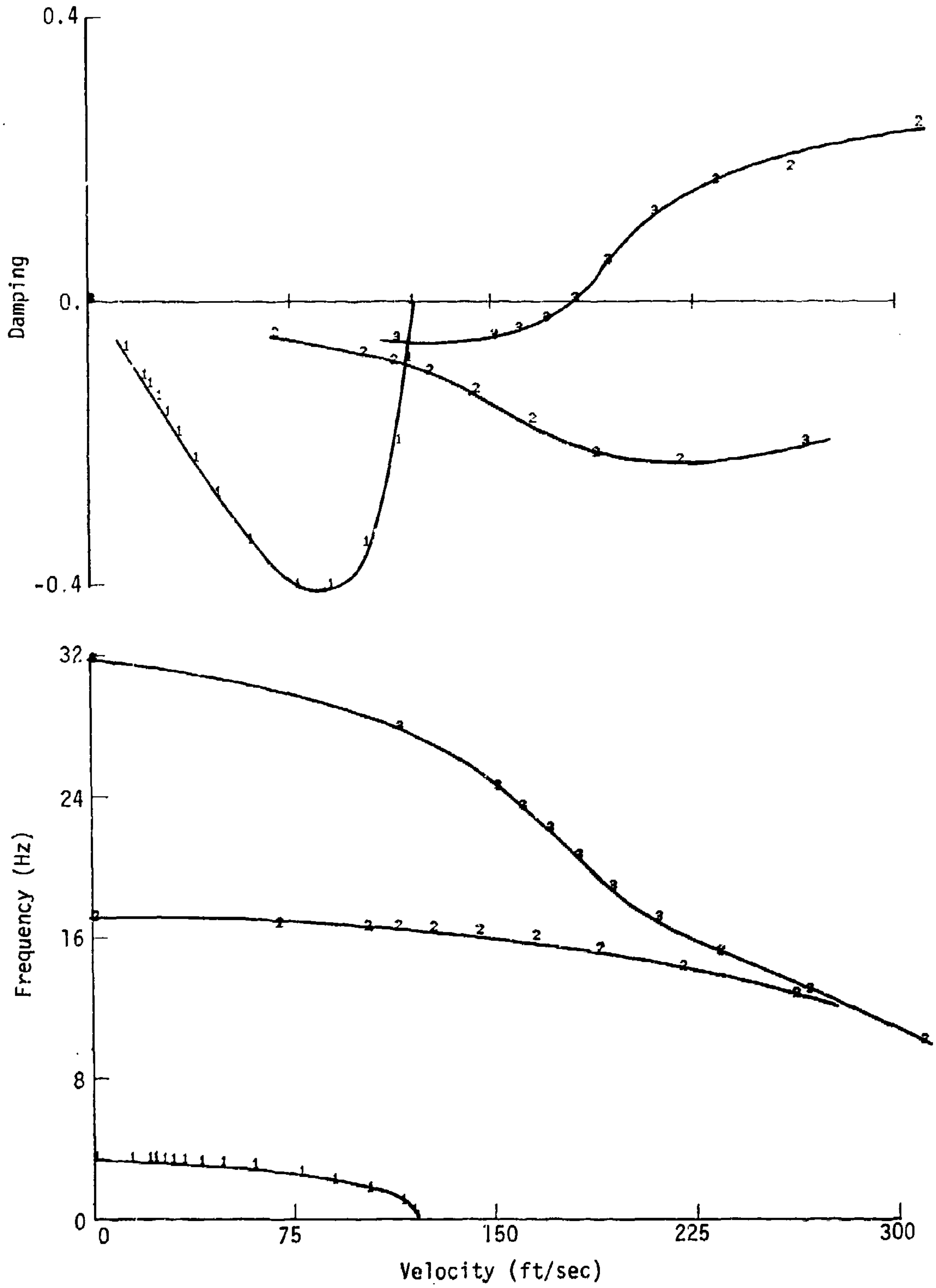

Figure C-32. NASTRAN analysis V-g and V-ω curves. 7.5° rotated model, Λ = -15°.

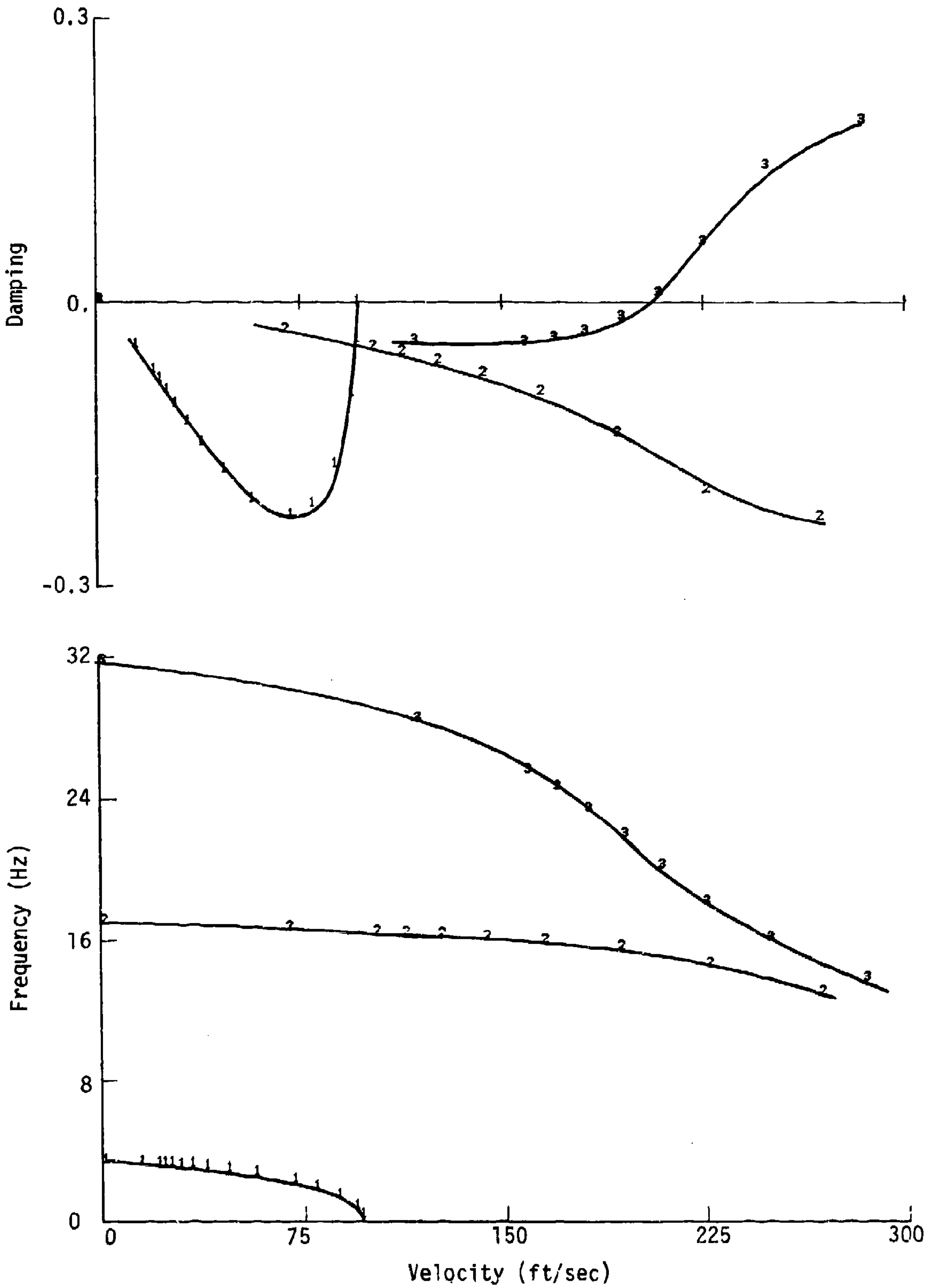

Figure C-33. NASTRAN analysis V-g and V-ω curves. 7.5° rotated model, Λ = -30°.

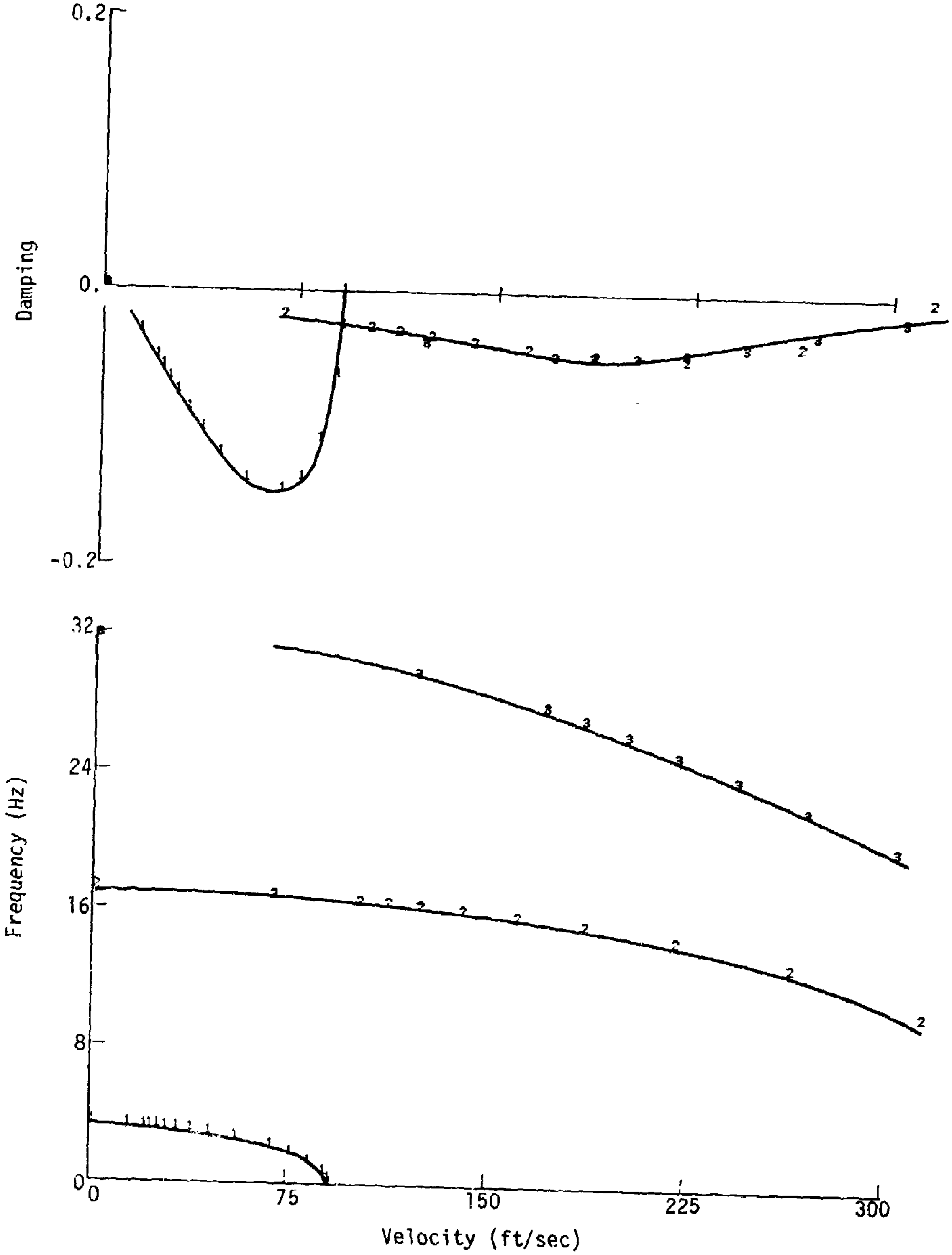

Figure C-34. NASTRAN analysis V-g and V-ω curves.
7.5° rotated model, Λ = -45°.

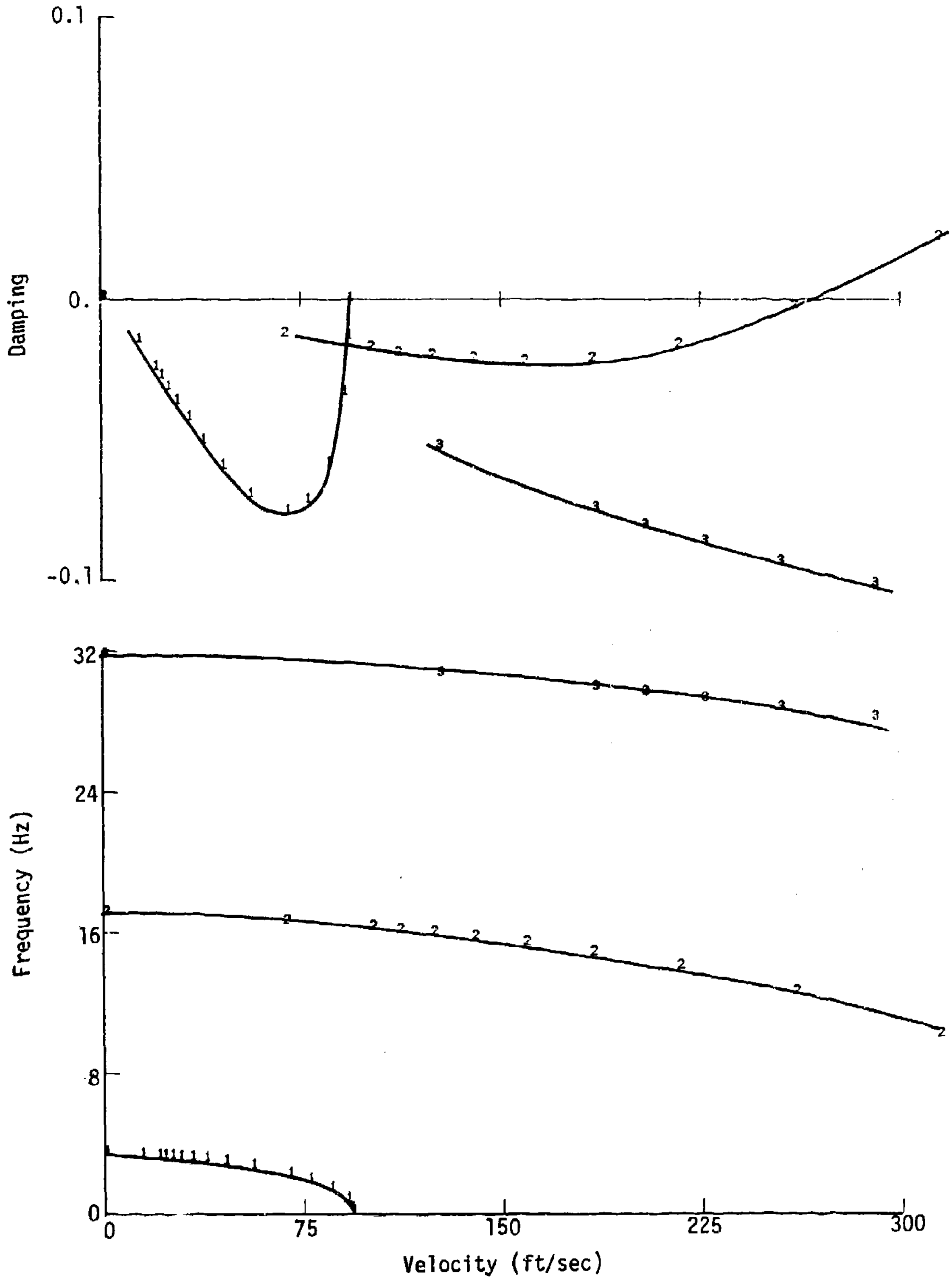

Figure C-35. NASTRAN analysis V-g and V-ω curves.
7.5° rotated model, Λ = -60°.

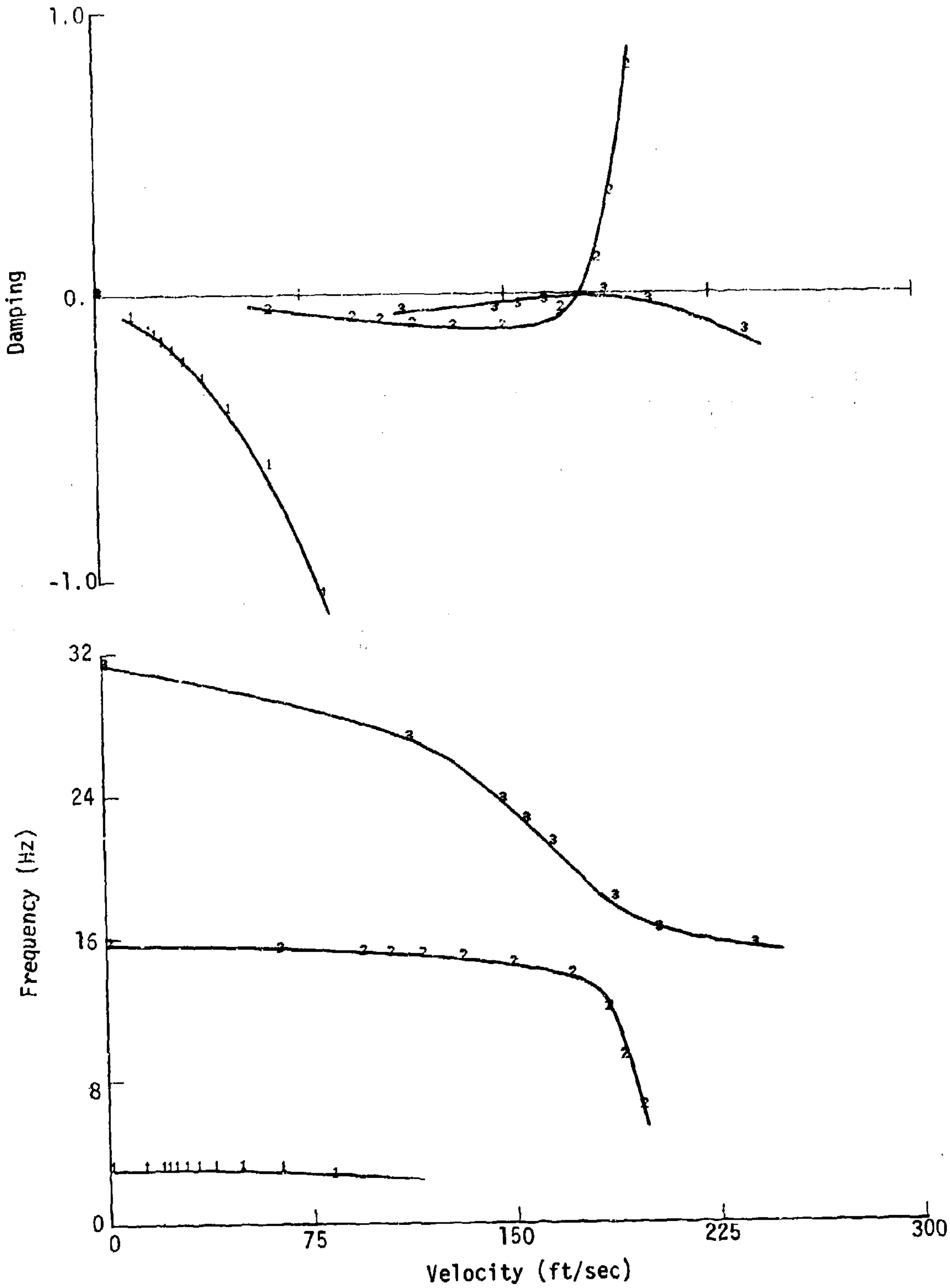

Figure C-36. NASTRAN analysis V-g and V-ω curves.
15° rotated model, Λ = 0°.

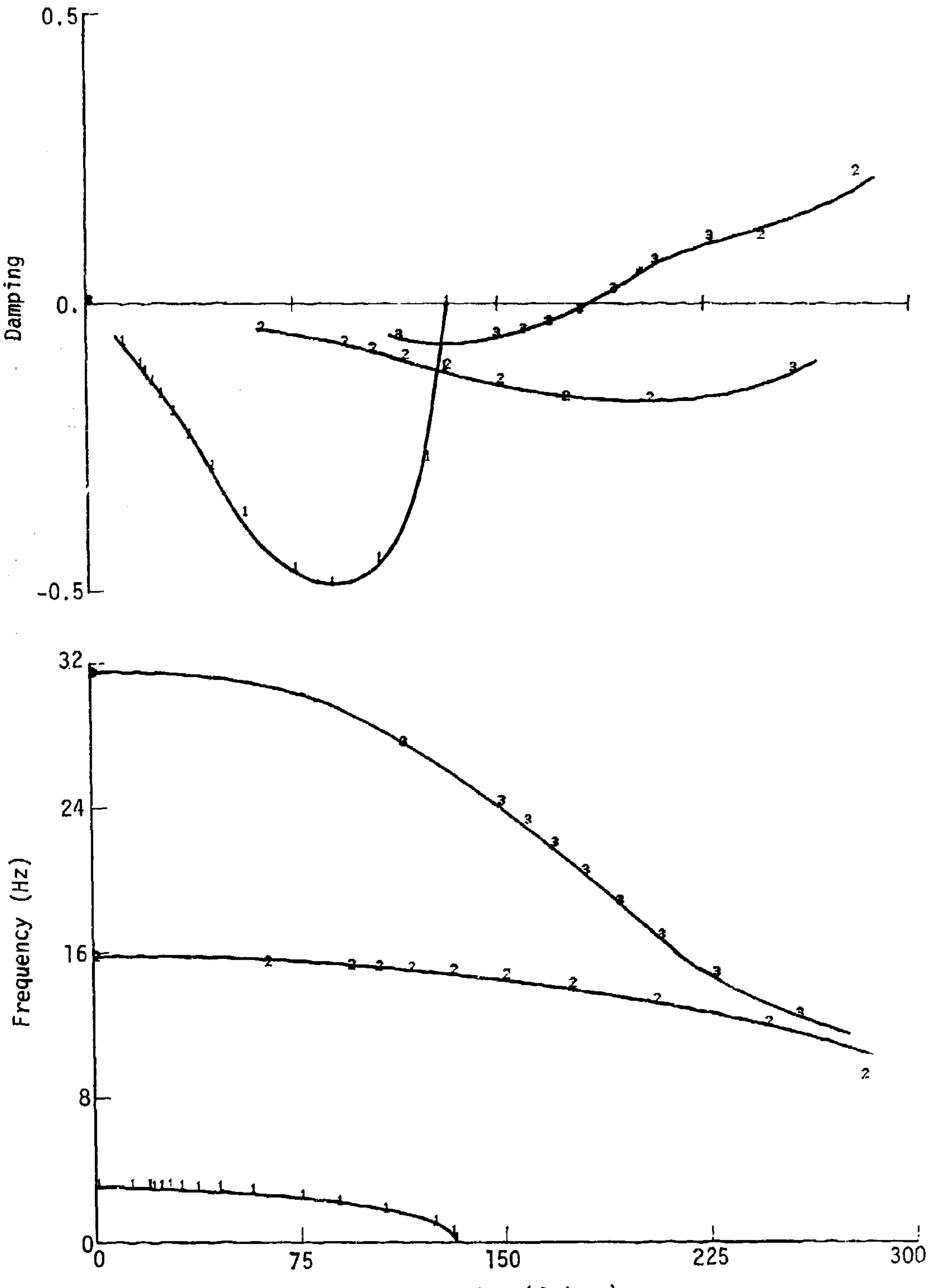

Figure C-37. NASTRAN analysis V-g and V-ω curves.
15° rotated model, Λ = -15°.

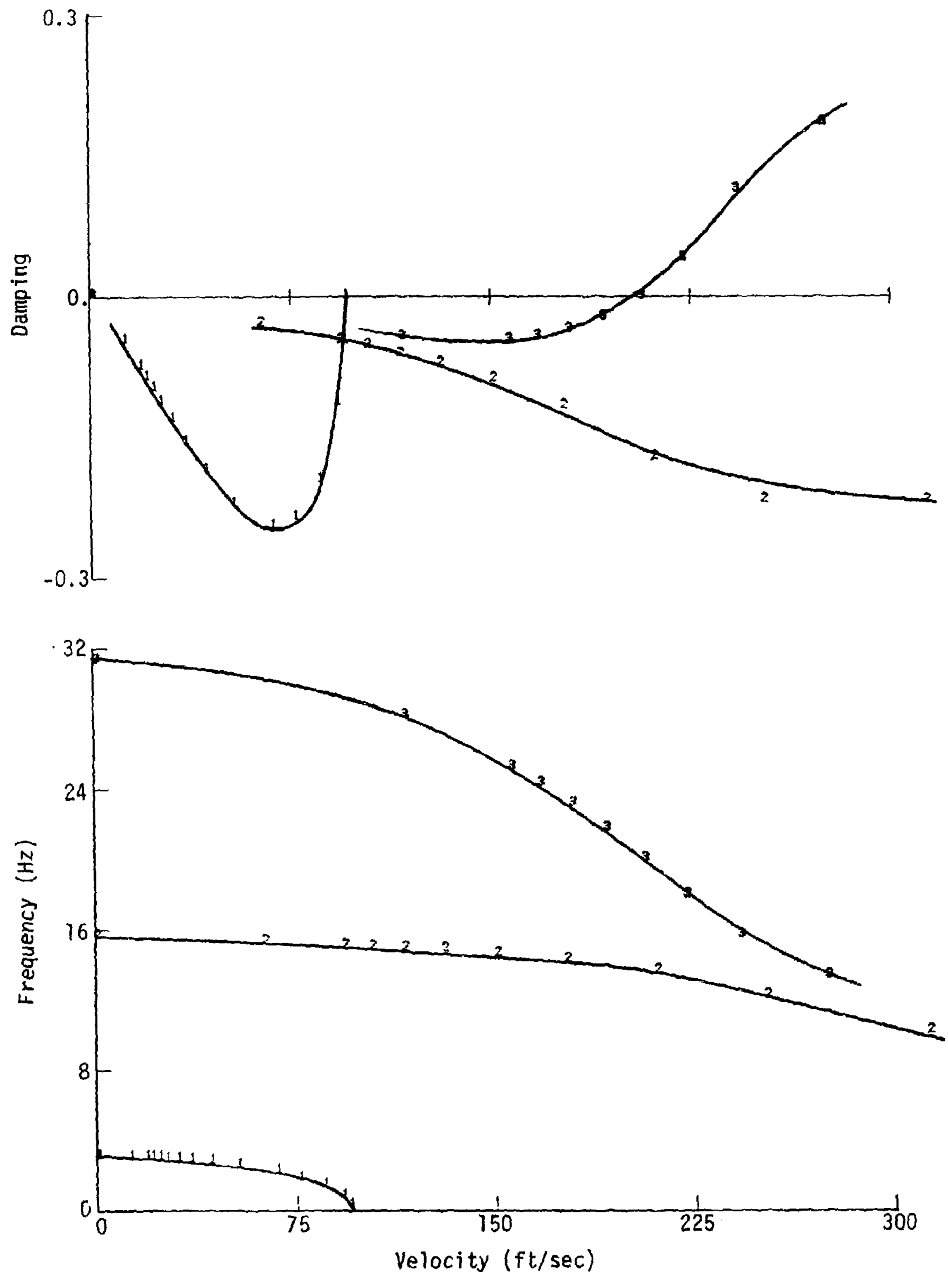

Figure C-38. NASTRAN analysis V-g and V-ω curves.
15° rotated model, Λ = -30°.

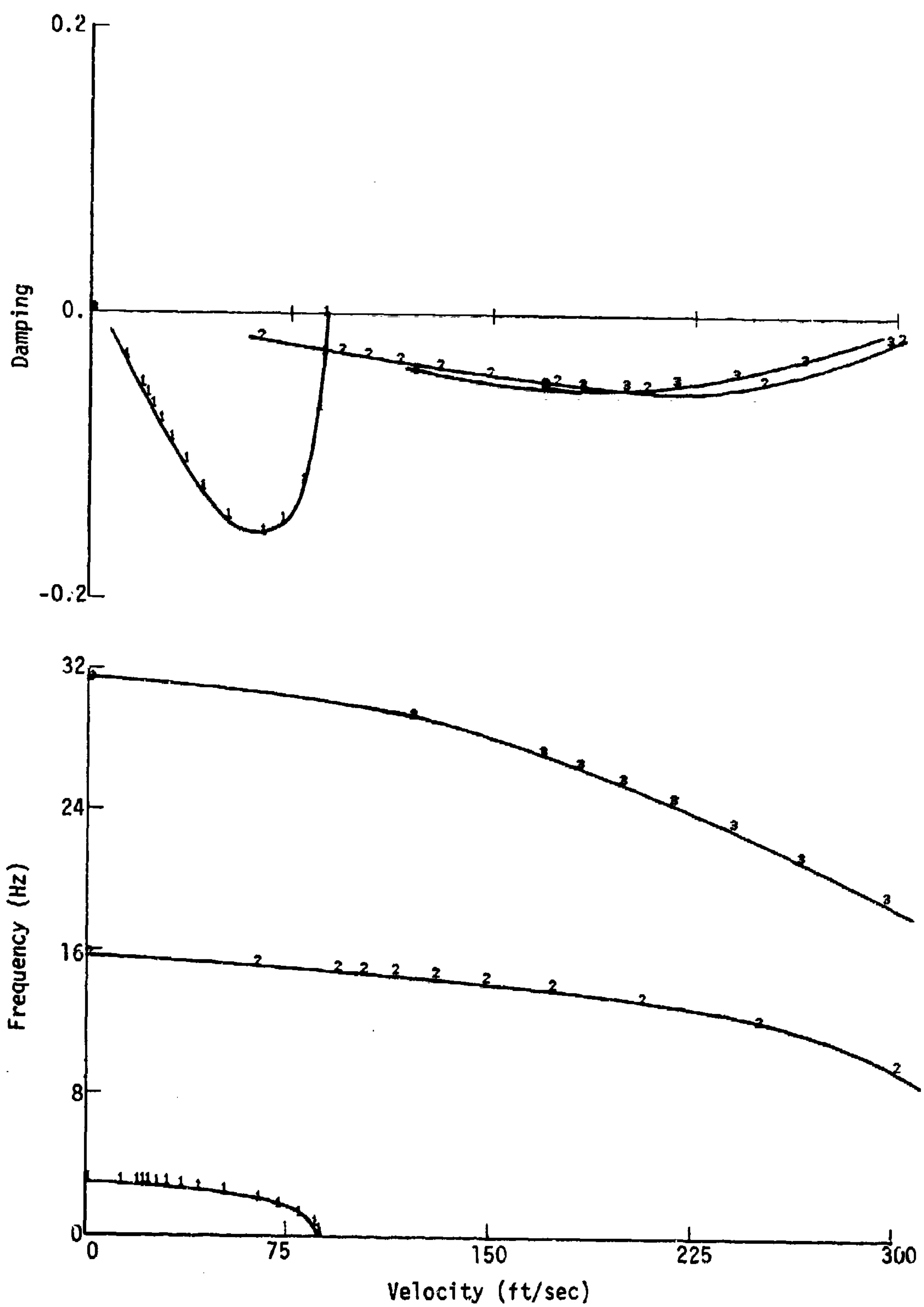

Figure C-39. NASTRAN analysis V-g and V-ω curves.
15° rotated model, Λ = -45°.

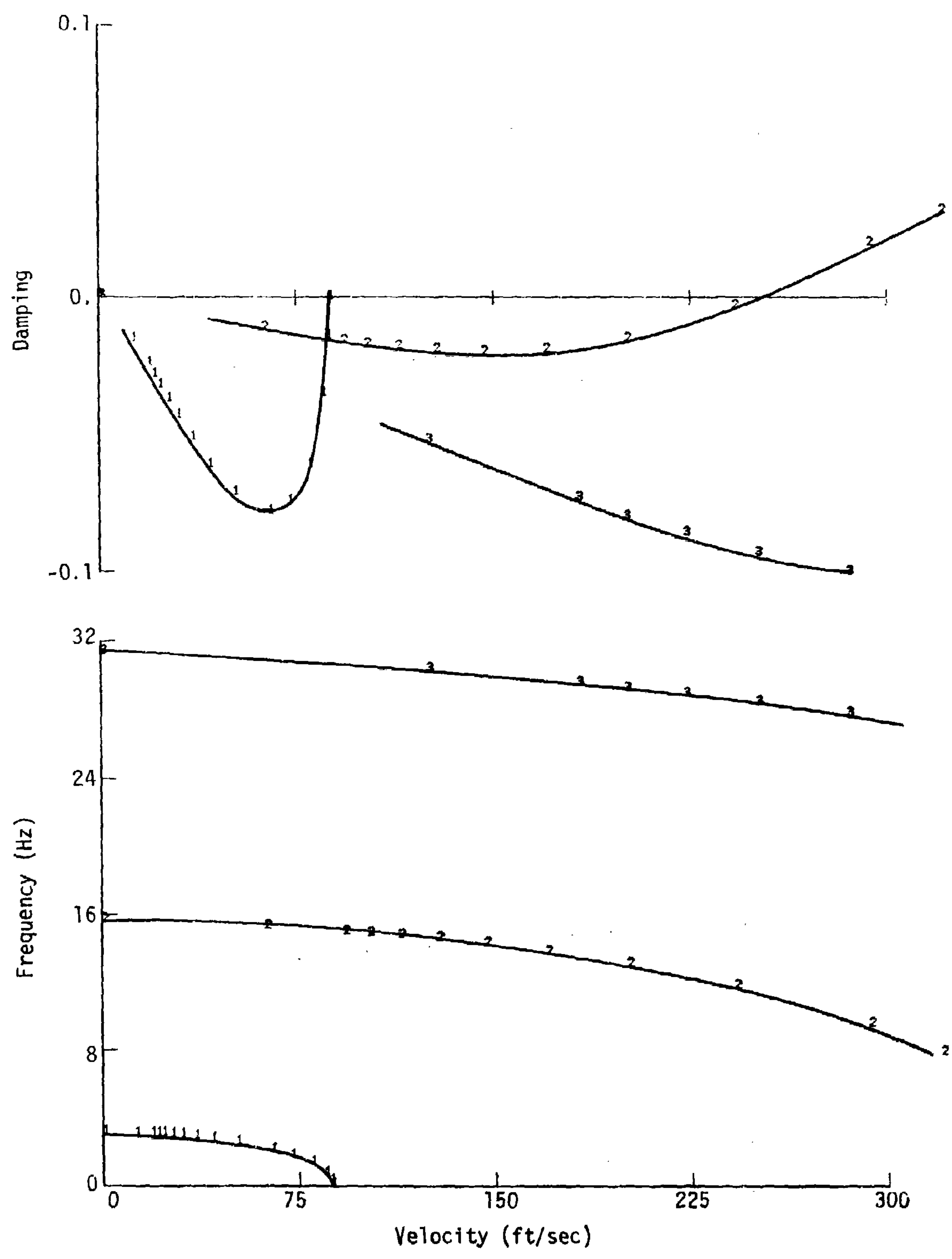

Figure C-40. NASTRAN analysis V-g and V-ω curves. 15° rotated model, Λ = -60°.

APPENDIX D

NASTRAN INPUT DATA

The data presented in this Appendix is the list of input required to perform a dynamic analysis using NASTRAN of the nonrotated model at -30° sweep.

```
                         S O R T E D   B U L K   D A T A   E C H O
CARD
COUNT      .   1  ..   2  ..   3  ..   4  ..   5  ..   6  ..   7  ..   8  ..   9  ..  1Ø  .
    1-     AERO    Ø          1.339+4 12.Ø     1.145-7 1
    2-     ASETI   3          1Ø      11       12      19      2Ø      21      28      +S1
    3-     +S1     29         3Ø      37       38      39      46      47      48      +S2
    4-     +S2     55         56      57       64      65      66      73      74      +S3
    5-     +S3     75
    6-     CAERO1  1Ø1        1       Ø        8       4                       1       +AERO1
    7-     +AERO1  -1.85      1.48    Ø.Ø      17.14   -15.75  25.48   Ø.Ø     6.86
    8-     CONM2   1          8       1        3.5Ø6-4 -3.131  .25     .Ø
    9-     CONM2   2          8       1        3.5Ø6-4 3.5Ø9   .25     .Ø
   1Ø-     CONM2   3          17      1        3.1Ø9-4 -2.9Ø   .25     .Ø
   11-     CONM2   4          17      1        3.1Ø9-4 3.34    .25     .Ø
   12-     CONM2   5          26      1        2.687-4 -2.67   .25     .Ø
   13-     CONM2   6          26      1        2.687-4 3.Ø7    .25     .Ø
   14-     CONM2   7          35      1        2.356-4 -2.4Ø   .25     .Ø
   15-     CONM2   8          35      1        2.356-4 2.86    .25     .Ø
   16-     CONM2   9          44      1        2.Ø14-4 -2.16   .25     .Ø
   17-     CONM2   1Ø         44      1        2.Ø14-4 2.61    .25     .Ø
   18-     CONM2   11         53      1        1.681-4 -1.92   .25     .Ø
   19-     CONM2   12         53      1        1.681-4 2.32    .25     .Ø
   2Ø-     CONM2   13         62      1        1.2Ø5-4 -1.72   .1Ø
   21-     CONM2   14         62      1        1.2Ø5-4 2.Ø7    .1Ø
   22-     CONM2   15         71      1        1.Ø2Ø-4 -1.74   .35
   23-     CONM2   16         71      1        1.Ø2Ø-4 1.39    .35
   24-     CORD2R  1          Ø       .82Ø     -3.Ø6   .Ø      .82Ø    -3.Ø6   1.Ø     +CORD2
   25-     +CORD2  6.15       .Ø      .Ø
   26-     CQUAD1  1          1       2        2       4       1       .Ø
   27-     CQUAD1  2          1       5        2       3       6       .Ø
   28-     CQUAD1  3          1       5        8       7       4       .Ø
   29-     CQUAD1  4          1       8        5       6       9       .Ø
   3Ø-     CQUAD1  5          1       8        11      1Ø      7       .Ø
   31-     CQUAD1  6          1       11       8       9       12      .Ø
   32-     CQUAD1  7          1       11       14      13      1Ø      .Ø
   33-     CQUAD1  8          1       14       11      12      15      .Ø
   34-     CQUAD1  9          1       14       17      16      13      .Ø
   35-     CQUAD1  1Ø         1       17       14      15      18      .Ø
   36-     CQUAD1  11         1       17       2Ø      19      16      .Ø
   37-     CQUAD1  12         1       2Ø       17      18      21      .Ø
   38-     CQUAD1  13         1       2Ø       23      22      19      .Ø
   39-     CQUAD1  14         1       23       2Ø      21      24      .Ø
   4Ø-     CQUAD1  15         1       23       26      25      22      .Ø
   41-     CQUAD1  16         1       26       23      24      27      .Ø
   42-     CQUAD1  17         1       26       29      28      25      .Ø
   43-     CQUAD1  18         1       29       26      27      3Ø      .Ø
   44-     CQUAD1  19         1       29       32      31      28      .Ø
   45-     CQUAD1  2Ø         1       32       29      3Ø      33      .Ø
   46-     CQUAD1  21         1       32       35      34      31      .Ø
   47-     CQUAD1  22         1       35       32      33      36      .Ø
```

```
CQUAD1  23    1     35    38    37    34    .0
CQUAD1  24    1     38    35    36    39    .0
CQUAD1  25    1     38    41    40    37    .0
CQUAD1  26    1     41    38    39    42    .0
CQUAD1  27    1     41    44    43    40    .0
CQUAD1  28    1     44    41    42    45    .0
CQUAD1  29    1     44    47    46    43    .0
CQUAD1  30    1     47    44    45    48    .0
CQUAD1  31    1     47    50    49    46    .0
CQUAD1  32    1     50    47    48    51    .0
CQUAD1  33    1     50    53    52    49    .0
CQUAD1  34    1     53    50    51    54    .0
CQUAD1  35    1     53    56    55    52    .0
CQUAD1  36    1     56    53    54    57    .0
CQUAD1  37    1     56    59    58    55    .0
CQUAD1  38    1     59    56    57    60    .0
CQUAD1  39    1     59    62    61    58    .0
CQUAD1  40    1     62    59    60    63    .0
CQUAD1  41    1     62    65    64    61    .0
CQUAD1  42    1     65    62    63    66    .0
CQUAD1  43    1     65    68    67    64    .0
CQUAD1  44    1     68    65    66    69    .0
CQUAD1  45    1     68    71    70    67    .0
CQUAD1  46    1     71    68    69    72    .0
CQUAD1  47    1     71    74    73    70    .0
CQUAD1  48    1     74    71    72    75    .0
CQUAD1  49    1     74    77    76    73    .0
CRIDG2  101   8     7     5     9     5     10    5     +B1
+B1     11    5     12    5
CRIDG2  103   17    16    5     18    5     19    5     +B2
+B2     20    5     21    5
CRIDG2  105   26    25    5     27    5     28    5     +B3
+B3     29    5     30    5
CRIDG2  107   35    34    5     36    5     37    5     +B4
+B4     38    5     39    5
CRIDG2  109   44    43    5     45    5     46    5     +B5
+B5     47    5     48    5
CRIDG2  111   53    52    5     54    5     55    5     +B6
+B6     56    5     57    5
CRIDG2  113   62    61    5     63    5     64    5     +B7
+B7     65    5     66    5
CRIDG2  115   71    70    5     72    5     73    5     +B8
+B8     74    5     75    5
CTRIA1  50    2     77    74    75    .0
EIGC    10    HESS  MAX                                 +EIGC
+EIGC
EIGR    20    INV   .0    40.0  6     3                 +EIGR
+EIGR   MAX
FLFACT  1     1.0
FLFACT  2     .13
```

```
 98-      FLFACT  3      .75    .5      .45     .4      .35     .3Ø     .25     +FL3
 99-      +FL3    Ø.2Ø   Ø.15   Ø.1Ø    Ø.Ø75   Ø.Ø5Ø   Ø.Ø25   Ø.Ø1    Ø.Ø
1ØØ-      FLUTTER 3Ø     K      1       2       3       S       3
1Ø1-      GRDSET                                        1       6
1Ø2-      GRID    1      1      2.45Ø   .Ø      .Ø
1Ø3-      GRID    2      1      6.15    .Ø      .Ø
1Ø4-      GRID    3      1      9.58    .Ø      .Ø
1Ø5-      GRID    4      1      2.378   1.5     .Ø
1Ø6-      GRID    5      1      5.972   1.5     .Ø
1Ø7-      GRID    6      1      9.3Ø2   1.5     .Ø
1Ø8-      GRID    7      1      2.295   3.25    .Ø
1Ø9-      GRID    8      1      5.764   3.25    .Ø
11Ø-      GRID    9      1      8.979   3.25    .Ø
111-      GRID    1Ø     1      2.271   3.75    .Ø
112-      GRID    11     1      5.7Ø5   3.75    .Ø
113-      GRID    12     1      8.886   3.75    .Ø
114-      GRID    13     1      2.187   5.5     .Ø
115-      GRID    14     1      5.497   5.5     .Ø
116-      GRID    15     1      8.562   5.5     .Ø
117-      GRID    16     1      2.1Ø4   7.25    .Ø
118-      GRID    17     1      5.29Ø   7.25    .Ø
119-      GRID    18     1      8.239   7.25    .Ø
12Ø-      GRID    19     1      2.Ø8Ø   7.75Ø   .Ø
121-      GRID    2Ø     1      5.23Ø   7.75Ø   .Ø
122-      GRID    21     1      8.145   7.75Ø   .Ø
123-      GRID    22     1      1.996   9.5     .Ø
124-      GRID    23     1      5.Ø23   9.5     .Ø
125-      GRID    24     1      7.822   9.5     .Ø
126-      GRID    25     1      1.913   11.25   .Ø
127-      GRID    26     1      4.815   11.25   .Ø
128-      GRID    27     1      7.498   11.25   .Ø
129-      GRID    28     1      1.889   11.75   .Ø
13Ø-      GRID    29     1      4.756   11.75   .Ø
131-      GRID    3Ø     1      7.4Ø6   11.75   .Ø
132-      GRID    31     1      1.8Ø6   13.5    .Ø
133-      GRID    32     1      4.548   13.5    .Ø
134-      GRID    33     1      7.Ø82   13.5    .Ø
135-      GRID    34     1      1.722   15.25   .Ø
136-      GRID    35     1      4.34Ø   15.25   .Ø
137-      GRID    36     1      6.758   15.25   .Ø
138-      GRID    37     1      1.693   15.75   .Ø
139-      GRID    38     1      4.281   15.75   .Ø
14Ø-      GRID    41     1      6.665   15.75   .Ø
141-      GRID    4Ø     1      1.615   17.5    .Ø
142-      GRID    41     1      4.Ø73   17.5    .Ø
143-      GRID    42     1      6.342   17.5    .Ø
144-      GRID    43     1      1.531   19.25   .Ø
145-      GRID    44     1      3.856   19.25   .Ø
146-      GRID    45     1      6.Ø13   19.25   .Ø
```

```
148-      GRID    47      1       3.8Ø6   19.75   .Ø
149-      GRID    48      1       5.926   19.75   .Ø
15Ø-      GRID    49      1       1.424   21.5    .Ø
151-      GRID    5Ø      1       3.598   21.5    .Ø
152-      GRID    51      1       5.6Ø2   21.5    .Ø
153-      GRID    52      1       1.34Ø   23.25   .Ø
154-      GRID    53      1       3.391   23.25   .Ø
155-      GRID    54      1       5.278   23.25   .Ø
156-      GRID    55      1       1.316   23.75   .Ø
157-      GRID    56      1       3.332   23.75   .Ø
158-      GRID    57      1       5.185   23.75   .Ø
159-      GRID    58      1       1.233   25.5    .Ø
16Ø-      GRID    59      1       3.124   25.5    .Ø
161-      GRID    6Ø      1       4.862   25.5    .Ø
162-      GRID    61      1       1.149   27.25   .Ø
163-      GRID    62      1       2.916   27.25   .Ø
164-      GRID    63      1       4.538   27.25   .Ø
165-      GRID    64      1       1.125   27.75   .Ø
166-      GRID    65      1       2.857   27.75   .Ø
167-      GRID    66      1       4.445   27.75   .Ø
168-      GRID    67      1       1.Ø61   29.1    .Ø
169-      GRID    68      1       2.697   29.1    .Ø
17Ø-      GRID    69      1       4.196   29.1    .Ø
171-      GRID    7Ø      1       .996    3Ø.45   .Ø
172-      GRID    71      1       2.536   3Ø.45   .Ø
173-      GRID    72      1       3.946   3Ø.45   .Ø
174-      GRID    73      1       .974    3Ø.917  .Ø
175-      GRID    74      1       2.481   3Ø.917  .Ø
176-      GRID    75      1       3.86Ø   3Ø.917  .Ø
177-      GRID    76      1       .89Ø    32.686  .Ø
178-      GRID    77      1       2.374   31.617  .Ø
179-      MAT1    3               .3Ø879+7
18Ø-      MAT2    1       .13825+6.27955+7-.131Ø-7.41178+7-.131Ø-7.3Ø879+7.14763-3
181-      MAT2    2       .81837+3.16Ø62+2-.97Ø7+1.93597+2-.97Ø7+1.58537+2
182-      MKAERO1 .1      .2                                                      +KAERO1
183-      +KAERO1 Ø.76    Ø.333   Ø.Ø12   Ø.Ø6Ø   Ø.ØØ1
184-      PAERO1  1
185-      PARAM   COUPMASS1
186-      PARAM   LMODES  3
187-      PARAM   VREF    12.
188-      PQUAD1  1       1       .ØØ5    2       1.Ø     3       .Ø
189-      PTRIA1  2       1       .ØØ8    2       1.Ø     3       .Ø
19Ø-      SET1    1       4       5       6       1Ø      11      12      19      +SE1
191-      +SE1    2Ø      21      28      29      3Ø      37      38      39      +SE2
192-      +SE2    46      47      48      55      56      57      64      65      +SE3
193-      +SE3    66      7Ø      71      72
194-      SPLINE1 1ØØØ    1Ø1     1Ø1     132     1
          ENDDATA
```

APPENDIX E

MEASURED INFLUENCE COEFFICIENT MATRICES

The tables presented in this Appendix are the measured influence coefficient matrices. The influence coefficient test, setup and data reduction are presented in detail in Reference 19.

MEASURED INFLUENCE COEFFICIENT MATRIX FOR ALUMINUM PLATE

.0021	.0004	.0043	.0021	.0063	.0044	.0086	.0068	.0107	.0092	.0128	.0112	.0149	.0140	.0165	.0157
	.0018	.0017	.0035	.0031	.0052	.0049	.0065	.0061	.0077	.0080	.0093	.0098	.0107	.0109	.0120
		.0182	.0110	.0319	.0252	.0463	.0394	.0590	.0534	.0755	.0660	.0887	.0803	.0969	.0940
			.0158	.0218	.0295	.0353	.0400	.0465	.0517	.0608	.0631	.0736	.0751	.0829	.0845
				.0642	.0539	.0989	.0868	.1381	.1227	.1728	.1610	.2127	.1952	.2342	.2274
					.0680	.0936	.1007	.1285	.1358	.1709	.1673	.2072	.2002	.2290	.2315
						.1812	.1615	.2485	.2306	.3399	.3028	.4172	.3867	.4682	.4483
							.1674	.2268	.2300	.3124	.2985	.3879	.3751	.4319	.4316
								.3565	.3201	.5067	.4531	.6328	.5765	.7199	.6857
									.3361	.4406	.4513	.5982	.6070	.6921	.7029
										.7403	.6883	.9555	.8895	1.1057	1.0285
											.6214	.8519	.8175	.9702	.9643
												1.2657	1.1800	1.4461	1.4116
													1.1099	1.3435	1.3375
														1.7417	1.7033
															1.6106

SYMMETRIC

MEASURED INFLUENCE COEFFICIENT MATRIX FOR NONROTATED PLATE

.0031	.0001	.0061	.0020	.0084	.0041	.0114	.0067	.0135	.0092	.0164	.0122	.0181	.0152	.0202	.0174
	.0047	.0019	.0079	.0050	.0102	.0092	.0128	.0127	.0154	.0161	.0175	.0203	.0199	.0231	.0218
		.0217	.0120	.0369	.0242	.0578	.0395	.0720	.0546	.0908	.0687	.1062	.0893	.1171	.1061
			.0296	.0304	.0477	.0489	.0637	.0655	.0786	.0876	.0986	.1062	.1147	.1197	.1309
				.0738	.0531	.1163	.0937	.1561	.1291	.2014	.1709	.2458	.2128	.2766	.2526
					.0918	.1060	.1369	.1423	.1714	.1924	.2129	.2343	.2483	.2648	.2873
						.2497	.1839	.3314	.2913	.4373	.3739	.5240	.4694	.5932	.5266
							.2299	.2705	.3028	.3685	.3873	.4563	.4761	.5221	.5474
								.4273	.4309	.5033	.5509	.7319	.6822	.8441	.8074
									.4251	.5367	.5649	.6753	.6927	.7795	.8145
										.8604	.7235	1.0899	1.0138	1.2436	1.1975
											.6957	.9375	.9529	1.1706	1.1349
												1.4125	1.3218	1.6341	1.6235
													1.3399	1.5436	1.5553
														1.9193	1.9056
															1.9917

SYMMETRIC

BEST AVAILABLE COPY

MEASURED INFLUENCE COEFFICIENT MATRIX FOR 7.5 ROTATED PLATE

.0045	.0001	.0066	.0015	.0038	.0032	.0109	.0058	.0128	.0083	.0150	.0108	.0170	.0125	.0187	.0145
	.0039	.0020	.0076	.0048	.0113	.0086	.0142	.0136	.0178	.0188	.0214	.0230	.0246	.0259	.0276
		.0251	.0119	.0417	.0251	.0534	.0408	.0707	.0584	.0872	.0716	.1004	.0867	.1092	.0988
			.0294	.0284	.0525	.0472	.0703	.0719	.0885	.0985	.1069	.1162	.1278	.1317	.1366
				.0903	.0651	.1282	.1072	.1769	.1569	.2214	.1941	.2645	.2443	.2319	.2728
					.1141	.1128	.1658	.1679	.2314	.2328	.2803	.2866	.3291	.3368	.3656
						.2069	.1908	.2942	.2871	.3892	.3734	.4654	.4393	.5272	.4990
							.2047	.3073	.3838	.4213	.4745	.5300	.5661	.6069	.6314
								.4708	.4772	.6288	.5958	.7897	.7456	.9490	.8063
									.5895	.6913	.7258	.8834	.8574	1.0035	.9860
										.9689	.8995	1.1563	1.1188	1.3242	1.2915
											.9326	1.1648	1.2474	1.3581	1.3781
												1.5092	1.5020	1.7766	1.7310
													1.5798	1.7705	1.7719
														2.0823	2.1063
															2.0537

SYMMETRIC

MEASURED INFLUENCE COEFFICIENT MATRIX FOR 15 ROTATED PLATE

.0035	.0002	.0050	.0012	.0063	.0022	.0078	.0034	.0092	.0047	.0107	.0056	.0119	.0065	.0135	.0073
	.0029	.0026	.0068	.0064	.0112	.0106	.0146	.0156	.0182	.0196	.0219	.0244	.0248	.0273	.0270
		.0305	.0146	.0474	.0321	.0637	.0482	.0806	.0694	.0965	.0824	.1149	.1026	.1243	.1182
			.0318	.0376	.0611	.0648	.0837	.0972	.1078	.1219	.1308	.1539	.1583	.1711	.1716
				.1013	.0844	.1532	.1333	.2057	.1699	.2538	.2381	.3068	.2829	.3365	.3230
					.1400	.1580	.2039	.2420	.2650	.3130	.3315	.3976	.4073	.4423	.4474
						.2704	.2568	.3918	.3646	.4951	.4776	.6160	.5917	.6804	.6729
							.3260	.3867	.4402	.5416	.5915	.6950	.7237	.7832	.8845
								.6087	.6274	.8133	.7952	1.0132	.9493	1.1692	1.0665
									.6678	.9093	.9458	1.1485	1.1344	1.2762	1.2739
										1.1222	1.1163	1.4715	1.4471	1.7172	1.6575
											1.2297	1.5216	1.5540	1.7924	1.8129
												2.0135	2.0069	2.3475	2.2783
													1.9710	2.3537	2.3117
														2.7030	2.8253
															2.6916

SYMMETRIC

BEST AVAILABLE COPY

BEST AVAILABLE COPY

MEASURED INFLUENCE COEFFICIENT MATRIX FOR ALUMINUM MODEL

.0017	.0004	.0041	.0023	.0067	.0046	.0083	.0071	.0110	.0097	.0125	.0115	.0143	.0134	.0157	.0152
	.0016	.0019	.0033	.0039	.0051	.0054	.0067	.0073	.0062	.0092	.0099	.0111	.0117	.0119	.0129
		.0184	.0115	.0354	.0265	.0463	.0419	.0633	.0563	.0765	.0744	.0900	.0861	.0975	.0964
			.0163	.0254	.0294	.0366	.0409	.0513	.0539	.0637	.0678	.0755	.0779	.0882	.0872
				.0796	.0624	.1145	.1028	.1598	.1488	.1981	.1912	.2344	.2264	.2594	.2589
					.0669	.0941	.1010	.1351	.1397	.1712	.1724	.2021	.2004	.2231	.2310
						.1834	.1639	.2638	.2439	.3350	.3281	.4039	.3926	.4483	.4477
							.1700	.2443	.2465	.3143	.3264	.3836	.3860	.4273	.4358
								.4057	.3885	.5313	.4875	.6496	.6360	.7291	.7301
									.3702	.4998	.4792	.8186	.6184	.6925	.7088
										.7249	.6654	.9148	.8934	1.0385	1.0381
											.6314	.8637	.8573	.9888	.9934
												1.1752	1.1543	1.3566	1.3578
													1.1490	1.3327	1.3482
														1.5739	1.5797
															1.5984

SYMMETRIC

MEASURED INFLUENCE COEFFICIENT MATRIX FOR NONROTATED MODEL

.0025	.0000	.0055	.0020	.0079	.0049	.0107	.0076	.0130	.0110	.0158	.0136	.0175	.0155	.0204	.0177
	.0029	.0019	.0055	.0046	.0088	.0073	.0117	.0107	.0142	.0135	.0165	.0156	.0187	.0190	.0204
		.0222	.0120	.0366	.0277	.0559	.0446	.0712	.0625	.0880	.0776	.1006	.0928	.1161	.1124
			.0235	.0259	.0428	.0427	.0587	.0605	.0734	.0768	.0873	.0904	.1006	.1048	.1142
				.0851	.0808	.1296	.1029	.1735	.1509	.2140	.1883	.2484	.2286	.2880	.2649
					.0934	.1050	.1386	.1557	.1861	.1983	.2200	.2381	.2591	.2868	.2930
						.2204	.1822	.3112	.2709	.3904	.3512	.4685	.4399	.5447	.5010
							.2293	.2762	.3191	.3607	.3932	.4447	.4769	.5303	.5346
								.4600	.4217	.6114	.5466	.7430	.6979	.8838	.8092
									.4832	.5659	.6059	.7109	.7510	.8474	.8489
										.8301	.7695	1.0465	.9987	1.2413	1.1549
											.8138	.9870	1.0361	1.1926	1.1808
												1.3617	1.3125	1.6367	1.5282
													1.3628	1.5903	1.5696
														2.0052	1.8751
															1.8339

SYMMETRIC

BEST AVAILABLE COPY

MEASURED INFLUENCE COEFFICIENT MATRIX FOR 7.5 ROTATED MODEL

.0023	.0000	.0042	.0018	.0060	.0038	.0083	.0062	.0103	.0079	.0120	.0104	.0136	.0126	.0150	.0138
	.0029	.0019	.0062	.0048	.0096	.0087	.0125	.0122	.0153	.0151	.0130	.0180	.0204	.0213	.0221
		.0224	.0118	.0372	.0255	.0549	.0411	.0692	.0577	.0817	.0735	.0939	.0889	.1062	.0973
			.0268	.0288	.0479	.0513	.0655	.0717	.0827	.0894	.1005	.1059	.1159	.1248	.1259
				.0787	.0627	.1281	.1043	.1670	.1505	.2033	.1900	.2381	.2300	.2783	.2548
					.1042	.1196	.1534	.1742	.2051	.2235	.2506	.2590	.2958	.3210	.3247
						.2333	.2034	.3228	.2953	.4029	.3837	.4792	.4728	.5631	.5231
							.2477	.3071	.3477	.3990	.4391	.4884	.5263	.5837	.5716
								.4807	.4633	.6254	.6105	.7608	.7714	.9159	.8584
									.5295	.6196	.6781	.7733	.8381	.9303	.9217
										.8467	.8427	1.0674	1.0771	1.2788	1.2075
											.9208	1.0803	1.1594	1.3150	1.2988
												1.3553	1.3966	1.6631	1.5896
													1.4982	1.7238	1.7003
														2.0688	1.9785
															1.9431

SYMMETRIC

MEASURED INFLUENCE COEFFICEINT MATRIX FOR 15 ROTATED MODEL

.0028	.0006	.0056	.0024	.0076	.0055	.0093	.0077	.0111	.0104	.0139	.0113	.0162	.0141	.0209	.0158
	.0040	.0037	.0082	.0086	.0137	.0138	.0166	.0190	.0228	.0241	.0264	.0299	.0328	.0381	.0370
		.0250	.0162	.0416	.0336	.0603	.0502	.0757	.0704	.0941	.0858	.1127	.1055	.1258	.1191
			.0327	.0413	.0573	.0702	.0824	.0950	.1096	.1253	.1304	.1521	.1561	.1744	.1774
				.0922	.0857	.1482	.1375	.1914	.1967	.2498	.2348	.3019	.2864	.3350	.3285
					.0911	.1555	.1679	.2118	.2352	.2881	.2878	.3570	.3444	.3933	.3965
						.2666	.2594	.3638	.3788	.4859	.4690	.5982	.5766	.6634	.6567
							.3055	.3762	.3940	.5191	.5394	.6501	.6573	.7291	.7519
								.5235	.5693	.7353	.7158	.9233	.8884	1.0268	1.0316
									.6768	.8110	.8478	1.0477	1.0562	1.1763	1.2168
										1.0605	1.0551	1.3696	1.3361	1.5451	1.5577
											1.1086	1.3959	1.4050	1.5920	1.6403
												1.8465	1.8097	2.0972	2.1410
													1.8330	2.0662	2.1433
														2.4197	2.4721
															2.5737

SYMMETRIC

REFERENCES

1. Bisplinghoff, R. L., Ashley, H., and Halfman, R. L., Aeroelasticity, Addison-Wesleublishing Company, Inc., Reading, Massachusetts, 1955, pp. 421-526.

2. Krone, N. J., Jr., "Divergence Elimination With Advanced Composites", AIAA Paper No. 75-1009, presented at AIAA 1975 Aircraft Systems and Technology Meeting, Los Angeles, August 1976.

3. McCullers, L. A., and Lynch, R. W., "Dynamic Characteristics of Advanced Filamentary Composite Structures", Volumes I through III AFFDL-TR-73-111, Air Force Flight Dynamics Laboratory, Wright-Patterson AFB, Ohio, September 1974.

4. Lynch, R. W., Rogers, W. A., and Braymen, W. W., "Aeroelastic Tailoring of Advanced Composite Structures for Military Aircraft", Volumes I through III, AFFDL-TR-76-100, Air Force Flight Dynamics Laboratory, Wright-Patterson AFB, Ohio, February 1978.

5. Weisshaar, T. A., "Aeroelastic Stability and Performance Characteristics of Aircraft with Advanced Composite Swept Forward Wing Structure", AFFDL-TR-78-116, Air Force Flight Dynamics Laboratory, Wright-Patterson AFB, Ohio, September 1978.

6. Weisshaar, T. A., "Forward Swept Wing Static Aeroelasticity", AFFDL-TR-79-3087, Air Force Flight Dynamics Laboratory, Wright-Patterson AFB, Ohio, June 1979.

7. Shirk, M. H., and Griffin, K. E., "The Role of Aeroelasticity in Aircraft Design with Advanced Composite Filamentary Composite Materials", presented at the Second Conference on Fibrous Composites in Flight Vehicles, Williamsburg, Virginia, November 1975.

8. Austin, E., Hadcock, R., Hutchings, D., Sharp, D., Tang, S., and Waters, D., "Aeroelastic Tailoring of Advanced Composite Lifting Surfaces in Preliminary Design", Presented at the AIAA/ASME/SAE 17th Structures, Structural Dynamics, and Materials Conference, Valley Forge, Pennsylvania, May 1976.

9. Lerner, E., and Markowitz, J., "An Efficient Structural Resizing Procedure for Meeting Static Aeroelastic Design Objectives", AIAA/ASME 19th Structures, Structural Dynamics, and Materials Conference, Bethesda, Maryland, April 1978.

10. Triplett, W. E., "Aeroelastic Tailoring Studies in Fighter Aircraft Design", presented at AIAA/ASME/ASCE/AHS 20th Structures, Structural Dynamics, and Materials Conference, St. Louis, Missouri, April 1979.

11. Gimmestad, D., "An Aeroelastic Optimization Procedure for Composite High Aspect Ratio Wings", presented at AIAA/ASME/ASCE/AHS 20th Structures, Structural Dynamics, and Materials Conference, St. Louis, Missouri, April 1979.

12. Gustavsson, S. A. L., A Computer Program for the Prediction of Aerodynamic Characteristics of Wing-Body-Tail Combination at Subsonic and Supersonic Speeds, The Aeronautical Research Institute Institute of Sweden, Report FFA AU-635, Part 2, Stockholm, Sweden, November 1972.

13. Giesing, J. P., Kalman, T. P. and Rodden, W. P., "Subsonic Unsteady Aerodynamics for General Applications", AFFDL-TR-71-5, Air Force Flight Dynamic Laboratory, Wright-Patterson AFB, Ohio, November 1971.

14. The NASTRAN User's Manual, (Level 17.0), NASA SP-222(04), National Aeronautics and Space Administration, Washington D.C., December 1979.

15. Reed, D. L., "Point Stress Laminate Analysis", FZM-5494, General Dynamics, Fort Worth Division, Fort Worth, Texas, April 1970.

16. Venkayya, V. B., "Beaming - A Program for Beaming Airloads to Structural Grid", AFWAL-TM-81-92-FIBR, Air Force Wright Aeronautical Laboratories, Wright-Patterson AFB, Ohio, August 1981.

17. Simites, G. J., Introduction to the Elastic Stability of Structures, Englewood Cliffs, New Jersey, Prentice Hall, 1976, pp. 66-68.

18. Dowell, E. H., et al, A Modern Course in Aeroelasticity, Sijthoff and Noordhoff, The Netherlands, 1978, pp. 3-8.

19. Pendleton, E. W., "Static Load Deflection Testing of a Forward Swept Wing Model", AFWAL-TM-81-93-FIBRC, Air Force Wright Aeronautical Laboratories, Wright-Patterson AFB, Ohio, July 1981.

☆U.S.Government Printing Office: 1982 — 559-005/4042